TRIUMF

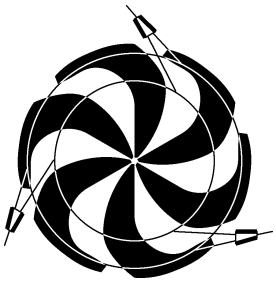

ANNUAL REPORT
SCIENTIFIC ACTIVITIES
2005

ISSN 1492-417X

CANADA'S NATIONAL LABORATORY FOR PARTICLE AND NUCLEAR PHYSICS

OPERATED AS A JOINT VENTURE

MEMBERS:

THE UNIVERSITY OF ALBERTA
THE UNIVERSITY OF BRITISH COLUMBIA
CARLETON UNIVERSITY
SIMON FRASER UNIVERSITY
THE UNIVERSITY OF TORONTO
THE UNIVERSITY OF VICTORIA

ASSOCIATE MEMBERS:

THE UNIVERSITY OF GUELPH
THE UNIVERSITY OF MANITOBA
McMASTER UNIVERSITY
L'UNIVERSITÉ DE MONTRÉAL
QUEEN'S UNIVERSITY
THE UNIVERSITY OF REGINA
SAINT MARY'S UNIVERSITY

UNDER A CONTRIBUTION FROM THE
NATIONAL RESEARCH COUNCIL OF CANADA

DECEMBER 2006

The contributions on individual experiments in this report are outlines intended to demonstrate the extent of scientific activity at TRIUMF during the past year. The outlines are not publications and often contain preliminary results not intended, or not yet ready, for publication. Material from these reports should not be reproduced or quoted without permission from the authors.

Experiment 715
Weak interaction symmetries in β^+ decay of optically trapped ^{37,38m}K
(J.A. Behr, M.R. Pearson, TRIUMF; K.P. Jackson, TRIUMF/SFU)

Reports on β-decay experiments with the TRIUMF neutral atom trap can be found here, and in reports on Expts. 956 and 1070.

Scalar search status

Our result for the β-ν correlation parameter $\tilde{a} = 0.9981 \pm 0.0030^{+0.0032}_{-0.0037}$ is an improvement over previous results in the literature. It is therefore the best limit on general scalar interactions coupling to the first generation. It is now published [Gorelov, Phys. Rev. Lett. **94**, 142501 (2005)].

At the December EEC, we received permission to upgrade this experiment. Details can be found in the report for Expt. 1070.

Polarized measurements

Our result for the neutrino asymmetry in the decay of polarized ^{37}K is $B_\nu = -0.755 \pm 0.020 \pm 0.013$, consistent with the standard model prediction $B_\nu = -0.7692(15)$. The largest errors are from the polarization, and from knowledge of the displacement of the trap position for the two different polarizations. We could measure the latter better in the future by taking more snapshots of the cloud expansion with the MOT light. We will minimize the displacement by shifting the optical pumping diode laser frequency between polarization states, and by using a high-power laser for the optical pumping beam and expanding it to larger diameter to ensure overlap with the cloud.

This is the only measurement of a ν asymmetry other than in neutron decay, and has achieved similar accuracy. This constrains a W_R boson coupling to right-handed ν's to have mass >170 GeV/c^2 (90% confidence), a result which is not yet competitive with the world average of other β-decay experiments. D. Melconian successfully defended his SFU Ph.D. thesis in November.

Our first steps toward loading a circularly polarized far off-resonance dipole force trap (FORT) to only trap fully polarized atoms were described in last year's Annual Report. E. Prime has completed her M.Sc. thesis on this topic.

Atomic electron detector upgrade

We have installed a detector for atomic shakeoff electrons. We have demonstrated an efficiency of ≈47% for low-energy electrons from photoionization, and similar tens of per cent efficiency for the atomic electrons from β decay of ^{80}Rb. See the report on Expt. 956 for experimental details.

Here we comment on possible improvements to ^{37}K utilizing this high-statistics technique. For β^+ decay, ≈15% of the daughter nuclei are produced as charged ions which can be detected and collected. We normally detect coincidences between these and a 1% solid angle β^+ detector. The atomic electron detector will therefore increase the efficiency of coincidences by ≈30 times. For asymmetry experiments, there is very little loss in sensitivity. We also expect the β^+ asymmetry in singles to have much less background when an atomic electron coincidence is required, as that will mostly select events decaying in the trap region.

In Fig. 56 we show an exclusion plot for manifest left-right models, showing our present B_ν result. We also show the exclusions that would occur for 0.001 accuracy results for the recoil singles asymmetry $A_{\rm recoil}$, assuming agreement with the standard model. This observable is sensitive to the Fermi/Gamow-Teller interference term, and its constraint is mainly on the left-right mixing angle ζ. We also show the β asymmetry constraint at the same accuracy. With the high-statistics electron coincidence, these observables can be measured to 0.001 statistical error in about 10 shifts, attaining statistical power similar to that of TWIST. The idea, of course, would be to use this statistical power to explore systematic errors in detail.

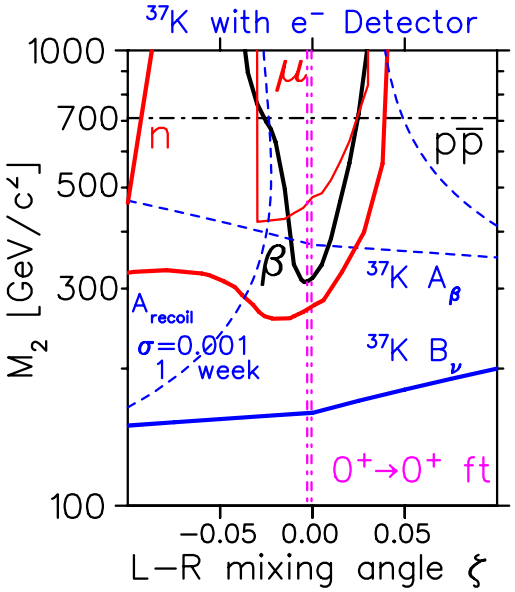

Fig. 56. Manifest left-right model exclusion plot. Present work excludes below solid blue line. Dashed blue lines are goals of 0.001 accuracy recoil asymmetry and β asymmetry, both using coincidences with atomic shakeoff electron detector.

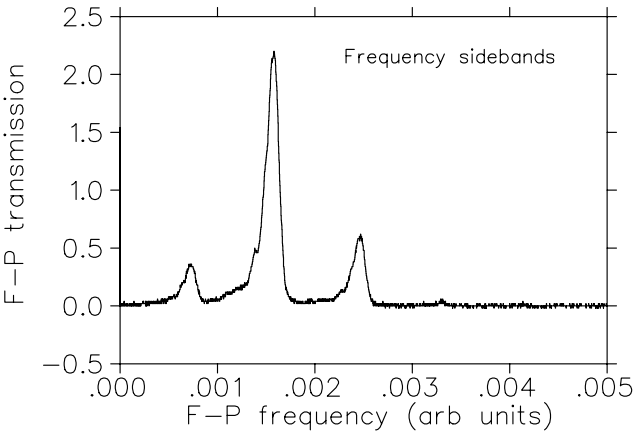

Fig. 57. Transmission of optical pumping diode laser light through Fabry-Perot interferometer, showing carrier frequency and sidebands to optically pump the hyperfine-split ground state.

Optical pumping improvements

A systematic error in ^{37}K experiments in D. Melconian's thesis was the inability to uniformly optically pump the entire cloud of atoms. A higher-power diode laser has been installed as one step toward overcoming this systematic error.

To optically pump both ground states, we inject rf at close to the hyperfine ground state splitting into the diode laser. We have now better characterized the resulting frequency content of the diode laser by measuring its transmission through a Fabry-Perot interferometer. In Fig. 57 we show the typical sidebands. The ratio between power in the carrier frequency and power in the sideband is important to model the optical pumping process and extract the polarization. In addition to FM modulation this technique incidentally applies an AM modulation, with the happy result that the unused lower-frequency sideband is suppressed.

Experiment 715 has approved shifts to test the next version of the ^{37}K experiment, though we expect to defend these at the summer 2006 EEC.

Experiment 823
Pure Fermi decay in medium mass nuclei
(G.C. Ball, TRIUMF)

Precise measurements of the intensities for superallowed Fermi $0^+ \rightarrow 0^+$ β-decays have provided a demanding test of the CVC hypothesis at the level of 3×10^{-4} and also led to a result in disagreement with unitarity (at the 98% confidence level) for the CKM matrix. Since this would have profound implications for the minimal standard model it is essential to address possible "trivial" explanations for this apparent non-unitarity, such as uncertainties in the theoretical isospin symmetry-breaking correction. Uncertainties in the calculated Coulomb corrections can be studied by extending the precision β-decay measurements to heavier ($A \geq 62,\ T_z = 0$) odd-odd nuclei where these corrections are predicted to be much larger [Towner and Hardy, Phys. Rev. **C66**, 035501 (2002)]. The primary goal of the Expt. 823 experimental program is to measure the half-lives and branching ratios for the superallowed β-decay of these radioactive nuclei produced at ISAC. The early measurements focused on ^{74}Rb (see TRIUMF 1999–2002 Annual Reports).

High precision measurement of the half-life of the superallowed β-emitter ^{62}Ga

A preliminary measurement of the half-life of ^{62}Ga, the first in the series of ($A \geq 62,\ T_z = 0$) odd-odd superallowed β-emitters, was carried out in the spring of 2003. The long-lived (9.74 m) isobar ^{62}Cu was a significant contaminant that limited the precision of this measurement. The results of this measurement were reported previously [TRIUMF 2003 and 2004 Annual Reports; Hyland *et al.*, J. Phys. G. Nucl. Part. Phys. **31**, S1885 (2005)]. The final result, 116.01 ± 0.19 ms, is statistically consistent with all previous measurements. However, the uncertainty in the world average half-life of ^{62}Ga, 116.17 ± 0.04 ms is dominated by a single high-precision measurement [Blank *et al.*, Phys. Rev. **C69**, 015502 (2004)]. Approval was obtained to substantially improve the precision of the present measurement to the required precision of $\sim$0.05% once the TRIUMF resonant ionization laser ion source (TRILIS) was operational.

Following the success of the first ^{62}Ga TRILIS development run in December, 2004 (see last year's Annual Report for details) beam time was allocated in December, 2005 to carry out a high-precision lifetime measurement. The experiment was carried out at GPS1 using the fast tape transport system. Details of this method have been described previously (see 1999 Annual Report). A beam of $\sim$5000 ^{62}Ga ions/s was delivered with about a factor of 100 reduction in the relative intensity of the long-lived isobaric contaminant ^{62}Cu. A representative decay spectrum observed for one run is shown in Fig. 58. A total of 55 runs, each with a statistical uncertainty of $\sim$0.15 ms, were obtained under various experimental conditions to test for systematic errors. A preliminary analysis has shown that these data are consistent with a statistical uncertainty in the ^{62}Ga half-life of $\sim$0.02 ms.

High precision branching-ratio measurement of the superallowed β-emitter ^{62}Ga

Non-analogue Fermi and Gamow-Teller branches in the superallowed β-decay of ^{62}Ga have been investigated recently at ISAC using the 8π spectrometer. The experiment was carried out in December, 2004 using a beam of $\sim$1600 ^{62}Ga ions/s produced during the first

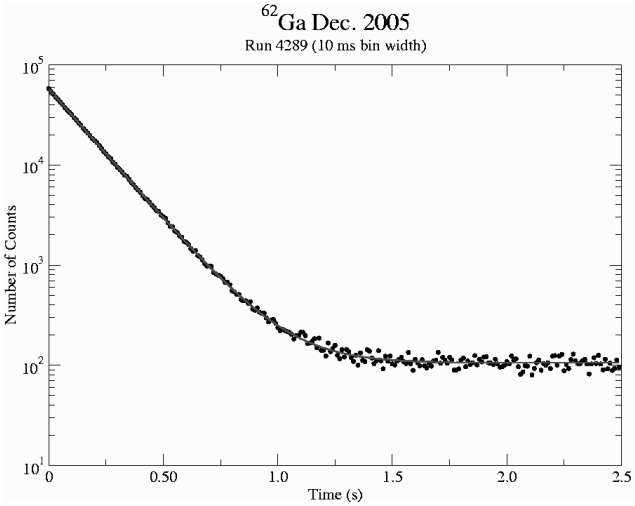

Fig. 58. ^{62}Ga decay curve obtained for run 4289. The fitted half-life (solid line) is 116.85 ± 0.13 ms.

beam development run with TRILIS. Details of this experiment were reported in last year's Annual Report. The analysis of these data has confirmed the observation of five excited 1^+ levels and the first excited 0^+ level in ^{62}Zn populated in the β-decay of ^{62}Ga. These states were found to decay directly to the ground state of ^{62}Zn and/or to the lowest three excited 2^+ levels in ^{62}Zn. The decay scheme is shown in Fig. 59. Nearly 90% of the observed intensity of the first excited 2^+ level at 954 keV could be attributed to the decay of the observed 0^+ and 1^+ levels. If we assume that the unobserved ground-state decay of weakly populated 1^+ levels in ^{62}Zn is comparable to the sum of all the observed intensity feeding the lowest three excited 2^+ levels in ^{62}Zn that couldn't be identified, then from these data it should be possible to determine the superallowed branching ratio of ^{62}Ga with an uncertainty of 0.02%.

This experiment was repeated in December, 2005 using a beam of ∼5000 ^{62}Ga ions/s which was more than 95% laser ionized. Approximately three times as much data were obtained. Preliminary analysis of these data has confirmed the earlier results. This improved data set will allow us to search for weaker transitions and improve the limits on the non-analogue Fermi and Gamow Teller decays of ^{62}Ga.

Experiment 870
Extracting (p, α) events using ^{10}B$(\alpha, p)^{13}$C

(B.R. Fulton, York; L. Buchmann, TRIUMF; T. Davinson, Edinburgh)

Experiment 870 is a proposal to measure the cross section for the reaction ^{18}Ne$(\alpha, p)^{21}$Na which now appears to be the most likely route for the breakout from the hot CNO cycle into the rp-process. This catastrophic thermonuclear runaway process is believed to

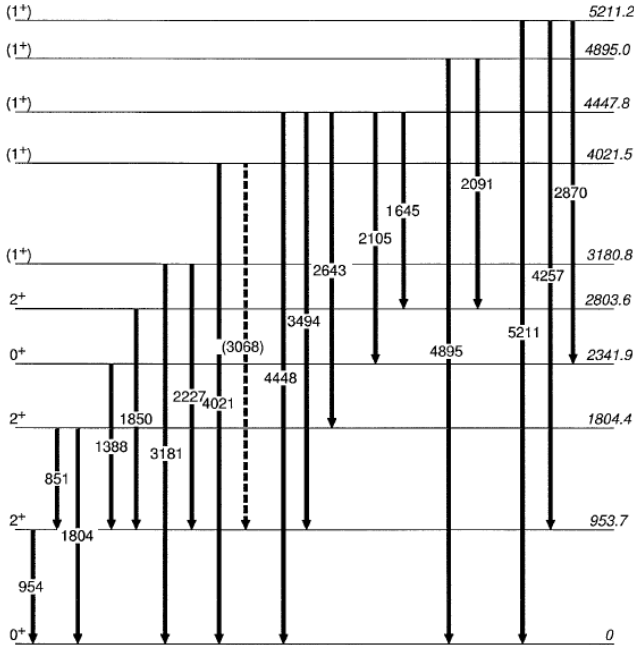

Fig. 59. Levels in ^{62}Zn populated in the β-decay of ^{62}Ga.

be the driving mechanism of astrophysical objects known as X-ray bursters. The experiment will use a radioactive ^{18}Ne beam from ISAC, the TUDA chamber, the York ^{4}He gas cell, and LEDA type silicon strip detectors.

ISAC has still not produced a ^{18}Ne beam, however, it is expected that the FEBIAD source, which will supply the beam, will come on-line in 2006. In order to make efficient use of the ^{18}Ne beam when it becomes available, a decision was made to test the experimental technique and the performance of the gas-target cell with the stable beam reaction, ^{10}B$(\alpha, p)^{13}$C. The experiment was carried out at the ISAC-I facility during August.

The ^{10}B$(\alpha, p)^{13}$C reaction was chosen as the test reaction because it is a direct (α, p) reaction with a positive Q value similar to that of the ^{18}Ne$(\alpha, p)^{21}$Na reaction of interest. The OLIS group was interested in developing a ^{10}B beam using a BF_3 gas and was sucessful in doing so just prior to the run. The ^{10}B$(\alpha, p)^{13}$C reaction has similar kinematics to ^{18}Ne$(\alpha, p)^{21}$Na when populating the range of energies, 12.29 → 13.74 MeV, in the compound nucleus ^{14}N. Populating these excited states creates ejectile protons with energies the same as those expected in the ^{18}Ne$(\alpha, p)^{21}$Na reaction. Studying the energy losses and straggling effects of the protons and duplicating the observations with simulations will be used to prepare on-line data reconstruction packages for Expt. 870.

Experimental set-up

The test experiment was undertaken using a ^{10}B beam in the 3^+ charge state at energies of 12.3 MeV

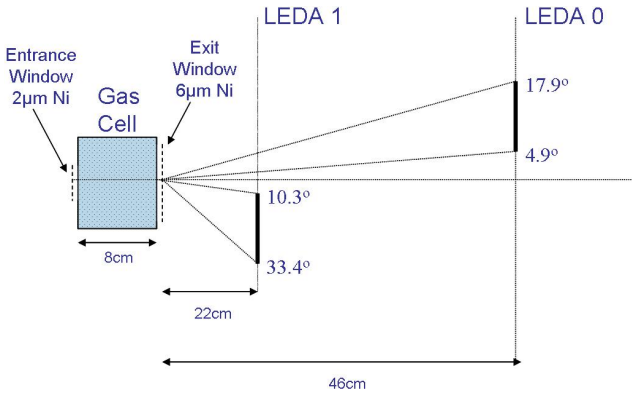

Fig. 60. Schematic of the detector set-up.

and 9.5 MeV. The gas cell was mounted inside the TUDA chamber on a newly adapted linear drive. This method allowed some adjustment of the gas cell alignment relative to the beam line. The alignment was confirmed by telescope to be within 1 mm in both x and y directions.

The detector configuration used for collection of the data is shown in Fig. 60. Two 1 mm LEDA sectors were positioned 22 cm and 46 cm from the back of the exit window of the gas target cell. The full LEDA arrays were not used, to simplify the electronics and minimize potential problems. The distances of the LEDA sectors from the back of the gas target were arranged to minimize the shadowing caused by the 22 cm LEDA sector (LEDA 1) preventing events from reaching the 46 cm LEDA sector (LEDA 0). By using two detector distances, the effect of the finite LEDA strip size can be assessed and an optimum detector distance decided upon for the Expt. 870 run. LEDA 1 provided angular coverage from 10.3° to 33.4°, LEDA 0 provided angular coverage from 4.9° to 17.9°. Particle identification was established using the time-of-flight method.

On-line analysis

Background data The presence of water vapour within the TUDA chamber caused a proton-rich layer to collect on the inner and outer surfaces of the entrance window. During the experiment, these protons can be elastically scattered from the window into the detector telescopes, forming a proton background against which the reaction protons from the ^{10}B$(\alpha, p)^{13}$C reaction are measured.

Several data runs were performed with no helium gas in the gas cell, the purpose of which was to detect and quantify this proton background from the entrance window and any other background that may arise. This was completed for the 12.3 MeV and the 9.5 MeV beam energies. An example spectrum is shown in Fig. 61. The two clear low energy data peaks correspond to protons scattered from the entrance window: the lower energy peak corresponding to protons scattered from the back

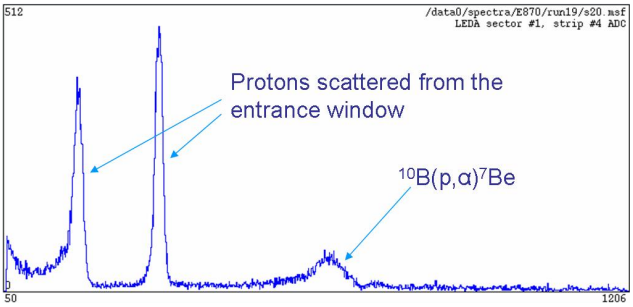

Fig. 61. Background data collected at ^{10}B 12.3 MeV.

of the entrance window and the slightly higher energy peak corresponding to protons scattered from the front of the entrance window. The third highest energy peak is thought to correspond to^{10}B$(p, \alpha)^{7}$Be events.

Reaction data For the (α, p) reaction experimental runs, helium gas was pumped into the gas cell at a pressure of 300 mbar for the 12.3 MeV ^{10}B beam energy and 200 mbar for the 9.5 MeV ^{10}B beam energy. The controlled pressure of the ^{4}He allowed the beam energy to degrade by a fixed amount enabling access to the relevant states in ^{14}N.

Figure 62 shows an example spectrum from a reaction run at 12.3 MeV. Some of the peaks have been tentatively identified as ^{10}B$(\alpha, p)^{13}$C reactions populating the ground state, first and second excited states in ^{13}C.

Following the collection of these data, the gas cell pressure was halved. The lower energy ^{14}N states observed in the high pressure run were expected to be absent for the low pressure run. This was confirmed.

Background reduction

Towards the latter stages of the experiment efforts were made to reduce the background contamination evident in the on-line spectra. One possible solution to the background arising from the entrance window is a piece of hardware, BaRT (background reduction tool). BaRT is a rubber-sealed 1 mm thick disk of tantalum with an 8 mm hole in the centre designed to slide inside the gas cell. When positioned ∼2 cm from the entrance

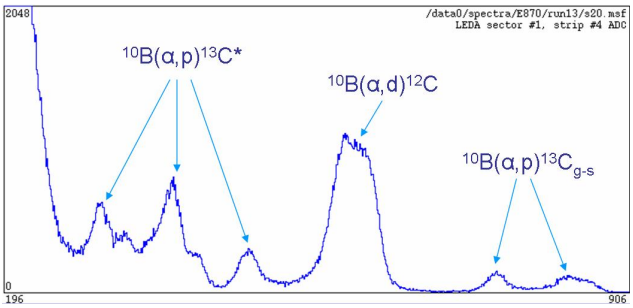

Fig. 62. Spectrum showing reaction data using 12.3 MeV beam with the gas target cell at 300 mbar pressure.

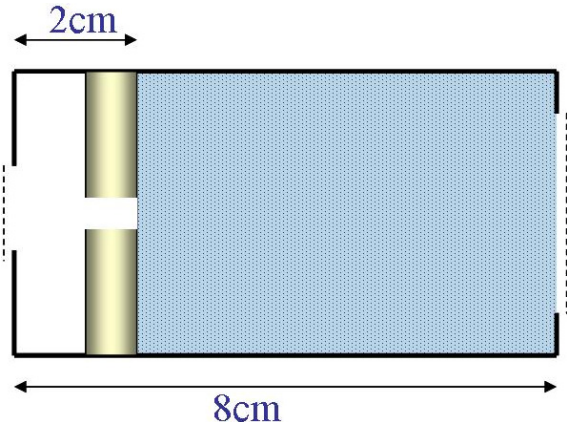

Fig. 63. A picture of the gas cell showing the position of BaRT inside.

window and held in place by grub screws against the inner walls of the gas cell, this restricts the angle at which ions can pass through the centre (see Fig. 63). All events occurring in the first 2 cm of the gas cell subtending an angle allowing them to pass through, subsequently fail to hit the LEDA detectors as the angle is smaller than the minimum angle covered by the detectors. This therefore reduces all background seen by the LEDA detectors originating before BaRT and cleans the spectrum notably.

The on-line spectra demonstrated the removal of prominent contaminant peaks for the runs using BaRT. In addition to the protons scattered from the entrance window, the (p, α) reactions appearing at higher energy were also removed from the spectra. However, some of the higher energy ^{14}N peaks from ^{10}B$(\alpha, p)^{13}$C were removed from the spectrum, due to the fact that they are produced in the region of the gas cell adjacent to the entrance window and prior to BaRT.

Background caused by fusion reactions of ^{10}B on carbon and oxygen deposits on the entrance window was also removed from the data.

Conclusions

The experimental set-up was sufficient to identify particles using the time-of-flight technique. Reaction data were collected for two beam energies, 12.3 MeV and 9.5 MeV, allowing a range of resonant states in the compound nucleus ^{14}N to be identified. Identification was confirmed by the expected disappearance of the lower energy states upon reduction of the gas cell pressure. The source of background contamination was identified, and a technique to remove it successfully tested.

Further analysis will extract the observed resolution and compare it to Monte Carlo simulations. The results will be used to prepare for Expt. 870. The ^{10}B$(\alpha, p)^{13}$C run, however, has confirmed the feasibility of the proposed experiment.

Experiment 875
MuScat - the measurement of muon scattering in low Z materials
(R. Edgecock, RAL)

The MuScat experiment was created to measure the multiple scattering of 180 MeV muons as input to the cooling studies of muons [Neuffer, Proc. Workshop on Beam Cooling, Montreux, 1993 (CERN Rep. 94-03, 1994) p.49] for a neutrino factory and a muon collider. Data were collected in the M11 beam line in 2000 and in M20 in 2003 for a variety of targets. The analysis of these for multiple scattering is now complete and in the process of being published. The results are summarized here.

The experiment

The experiment (see Fig. 64) has been described in detail in previous Annual Reports, so only a short description is given here. The technique employed was to prepare a narrow collinear muon beam by collimation, and to use it to illuminate a variety of target materials. The position of the outgoing particles was measured after travelling a sufficient distance that the position and angle were highly correlated.

The key components are the collimation system, a wheel with a selection of solid targets and an optional liquid hydrogen (LH_2) vessel, a scintillating fibre tracker, and the trigger scintillators, in particular two overlapping fingers in front of the collimation system, S1A and S1B. In addition to these the TINA (TRIUMF iodide of sodium) calorimeter [Waltham *et al.*, Nucl. Instrum. Methods **A256**, 91 (1987)] was useful to help understand the system. There were also some extra scintillators employed as veto counters. The complete list of targets employed and the number of data events used in the analysis are shown in Table IX.

GEANT4 model

The detector performance has been modelled using GEANT4.7.0p01. This toolkit was used to make a complete description of the geometry shown in Fig. 64.

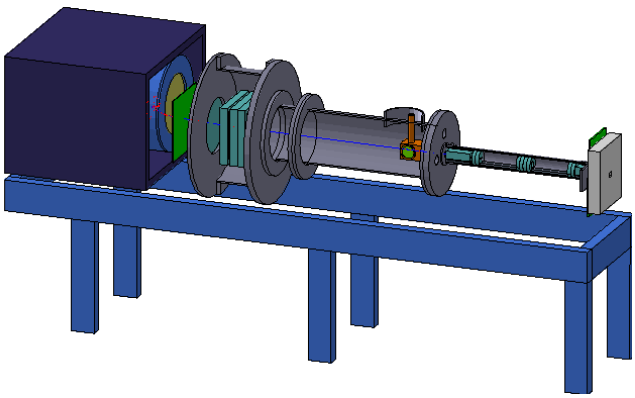

Fig. 64. The MuScat detector, from a GEANT4 model.

Table IX. The targets used and the number of events selected for each.

No.	Material	Thickness, mm	Events
0	Lithium	12.78	805,239
1	Lithium	6.43	1,224,756
2	Lithium	6.40	882,449
3	Lithium	12.72	1,215,336
4	Beryllium	0.98	500,766
5	Beryllium	3.73	1,186,528
6	CH_2	4.74	802,426
7	Carbon	2.50	801,899
8	Aluminum	1.50	1,201,280
9	None	0	2,259,476
10	Iron	0.24	845,020
11	Iron	5.05	1,225,435
	Empty H_2	109.0	2,694,511
	H_2	109.0	2,267,683
	Empty H_2	159.0	812,730
	H_2	159.0	1,127,045

Considerable attention has been attached to the simulation of the collimator system and the fibre tracker, which are critical to the experiment and whose performances are sufficiently complex that they are hard to extract from the data alone. Figures 65 to 67 show a comparison between the data and the model to illustrate the quality of the simulation of these two elements. In Figs. 65 and 66 are comparisons between data and the GEANT model with no target and the thick iron target, respectively.

In Fig. 67 (left), the distribution of ADC counts recorded on all channels of the scintillating fibre tracker is shown. The pedestal is clearly visible, with a peak due to single photo-electrons at around 600 counts

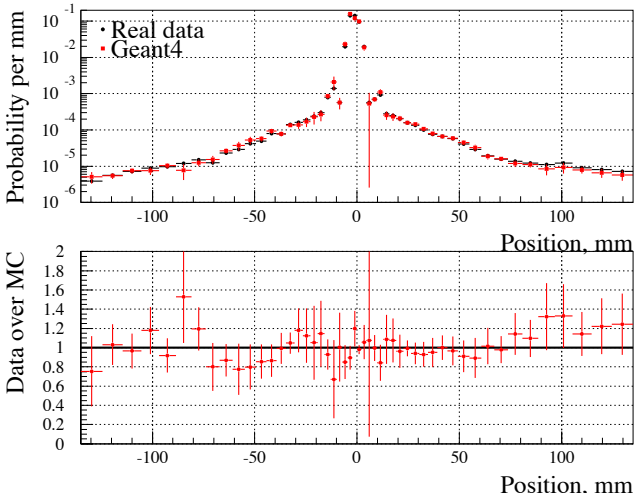

Fig. 65. The distribution of particles at detector plane 1 in data and simulation for no target. The error bars include estimated systematic uncertainties.

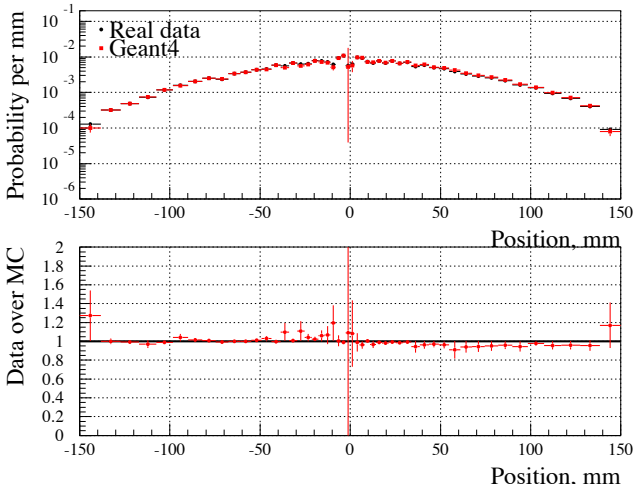

Fig. 66. The distribution of particles at detector plane 1 in data and simulation when the thick iron target is in place.

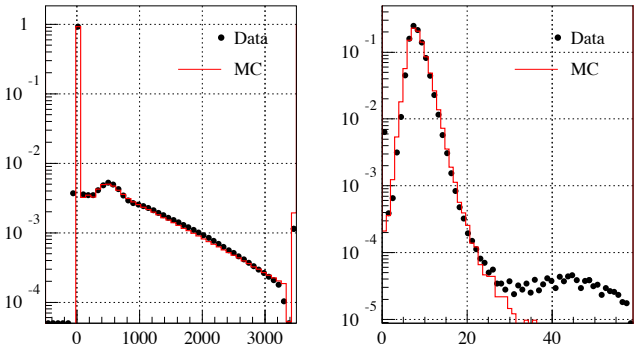

Fig. 67. Left: The number of ADC counts on every channel in data and simulation with the thick iron target. The peak at 600 is due to single photo-electrons. Right: The distribution of the number of fibres with a signal of over 0.2 photo-electrons observed in data and simulation.

which was used to measure the gain. The upper edge is cut off by the saturation of the ADCs. The simulation includes these effects and shows reasonable agreement.

The distribution of the number of reconstructed fibres with signals in data and simulation is shown in Fig. 67 (right). The data have events with no fibres hit which are not reproduced by simulation. These are trigger accidental coincidences. There are also events with several times the normal number, which arise from multiple tracks. Both types of events are removed in analysis.

Beam properties

There has been no attempt to simulate the beam line. However, the X distribution of the observed beam has a very small dependence upon the initial beam configuration, and for Y it is totally negligible. The beam divergence is instead determined by multiple scattering in the S1A and S1B scintillators, which guarantees a minimum spread, followed by the collimation system which limits the maximum angle.

Beam momentum determination A special run was taken with the momentum of the second dipole in the beam line turned down by 2%. This meant that the forward muons normally accepted have a large contamination from other species. The presence of multiple particle types has been used to measure the beam momentum. The time of arrival of the cyclotron signal relative to S1B is shown in Fig. 68. The major peaks are at 500 (pions), 650 (muons), 750 (protons) and 900 (electrons). In general the fastest particles give the largest times, because what is measured is the arrival time of the cyclotron signal after S1B. In the case of protons, the velocity is only 0.2 c, and they arrive seven beam crossing periods late. The width in the electron and pion signals is similar, but the others are broader. For protons this is because the very low velocity leads to a much larger spread in time, while the muon arrival time depends upon the decay point. There is a distinct peak of muons which were produced before the first bending magnet.

The momentum of the beam has been estimated by fitting the arrival times of all four particle species. Three parameters are required for this: the time offset (defined by the arrival time of a particle going at the speed of light), the length of the beam line and the beam momentum. The results are shown in Fig. 69, where a momentum of 168.9 MeV/c is found and the four points are seen to be consistent. This run was taken with the final dipole field reduced by 2%, so under normal running conditions the beam momentum is 172 ± 2 MeV/c.

The spread in momentum can be estimated by noting that it affects the velocity of pions but not electrons. The quadrature difference in width of the pion and electron peaks calculated as in Fig. 68 but after accounting for small time-walk effects gives the spread in momentum as being between 1.0 and 1.2 MeV/c.

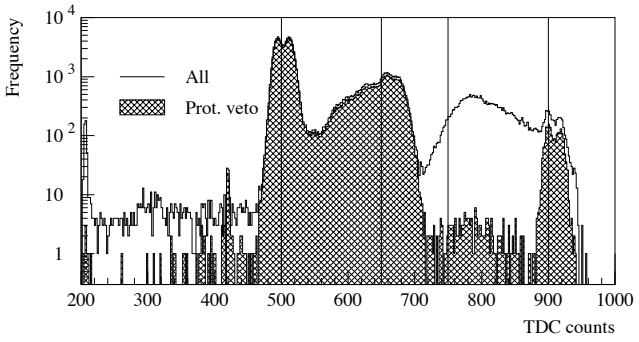

Fig. 68. The time of arrival of the beam cycle signal relative to the S1B scintillator for run 177, which was tuned to have a mixed particle content. The four lines guide the eye to pions, muons, protons and electrons. The open histogram is for all events that are in time on S1B, and the hashed area for events that meet a tighter requirement on S1B, within 0.25 ns of expected, which excludes protons. A double peak structure can be seen for the precise peaks; this is not understood.

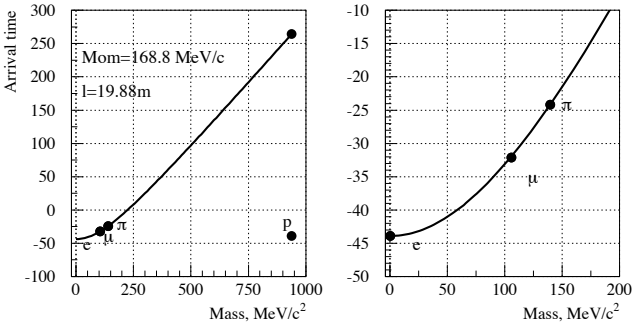

Fig. 69. Fitting the beam momentum from the observed peaks using the cyclotron signal. The negative of the arrival time of the cyclotron signal is plotted; for protons a point is shown both at the measured time and delayed by seven beam cycle periods.

Beam composition The recorded sample under normal conditions has a large proportion of muons. This can be seen in Fig. 70. Protons are ranged out in the S1A trigger, and not generally recorded. This figure shows a somewhat worse time resolution than in Fig. 68, which is not understood but was constant for the data used for the main analysis.

The muon fraction is further raised by demanding that the recorded time of the TOF signal is within the section labelled μ in the figure. The energy recorded in TINA for the subset of events within its acceptance is used to evaluate the purity of this sample and a 0.8% pion contamination is found.

Analysis method

Event selection The selection of events for analysis requires that they pass a number of selection criteria. Firstly the high voltage must have been nominal and the data acquisition in a normal state. Then we require that the event was not taken during a period identified as having a problem with the time of flight system.

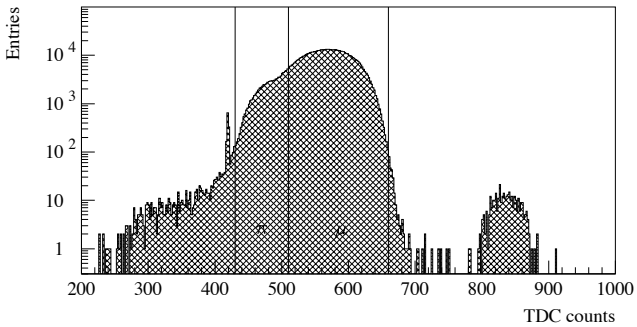

Fig. 70. The time of arrival of the beam cycle signal relative to the S1B scintillator for run 290, an ordinary run with no target. The graph corresponds to events where the digitized time from S1B was correct. The section labelled μ contains those events used for the scattering analysis. The small peak to the right contains electrons. The resolution is slightly worse than in Fig. 68; this is not understood.

Next the number of reconstructed points on the first plane of the tracker is required to be one or two; more hits would make the position of the muon very ambiguous. Then the summed signal from the two internal veto scintillators had to be consistent with the pedestal, and the time from S1B within a few counts (0.2 ns) of nominal.

The hit with the largest light yield is taken as the estimated particle position at each detector plane. Finally, the positions of the hits on the first and second planes are required to be consistent with the hypothesis of a particle coming from the target. The second plane is about 4% further from the target, so it is required that 0.96 times the Y position on the second plane be within 5 mm of the Y position on the first plane. This procedure is simpler than performing a full track fit, and less dependent upon alignment systematics.

Deconvolution technique It is possible to compare the distributions of hits at the first detector plane. However, the more fundamental quantity is the angle through which the particle scattered in the target, and the effects of beam width, efficiency, resolution etc. must be corrected in order to see this. This deconvolution is done using the GEANT4 simulation, with the following approximate formula:

$$\overline{D} = \overline{B} + \overline{D_\pi} + \overline{\overline{R}} \cdot \overline{\overline{\epsilon}} \cdot \overline{\Theta} \qquad (1)$$

where $\overline{D}$ is the observed position data, $\overline{B}$ a background of particles not passing through the target, $\overline{D_\pi}$ is the contamination from pions, $\overline{\overline{R}}$ is the response of the detector to a particle deflected through angle θ_y, $\overline{\overline{\epsilon}}$ is the efficiency of the detector for particles deflected through angle θ_y, and $\overline{\Theta}$ is the projected scattering distribution in the target.

The background, $\overline{B}$, is found from simulation as those muons which managed to meet the trigger conditions without passing through the target. There are typically 0.125% background events. The pion contamination, $\overline{D_\pi}$, is taken from the data pion sideband. The default value is 0.8% pions, and as the sideband is approximately 50% pions, a 1.6% admixture of the data sideband is added to the simulation.

The response and efficiency matrices, $\overline{\overline{R}}$ and $\overline{\overline{\epsilon}}$ are taken from simulation. The efficiency is found by running GEANT4 twice. The first run is a simulation of the target only, illuminated by a monochromatic collinear beam of muons. This is used to find the true $\overline{\Theta}$ distribution in GEANT4. The second run is the full simulation, including trigger and tracking acceptance cuts. The distribution $\overline{\Theta}$ for those muons accepted is calculated, and the ratio of these is $\overline{\overline{\epsilon}}$. In the above formula it is treated as a diagonal matrix. Finally, $\overline{\overline{R}}$ is filled as a 2D matrix, with each accepted simulated event being entered at a point given by its θ_y and the Y position at the first measurement plane. It therefore gives the probability of a given measured position for each possible true deflection angle.

The equation is solved for $\overline{\Theta}$, imposing a requirement of symmetry about $\theta = 0$, using Minuit [CERN Program Library entry D506], which also finds errors and correlations. It has been checked that the technique is mathematically correct, in that if given simulated data as an input the scattering distribution from that simulation is recovered.

This formalism does not explicitly include the effect of energy losses and scattering in the X direction. The matrices $\overline{\overline{R}}$ and $\overline{\overline{\epsilon}}$ therefore depend on the simulation of multiple scattering and energy loss in the GEANT model. In particular, the probability that a particle completely misses the detector in the X direction as a function of its Y angle must be taken from simulation.

The problem of instabilities in the deconvolution has been dealt with by reducing the number of bins in the deconvoluted data, where 21 are used, compared to the raw data, which has 57. Furthermore the condition of symmetry is enforced in the fit, so there are essentially only 11 bins. Finally, the outermost bin in true scattering angle runs from 115 mrad to π, but is very weakly constrained by the data as the majority of events in this bin are not recorded. It also has a strong dependence on the simulated prediction of the fraction recorded. It is not shown in the plots which follow.

The results

Comparisons at detector level Data taken with no target, an empty hydrogen vessel or a very thick iron target are not of great intrinsic interest, but were necessary to understand the detector. The first, the bare collimator distribution, is shown in Fig. 65. The final results are based upon deconvoluting the data using the simulation, and so discrepancies here will translate into systematic errors on the results. In the case of hydrogen data, the equivalent of the bare collimator is the empty target vessel. The distributions obtained for this in data and simulation are shown in Fig. 71 for the case of the longer target configuration.

The error bars shown in these plots are statistical only for the data but are a combined statistical and systematic error on the simulation points. This systematic error explicitly includes the difference between these plots, and so by construction all ratios must be compatible with one to within one combined error.

The other control plot is Fig. 66, which shows the results for a thick iron target, of 28% X_0. The agreement is well within 10% in most bins, with the centre and the edge bins showing differences around 20%. As the edge bins have also got a large background subtraction, the region of the detector used for analysis and

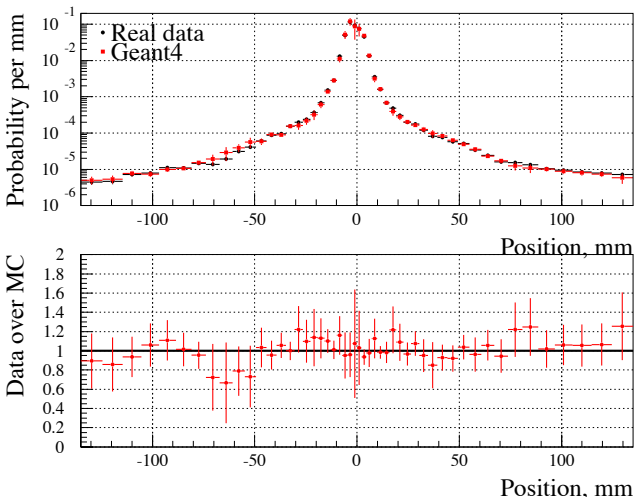

Fig. 71. The distribution of particles at detector plane 1 in data and simulation for the empty H_2 vessel in the 150 mm position.

subsequent figures is restricted to the central 270 mm.

The raw distribution at detector level for a few of the targets is now shown. Figure 72 shows the combined data from the two thin lithium targets. The thickness of this sample corresponds to the second lowest fraction of a radiation length of material used, and it therefore has a narrow distribution. GEANT tends to overestimate the distribution, starting from about 10 mrad. Note that outside about 100 mm the distribution is completely dominated by the scattering from the collimator (see Fig. 65) and the contribution from the lithium is negligible. Thus the convergence of data and simulation in the tails is more related to the simulation of the collimator than the physics of scattering.

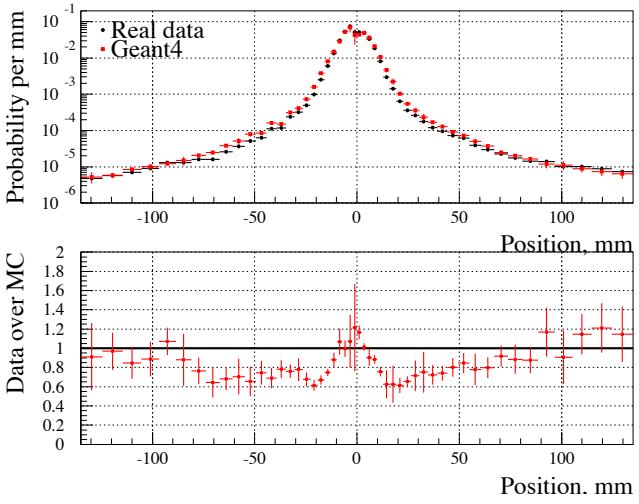

Fig. 72. The distribution of particles at detector plane 1 in data and simulation for thin lithium, combining both targets. This distribution is used to check the agreement of our data with GEANT.

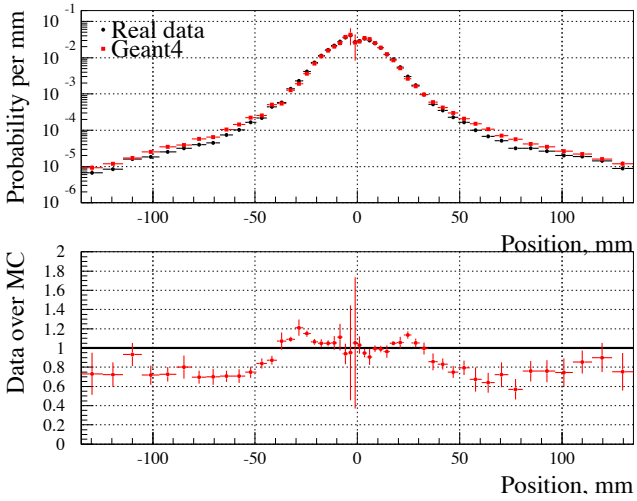

Fig. 73. The distribution of particles at detector plane 1 in data and simulation for thin iron, target 10.

The thin iron target, Fig. 73, is the highest Z target studied. The GEANT description is better than for any of the lighter targets, but there is here a small region below 40 mm where the scattering distribution is underestimated which is seen in no other target.

The final comparison presented at the level of the detector is for the longer hydrogen target, Fig. 74. This resembles the lithium target, but the differences between data and simulation are more pronounced, with the observed distribution less than half the predicted level at ±40 mm.

Deconvoluted results The deconvolution procedure described above is applied to each of the targets. A series of systematic effects are allowed for, and plots for many of the targets are presented in Figs. 75 to 81. In each case the statistical error is indicated with an inner error bar, and the combined statistical plus systematic error is indicated with the outer error bar.

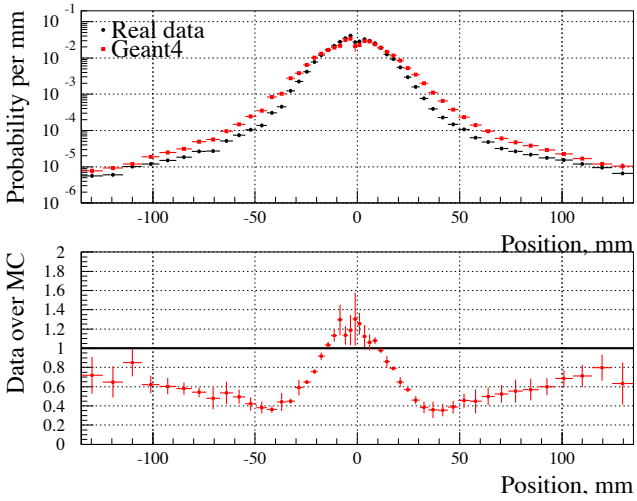

Fig. 74. The distribution of particles at detector plane 1 in data and simulation for 159 mm of liquid H_2.

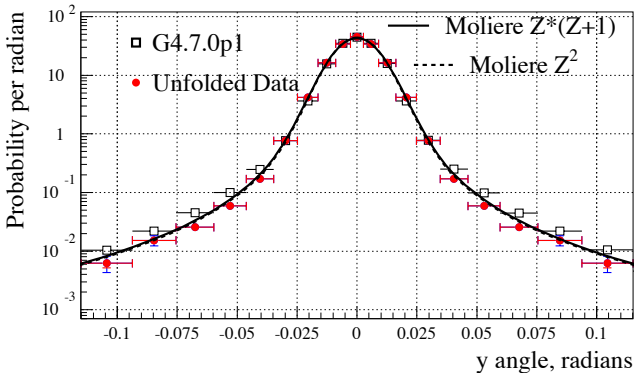

Fig. 75. The projected scattering angle distribution in data and simulation for thin iron, target 10.

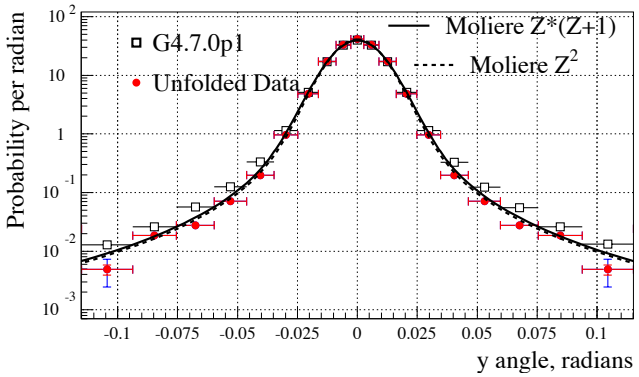

Fig. 76. The projected scattering angle distribution in data and simulation for aluminum, target 8.

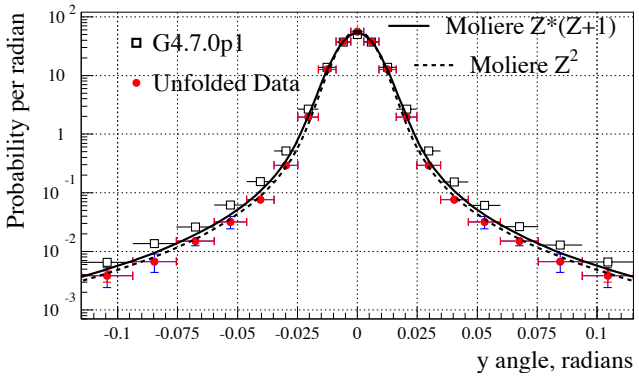

Fig. 77. The projected scattering angle distribution in data and simulation for carbon, target 7.

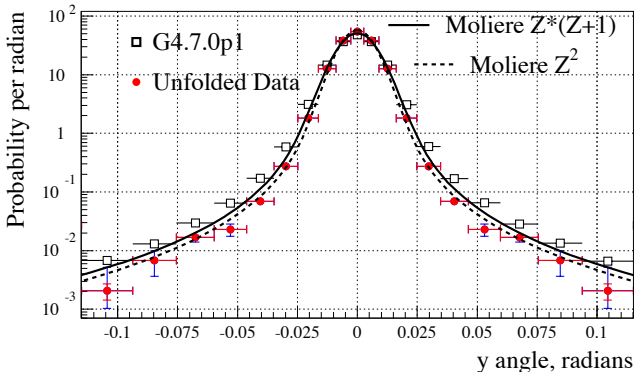

Fig. 78. The projected scattering angle distribution in data and simulation for thick beryllium, target 5.

In most cases the statistical errors are only important for regions of the distribution where the probability of arrival is below about 0.1 per radian.

The plots have two smooth curves superimposed: the solid line represents the Moliére calculation with a $Z \times (Z+1)$ factor for the large angle scatters, as proposed by Bethe [Phys. Rev. **89**, 1256 (1953)], and the dashed line represents the same calculation using a Z^2 term. The difference corresponds to scattering solely on the nucleus, or also on the electrons. Note that the kinematics of scattering prevent a muon from making a single scatter from a free electron through an angle greater than m_e/m_μ, or 5 mrad. We therefore expect that for the description of the tail region, above 15 or 20 mrad, the Z^2 term will be more appropriate.

Thin iron The data are shown in Fig. 75. The two Moliére models are almost indistinguishable, and provide a good description of the data. In general, the GEANT4.7.0p1 simulations are somewhat in excess of the data above 35 mrad. Errors are around 5%, growing to 30% in the final bin shown.

Aluminum The data, Fig. 76, are rather similar to the iron, with an overestimation of the tail by GEANT4 of around a factor of two.

Carbon The data, shown in Fig. 77, reveal a visually apparent distinction between the Moliére models. Furthermore, the GEANT simulation appears to have an excess compared with data starting at lower angles, around 20 mrad, than it did for iron.

Polyethylene The data for this target resemble beryllium, with a similar overestimate from GEANT of the scattering. They are not shown. The largest systematic contributions come from the simulated collimator description.

Beryllium The thick target data are shown in Fig. 78. The GEANT model overstates the tails by approximately a factor of two. Of the two Moliére models, the Z^2 is slightly preferred. No distinction was possible for materials with higher Z as the models were similar. The thin beryllium has larger errors, owing to the large background subtraction required there, and is not displayed.

Lithium There were two pairs of lithium targets with very similar thicknesses. The data for the thicker pair are combined in Fig. 79. The Moliére model with a Z^2 term provides a reasonable description of the data, but the $Z \times (Z+1)$ Moliére model is now clearly disfavoured. GEANT continues to have tails about a factor two above the data. The data from the thin lithium targets have large systematic and statistical errors in

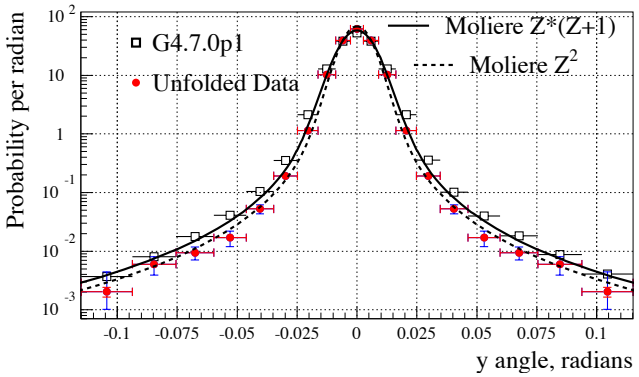

Fig. 79. The projected scattering angle distribution in data and simulation for thick lithium, both targets combined.

the tails, owing to the large fraction of background which has been accounted for in the deconvolution, and are not shown.

Hydrogen For 109 mm of hydrogen it can be clearly seen in Fig. 80 that neither Moliére model accurately describes the data. The Z^2 model understates the region below around 25 mrad, and above 60 mrad, although here the errors are much larger. GEANT4.7.0p01 predicts too much scattering, by a factor of around 4 at 50 mrad.

The data from the ELMS model [Allison, J. Phys G Nucl. Part. Phys. **29**, 1701 (2003)] are also compared with our results. These seem to show good agreement at all but the high angle. This region has the largest systematic errors.

It can be clearly seen in Fig. 81 that neither Moliére model accurately describes the data for the long hydrogen target. The Z^2 model seems correct beyond around 40 mrad, but in the multiple-scattering dominated region the $Z \times (Z+1)$ model is much more appropriate. GEANT4.7.0p01 predicts too much scattering, but close examination reveals that the excess is less than for the thinner sample.

Overall, we see that when the two Moliére models are distinguishable, i.e. when Z is small, the data are described by the $Z \times (Z+1)$ in the Gaussian core, while

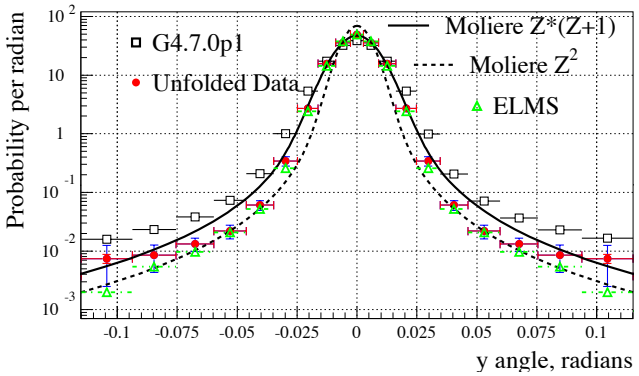

Fig. 80. The projected scattering angle distribution in data and simulation for 109 mm of liquid H_2.

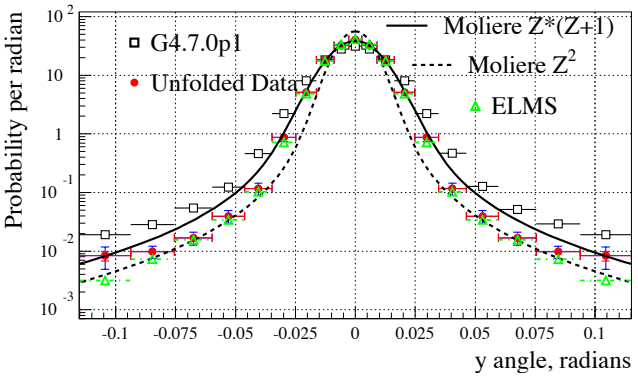

Fig. 81. The projected scattering angle distribution in data and simulation for 159 mm of liquid H_2.

the tails show better agreement with the Z^2 version. This emphasizes that the difficulty of describing the data is greater at low Z.

GEANT4.7.0p01 typically predicts about a factor two more scattering tail than is observed. This is not a very large effect given that the data cover 4 orders of magnitude. However, in the case of liquid hydrogen the discrepancy grows to be a factor 4.

The ELMS simulation describes hydrogen very well.

Systematic errors

Systematic errors are evaluated by performing the complete analysis with different treatment of the data. The difference with the main results is taken as an estimate of systematic error. All errors are combined in quadrature.

Collimator description Three different techniques are used to evaluate the impact of differences between the collimated distributions seen in Fig. 65. The largest systematic errors are generally from uncertainty in our understanding of the collimated beam.

Collimator difference The bare collimator distribution seen in simulation is subtracted from the observed data. This residual is then added to the simulated distribution for whichever target is currently under study. This is not completely correct, as it ignores the scattering in the target, but it provides an estimate of the systematic effects.

Collimator deconvolution The deconvolution to find the underlying scattering distribution is performed on the data with no target present. This would yield a delta function, but is not due to bin width effects and discrepancies between data and simulation. The same is done in simulation, and the difference of the two is found. This difference is due to poor modelling of the collimated beam. The deconvolution for any given target is then repeated with this difference distribution included as an extra convolution term on the right hand

side of Eq. 1. Any changes in the results are taken as systematic errors.

Internal veto scintillators The collimation system has two internal veto scintillators mounted just before the second collimator. The data show a good separation between pedestal and hits, but there is no complete cross-check on this. The simulated efficiency is lowered to 90%, (which also provides a slightly better description of the scattering distributions) and a systematic error is generated.

Detector alignment Detector misalignment relative to the simulation will cause errors in the deconvolution.

Detector *X* alignment Any credible X misalignment will have negligible impact.

Detector *Y* alignment A transverse shift of the detector of 0.1 mm is allowed as a systematic error. The size comes from inspection of Fig. 65.

Detector *Z* alignment The Z position of the detector affects the widths of the distribution. From a combination of studying internal distributions in the tracker and knowledge of the detector construction, a systematic error of 5 mm has been assigned.

Detector modelling

Thick target comparison The muon tracking efficiency maps directly into the scattering distribution, and as such it must be well controlled. The distributions in data and simulation observed with the thick iron target present (Fig. 66) are used to monitor this. It is conservatively assumed that all differences are due to efficiency, and so the ratio of these distributions is used as an efficiency correction. The change in the unfolded results when this is applied is regarded as a systematic error.

Cross-talk suppression The default cut selection allows one or two hits to be reconstructed on the first detector plane. When we require exactly one the probability of picking the wrong one is reduced. The analysis is repeated with this requirement and the difference is taken as a systematic error.

Pion contamination As discussed above, a pion background of 0.8% is estimated. However, this comes from the observation that the energy deposition in TINA has tails to the left of the muon peak; some of this background will arise from sources other than pions. The most extreme alternative assumption is that there are no pions present, and this is used to estimate a systematic error.

Deconvolution matrix The matrix used to relate true scattering angle to measured position is taken from simulation. It depends upon the physics in that simulation, especially scattering in the X direction. This dependence is reduced by re-weighting all the simulated events as a function of the space angle scatter with an ad-hoc simple function which moves GEANT4 towards Moliére Z^2 scattering above about 40 mrad. The central values of all the fits have been obtained using this procedure. A systematic error is assigned by comparing with the unweighted GEANT, except in the case of hydrogen where we have the ELMS simulation, and the alternative distribution is GEANT4 re-weighted to match the predictions of that. This is typically the largest systematic error at the edge of the deconvoluted distributions.

Conclusions

These data allow the validation of codes to calculate multiple scattering in the regime relevant for ionization cooling. In general Moliére scattering provides a good description, but for Z below about 4 there are differences which may be important. In particular, for hydrogen, neither Moliére model used is appropriate. The ELMS simulation provides a good prediction of the deconvoluted hydrogen distributions.

The data show noticeable deviations from the predictions of the GEANT4.7.0p01 simulation code, which tends to overstate the scattering tail by about a factor of two, and more strongly the lower the Z of the material. For hydrogen it is about a factor of 4.

The discrepancies observed previously [Andrievsky *et al.*, J. Phys. (USSR) **6**, 279 (1942)] are not confirmed. Indeed, the scattering predicted by the GEANT simulation needs to be reduced to match the data, not increased.

With this, the main original aim of the experiment has been achieved.

Experiment 909
Isospin symmetry breaking in superallowed Fermi β-decays

(G.F. Grinyer, Guelph)

Precision measurements of the ft values for superallowed $0^+ \rightarrow 0^+$ Fermi β-decays between isobaric analogue states provide demanding tests of the standard model description of electroweak interactions. To date, superallowed ft values have been determined at the $\pm 0.1\%$ level for nine nuclei between ^{10}C and ^{54}Co. Once corrected for small radiative and isospin symmetry-breaking effects, their consistency has confirmed the conserved vector current (CVC) hypothesis at the level of 3×10^{-4}. From these studies, the Cabibbo-Kobayashi-Maskawa (CKM) matrix element, V_{ud}, can be derived by comparing the β-decay data with pure leptonic muon decay. Combining the results from superallowed Fermi β-decay studies with the present knowledge of V_{us} and V_{ub}, indicates a violation of CKM unitarity by 2.4 standard deviations

[Hardy and Towner, Phys. Rev. **C71**, 055501 (2005)]. Although recent measurements indicate the accepted value of V_{us} may ultimately be the source of this discrepancy, these results are presently under intense scrutiny and must still be confirmed by independent measurements.

Before a definitive conclusion can be reached, all uncertainties contributing to the unitarity test must be carefully scrutinized and, if possible, reduced. For V_{ud}, the dominant uncertainties are those associated with theoretical corrections to the ft values, and the search for systematic effects has focused on the nuclear-structure dependent δ_C corrections that account for the breaking of isospin symmetry by charge-dependent forces in the nucleus.

Experiment 909 involves a series of measurements with the 8π γ-ray spectrometer and the scintillating electron positron tagging array (SCEPTAR) aimed at constraining the above-mentioned isospin symmetry-breaking corrections in superallowed Fermi β-decays. This program will take advantage of the unique beams of radioactive ions available at ISAC to study particular decays in which the predicted δ_C corrections show the greatest model sensitivity. An initial focus of Expt. 909 will be on half-life and branching ratio measurements for ^{34}Ar, with the aim of establishing the superallowed ft value at the $\pm 0.1\%$ level. The first objective will be to improve the current half-life precision by approximately one order of magnitude. These measurements will be carried out by collecting samples of ^{34}Ar at the centre of the 8π and following their decay for $\sim$30 half-lives by time-stamping γ-rays emitted from excited states in the daughter, ^{34}Cl, populated in Gamow-Teller decay branches of ^{34}Ar.

Tests of the experimental techniques to be employed in Expt. 909 were carried out with radioactive ^{26}Na beams. This isotope was chosen because: i) high yields were available from existing ISAC surface ion sources, ii) the half-life ($\sim$1.07 s) is similar to ^{34}Ar ($\sim$0.84 s), iii) the daughter ^{26}Mg is stable, and iv) $\sim$99% of ^{26}Na β-decays are followed by an 1809 keV γ-ray transition in ^{26}Mg, facilitating tests of the γ-ray lifetime technique to be employed for ^{34}Ar. To this end, a beam of ^{26}Na was delivered to the 8π spectrometer in April, 2004. A sample decay curve obtained from a gate on the 1809 keV γ-ray in ^{26}Mg is presented in Fig. 82. Before the half-life of ^{26}Na can be reliably extracted from these data and compared to the high precision result obtained previously at ISAC [Grinyer *et al.*, Phys. Rev. **C71**, 044309 (2005)], it is necessary to quantify all rate dependent systematic effects. A Monte Carlo simulation has recently been developed to investigate detector pulse pile-up over a wide range of variables such as detector count rate, detector time

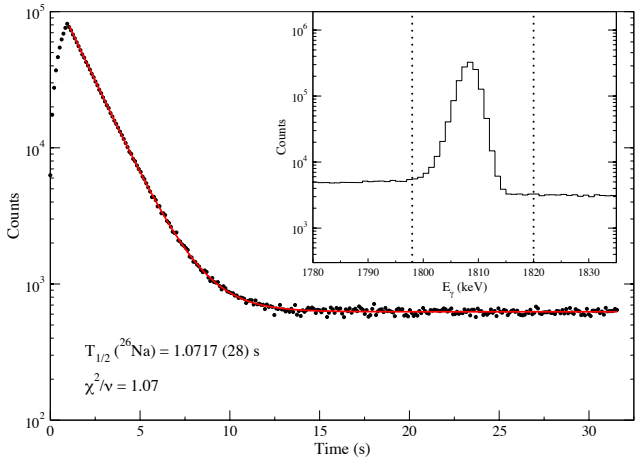

Fig. 82. Typical growth and decay curve of ^{26}Na obtained at the 8π spectrometer from a γ gate on the 1809 keV photopeak events in the γ-ray singles spectrum (inset).

resolution, γ-ray multiplicity, detector solid angle, and pile-up time (shaping time). The results of this simulation and the subsequent correction for these effects in the ^{26}Na data set will prove invaluable in the determination of the half-life of ^{34}Ar where a β counting measurement is not ideal due to the fact that the daughter ^{34}Cl also β-decays with a similar half-life ($\sim$1.53 s). The comparison between the β and γ half-life determinations for ^{26}Na will provide fundamental insight into the systematic effects such as detector pulse pile-up that have not allowed previous γ-ray lifetime measurements to achieve the level of precision ($\sim$0.05%) necessary for distinguishing between the model dependencies of the isospin symmetry breaking corrections described above.

In May, 2005 a beam of ^{34}Ar at a rate of $\sim$100 s^{-1} from the ISAC electron cyclotron resonance (ECR) source was delivered to the 8π spectrometer and SCEPTAR. The yield of ^{34}Ar observed was 3 orders of magnitude below the minimum yield of 10^5 ^{34}Ar s^{-1} required to improve upon previous measurements of the ^{34}Ar half-life. A measurement through the β activity was explored through the use of SCEPTAR, however, the large covariance between the half-lives of the parent (^{34}Ar) and daughter (^{34}Cl) proved impossible to overcome at this beam rate. Instead, 2 shifts of ^{26}Na beam was delivered to SCEPTAR and the 8π to further explore systematic effects of the scintillator array. The half-life of ^{26}Na obtained with SCEPTAR will be directly compared to both ^{26}Na half-life determinations made at the 8π and the general purpose station (GPS). A sample decay curve obtained from one ring of SCEPTAR consisting of 5 SCEPTAR detectors is presented in Fig. 83. A ring by ring comparison of the half-life obtained is one method of ensuring potential systematic effects are minimized (Fig. 83 inset). In the remaining 3 days of the experiment, a beam of 10^4 ^{35}Ar s^{-1}

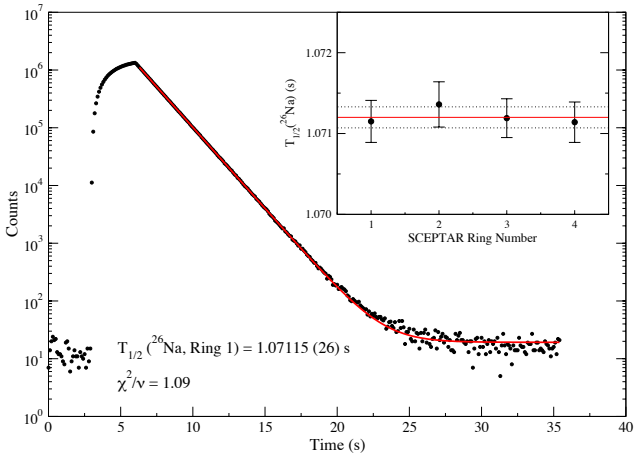

Fig. 83. Typical growth and decay curve of ^{26}Na obtained from one ring (5 detectors) of SCEPTAR in a single run lasting ∼2 hours. Each SCEPTAR ring will be used as an independent measurement of the ^{26}Na half-life (inset).

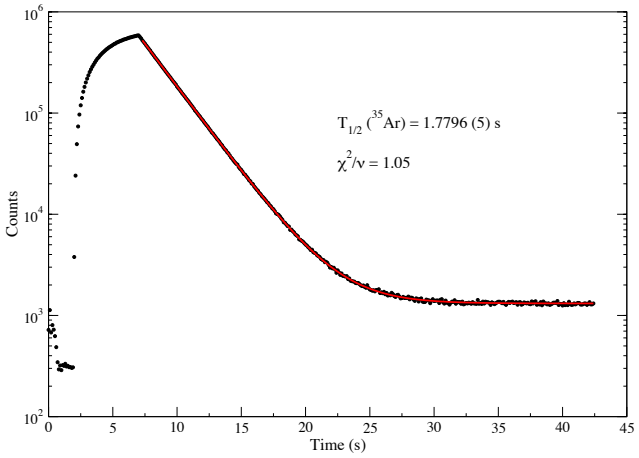

Fig. 84. Typical growth and decay curve of ^{35}Ar obtained from the sum of all 20 SCEPTAR plastic scintillators for a single run lasting ∼6 hours.

was delivered to the 8π and SCEPTAR. While not a superallowed decay, the rate of ^{35}Ar from the ECR source was sufficient to establish the half-life of ^{35}Ar using SCEPTAR to a statistical precision of ∼0.01%. A sample decay curve obtained from a sum of all 20 SCEPTAR detectors is presented in Fig. 84. Analysis of these experiments is ongoing and will provide a demanding test of the SCEPTAR array.

A beam of ^{34}Ar of sufficient intensity ($>10^5$ s^{-1}) to perform the half-life and β-branching ratio measurements to establish the ft value for this superallowed decay to better than 0.1% is anticipated to be delivered from the ISAC FEBIAD ion source in the fall of 2006.

Experiment 920
Nuclear moments of ^{131}La determined by on-line laser spectroscopy

(H.A. Schuessler, Texas A&M)

Off-line runs

During the year we had three OLIS runs for La spectroscopy. The main purpose was to compare the characteristics of a new mesh assembly in the fluorescence detection region containing a four plate detector with the previous version of a mesh only. The new mesh assembly was designed according to a TAMU arrangement, and constructed at McGill. It has gradient electrodes intended to reduce the large voltage gradient present at the entry to the mesh itself. The assembly also is constricted with an entrance and exit skimmer electrode, each built with 4 quadrants so that the ion beam position could be centred accurately. This arrangement worked well, and we decided to use it for our on-line run on July 29 – August 3.

On-line runs

As requested, Expt. 920 had been put at the beginning of an on-line cycle. This way we could possibly have a stable beam, before bombarding the ion source with protons. We needed to make such a measurement of ^{139}La for reference of the isotope shift, and for optimal tune-up of our laser spectroscopy experiment. For this purpose the on-line ion source had been spiked before the run with stable lanthanum. Unfortunately the ion source did not get hot enough to produce a stable beam (the target heating from the proton beam was off for this experiment). The required temperature of 2200°C can, however, be obtained by having a radiation shield installed on the ion source, and we recommend this for our next run as the simplest way of increasing the temperature. After this we proceeded with the on-line part of the experiment.

The aim was to observe the hfs of a short-lived La isotope in the range of A = 130–135. We obtained a good beam of ^{131}La and performed the measurement. We needed about 12 hours of averaging to obtain a reasonable S/N ratio. Before giving the results below, necessary additions to the experiment before a future run will be described: namely to enlarge the solid angle of detection and to stabilize the laser with an improved iodine lock. These tasks will be carried out during spring, 2006.

Introduction

Collinear fast-beam laser spectroscopy continues to provide detailed nuclear structure information. At present, measurements of the hyperfine structure (HFS) of the atomic spectra of short lived isotopes are ongoing at several nuclear facilities, in particular at

ISOLDE (Switzerland), GSI (Germany), JYFL (Finland) and RIKEN (Japan). We report here on our first measurements with collinear fast-beam laser spectroscopy at the ISAC facility at TRIUMF. This nuclear facility is able to produce intense beams of radioactive isotopes of the rare earth elements with unprecedented intensities. In particular the neutron deficient region below the $N = 82$ shell closure is of interest and contains around $N = 74$, an unexplored region of nuclear deformation predicted by both the droplet model and the HF-BCS method. In these calculations the change in deformation on the neutron deficient side is more pronounced than for the neutron rich isotopes. While an extensive amount of experimental information on nuclear charge radii of short lived isotopes is available for the rare earth elements with $N > 82$, only a few isotopes below shell closure could so far be investigated with laser spectroscopy. This is due to the low production yields, which require large proton beam currents, for the sufficient production of radioactive isotopes in this region.

In this paper we report the measurement of the HFS–constants of ^{131}La as an initial step to further exploring this region. Our work is an extension of our earlier off-line experiments on $^{135,137-139}$La at JAERI (Japan) to on-line laser spectroscopy.

Experiment

The radioactive isotope ^{131}La was produced by means of a fusion evaporation reaction using a tantalum target and a 35 μA proton beam from the TRIUMF cyclotron. A surface ionization source operated at about 2200°C and produced the on-line ion beam. After mass separation the yield of the ^{131}La was determined to be about 2×10^7 ions/s by measuring several γ-rays. The half life of ^{131}La is $T_{\frac{1}{2}} = 59$ min.

Our collinear fast-beam laser spectroscopy set-up is the standard one for ion fluorescence detection. A copropagating laser beam excited the La^+ ions from the lower metastable level to the upper state. The La^+ ion beam was accelerated to 30.6 keV and post accelerated by a set of acceleration electrodes to be at resonance with the laser light in the interaction region. The laser frequency was kept constant and the ion beam was Doppler tuned through optical resonance. Excitation at 538 nm and detection at a different wavelength was carried out. The fluorescent light was collected by a lens and a spherical mirror onto a cooled photomultiplier. Since excitation and detection were effected at different wave lengths, colour glass filters effectively suppressed stray light from the laser and collisional excitation of the fast ion beam. The signal from the photomultiplier was counted during the voltage scans using multi channel scaling and recorded using the TRIUMF computer based data acquisition system. A dye laser

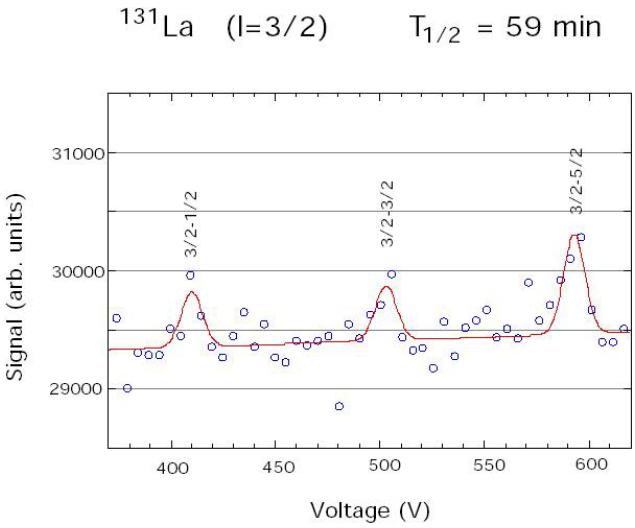

Fig. 85. HFS spectrum.

operating with Rh 110 and pumped by an argon ion laser was employed and locked to the Doppler broadened I_2 line at 18591.1042 cm^{-1}. The data were obtained from scans typically about 500 V wide having a step size of 5 V/channel and a dwell time of 1.5 s. A HFS spectrum of the 538 nm transition of ^{131}La is shown in Fig. 85. Because the nuclear spin is I = 3/2, the spectrum has only three HFS components. The relevant F quantum numbers are indicated with the lower state first and the upper state second. The observed peak intensities confirm the assignment of HFS components and are close to the theoretical value of 3:2:1.

Discussion

Lanthanum isotopes have been of particular interest because they are located at a so called transitional region, where the quadrupole deformation increases as the neutron number decreases from N = 82 (^{139}La). Moreover, a triaxiality is suggested theoretically around A = 130 [Tajima, Nucl. Phys. **A572**, 365 (1994)].

From the observed peak intervals of the 538.2 nm transition of ^{131}La, the hyperfine structure constants of the $5d6p\,^3D_1$ level were obtained to be A = 271(8) MHz and B = –86(10) MHz. The nuclear moments of ^{131}La were derived from these hyperfine constants and the known magnetic moment of the stable ^{139}La, $\mu(139) = +2.7830455(9)$ nuclear magneton [Raghavan, At. Data Nucl. Data Tables **42**, 189 (1989)], and the quadrupole moment, Q(139) = +0.20(1) barn [Bauche *et al.*, Z. Phys. **A304**, 285 (1982)]. The result for the magnetic moment of the ground state of ^{131}La is +0.589(20) nm, and the quadrupole moment –0.66(11)b. Here, the errors arise from the propagation of errors in the A and B values and also include the uncertainties in the ^{139}La nuclear moments. We estimated the upper limit of the

hyperfine anomaly to be 0.5%, and due to this the magnetic moment was assigned an additional error.

In order to arrive at an understanding of the nuclear structure of ^{131}La, we performed a Nilsson model calculation with Coriolis coupling. The quadrupole deformation of ^{131}La has been theoretically predicted by Möller *et al.* [At. Data Nucl. Data Tables **59**, 185 (1995)] by using the finite-range droplet model. This deformation, $\beta = 0.19$, served as an input to the present Nilsson model calculation. A hexadecapole deformation was not included. The Nilsson potential parameters, $\kappa = 0.065$ and $\mu = 0.57$, were used according to Bengtsson and Ragnarsson [Nucl Phys. **A436**, 14 (1985)]. Pairing correlations are treated on the basis of the BCS theory. No attenuation of the Coriolis matrix element was applied. The effective single-particle gyromagnetic ratio g_s was set at 0.5 g_s (free), and a collective gyromagnetic ratio $g_R = Z/A$ was used.

From the spin-parity of 3/2+, the ground state of ^{131}La can be assigned as the Nilsson orbital [422]3/2. The calculated value for the magnetic moment is +1.00 nm, which is larger than the present experimental value. On the other hand, the quadrupole moment was calculated to be +0.61 b, showing a discrepancy in sign to the experimental result. These discrepancies could be attributed, at least partly, to the axially symmetric character of deformation in the FRDM and the Nilsson model. Further theoretical studies in which triaxial deformation is taken into consideration are needed to improve the predictions of the nuclear moments of ^{131}La.

Experiment 921

$K^\pi = 0^+$ 2.29 s isomer in neutron-rich ^{174}Tm

(R.S. Chakrawarthy, TRIUMF/SFU; P.M. Walker, U. Surrey)

Conversion-electron spectroscopy experiments, with a new Si(Li)-array, have been performed aiming to resolve an outstanding problem about the multipolarity of the two γ-ray transitions populated in the decay of the 2.29 s isomer in ^{174}Tm. The ground-state spin and parity of ^{174}Tm are known to be $I^\pi = 4^-$, as deduced from the ground-state systematics of the odd-proton Tm isotopes and the $N = 105$ isotones, and the allowed-unhindered β-decay proceeding to the lowest two excited 5^- states in ^{174}Yb [Kaffrell and Kurcewicz, Nucl. Phys. **A255**, 339 (1975)]. However, the excited states in ^{174}Tm populated in the $I^\pi = 0^+$ ground-state β-decay of ^{174}Er must be of low spin. Hence an unobserved low-energy, high-multipolarity transition was postulated, between the low-spin states observed following β decay and the high-spin ground state [Becker *et al.*, Nucl. Phys. **A522**, 557 (1991); Chasteler *et al.*, Z. Phys. **A332**, 239 (1989)]. However, several issues could not be resolved from γ-ray spectroscopy alone. These relate to the large intensity difference between the two, seemingly $M1$, γ-ray transitions at 100 and 152 keV; the absence of a 252 keV cross-over $E2$ transition; and speculation that the isomeric state could be a new excited state, the decay of which could not itself be established, requiring population from a hypothesized high-K β-decaying isomer in ^{174}Er [Chakrawarthy *et al.*, Eur. Phys. J. **A25**, s01, 125 (2005)].

A closer examination of the K-electron conversion coefficient for the 152 keV transition, extracted from X-ray and γ-ray intensities, reveals that it agrees, within error, with the values expected for an $M1$ multipolarity (α_K= 0.81) and an $E3$ multipolarity (α_K= 1.18). Furthermore, an $E3$ multipolarity for the 152 keV transition would explain the large intensity imbalance with the 100 keV transition that arises from the earlier deduction of $M1$ multipolarity for both transitions. However, the L-conversion coefficients would differ greatly (α_L= 0.12 and 4.1 for $M1$ and $E3$ multipolarity, respectively), motivating a measurement involving a conversion-electron spectrometer. Therefore, in a follow-up experiment, a new conversion-electron spectrometer, pentagonal array for conversion electron spectroscopy (PACES), was brought on-line at the 8π-spectrometer station. PACES is composed of five (cooled) Si(Li) detectors, 5 mm thick, circular in shape, with an area of 200 mm^2, and mounted at a distance of 2.2 cm from the beam focus. About 8% of the solid angle was covered by PACES. In the "singles" conversion-electron spectrum (Fig. 86) and the spectrum gated by the 100 keV γ-ray transition (Fig. 87) the key feature is the prominent peak at 142 keV due to L-conversion, with the K- and M-conversion peaks being of relatively

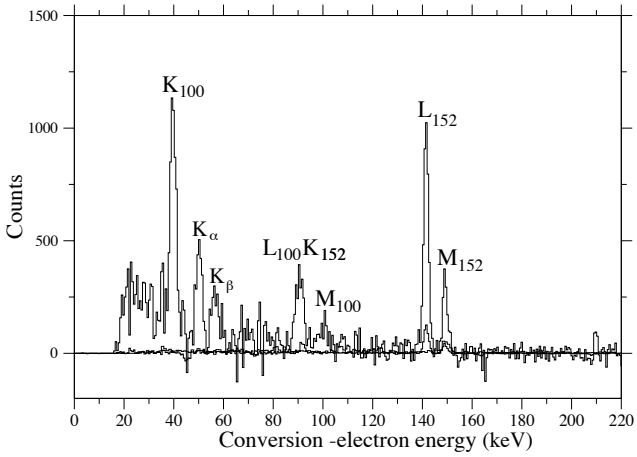

Fig. 86. The singles conversion-electron spectrum obtained by subtracting the 5.4 m ^{174}Tm ground-state β-decay component. K_γ denotes the conversion-electron corresponding to the γ-ray transition, while the Tm X-rays are labelled as K_α/K_β.

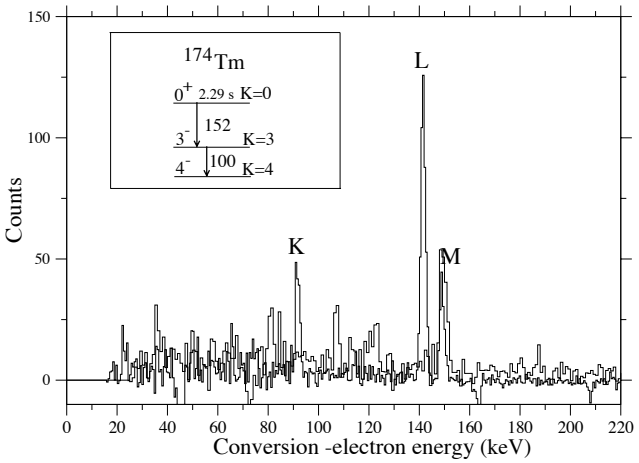

Fig. 87. The conversion-electron spectrum gated by the 100 keV γ-ray transition. The earlier [Becker *et al., op. cit.*], incorrect, $M1$-multipole assignment for the 152 keV transition would have given rise to strong K conversion and very little L and M conversion. The inset depicts the isomer decay-scheme as a result of the present work.

low intensity in this spectrum. The deduced conversion coefficients, as well as the K/L and L/M intensity ratios, compare very well with an $E3$ multipolarity assignment for the 152 keV transition, and rule out the $M1$ alternative. Similarly, the conversion electron data unambiguously assign $M1$ multipolarity to the 100 keV transition. The deduced conversion-electron coefficients are presented in Table X.

In view of the lack of a cross-over γ-ray transition (I_γ 252 keV $\leq$ 0.34% I_γ 100 keV) or a highly-converted $M4$ transition, in the "singles" conversion-electron spectrum (Fig. 86), it is inferred that the 100 and 152 keV transitions are of stretched $M1$ and $E3$ character, respectively. A 100 keV $M1$ transition would not give rise to such a long half-life, so the 152–100 keV transition ordering is well-defined. Accordingly, the spin-parity sequence is (in increasing energy order) either $4^- - 5^- - 8^+$ or $4^- - 3^- - 0^+$. Only the 0^+ assignment for the 252 keV isomer is consistent with the known indirect feeding from the β decay of ^{174}Er [Becker *et al., op. cit.*; Chasteler *et al., op. cit.*].

A direct ^{174}Er ($I^\pi = 0^+_{\rm g.s.}$)$\rightarrow$ ^{174}Tm($I^\pi = 0^+_{\rm isomer}$) Fermi-transition will be strongly suppressed due to the non-analogue nature of the orbitals involved, consistent with the observed intensity flow. The same selection rule also forbids β decay of the ^{174}Tm isomer to ^{174}Yb $K^\pi = 0^+$ levels. An upper limit of 1.0(5)% β decay branch could be deduced for such a forbidden decay. This limit was determined from the peak-free region of the electron spectrum from the 2 s/3 s/3 s tape cycle after background subtraction from the e^--time data.

Table X. Experimental and theoretical internal conversion coefficients (ICC).

Energy (keV)	ICC (expt.)	ICC (theory)
152.1	α_K 1.13 ± 0.06	$\alpha_K(E3)$ 1.18
	α_L 3.31 ± 0.48	$\alpha_L(E3)$ 4.10
	α_M 1.10 ± 0.12	$\alpha_M(E3)$ 0.99
100.3	α_K 3.10 ± 0.01	$\alpha_K(M1)$ 2.66
	α_L 0.45 ± 0.10	$\alpha_L(M1)$ 0.40
	α_M 0.14 ± 0.03	$\alpha_M(M1)$ 0.09

γ-ray and conversion-electron spectroscopy have thus established the existence of a 2.29(1) s, $K^\pi = 0^+$, isomeric state in neutron-rich ^{174}Tm. The isomer de-excites via 100 and 152 keV electromagnetic transitions. First results from a newly commissioned Si(Li) detector array have established their $M1$ and $E3$ multipolarities, respectively. The single-particle configurations of the excited states suggest that the $E3$ transition originates from a $\pi h^{-1}_{11/2} \rightarrow \pi d_{3/2}$ configuration change, while the $M1$ transition occurs between members of a Gallaghar-Moszkowski(GM) doublet. Calculations based on the quasi-particle phonon model (QPM) predict the two lowest-lying intrinsic states in ^{174}Tm to be the GM-doublets [Jain *et al.*, Rev. Mod. Phys. **70**, 843 (1998)], and the calculated splitting of 94 keV is very close to the observed splitting of 100 keV. From the measured half-life, the deduced $B(E3)$ value of 0.024(2) W.u. is highly hindered but is well within the prescribed range for a K-allowed $\Delta K = 3$, $E3$ decay. The reported measurements resolve ambiguities in the previously proposed β-decay scheme of ^{174}Er to ^{174}Tm. The results of three different experiments can be combined to explain all the data consistently with a minimum number of states [Becker *et al., op. cit.*; Chasteler *et al., op. cit.*; Chakrawarthy *et al., op. cit.*].

Experiment 921 is a collaboration of scientists from TRIUMF, Simon Fraser University, University of Surrey, Lawrence Livermore National Laboratory, Louisiana State University, Saint Mary's University, University of Guelph, GSI, Youngstown State University, and Georgia Institute of Technology.

Experiment 929
Radon EDM
(T.E. Chupp, Michigan; C.E. Svensson, Guelph)

Measurements of permanent electric dipole moments (EDMs) have an impact on both standard model physics (in the form of the vacuum expectation value of the gluon field, $\theta_{\rm QCD}$) and in physics beyond the standard model (e.g., defining the mass scale of the physics generating the baryon asymmetry and constraining the parameter spaces of supersymmetric theories). The enhanced sensitivity to EDMs, compared to that of ^{199}Hg (which is the basis of the most precise atomic EDM

measurement to date), of ^{223}Rn makes it a prime candidate for improving the limits on many fundamental parameters. Studies of various systems required for the experiment continue while we await the approval and installation of the actinide target at TRIUMF necessary for the production of ^{223}Rn.

Polarization of radon at Stony Brook

First run Work at Stony Brook continued in May with a run designed to collect and polarize ^{209}Rn. To produce the radon, a ∼91 MeV ^{16}O beam is focused onto a heated $^{197}_{79}$Au target, creating francium atoms that surface ionize and are accelerated to 5–8 keV and focused into a beam. This francium beam is steered to our zirconium foil and 11% of the implanted ^{209}Fr ($T_{1/2}$ = 50 s) decays to ^{209}Rn ($T_{1/2}$ = 23.8 min.). Implantation continues for about an hour, at which point the radon is transferred by freezing into the optical pumping cell utilizing techniques developed at TRIUMF [Nuss-Warren *et al.*, Nucl. Instrum. Methods **A533**, 275 (2003)]. The cell, approximately spherical and made of Pyrex coated with octadecyltrichlorosilane (OTS), had been pre-loaded with a small amount of rubidium before being attached to the vacuum system. After freezing the radon into the cell, ∼1 atm of N_2 buffer gas is added and we heat to temperatures appropriate for optical pumping (e.g. 130°C). Circularly polarized D1 light from a broadband laser diode array polarizes the rubidium and, through spin exchange collisions, the radon. Two HPGe detectors, placed at 0° and 90° with respect to the magnetic field $\vec{B}$ generated by Helmholtz coils centred on the cell, detect the γ-rays emitted when ^{209}Rn decays to excited states of ^{209}At. Some percentage of the alignment of the radon spins will be passed on to the excited ^{209}At after decay, leading to asymmetries in the angular distribution of γ-rays from these atoms and thus a measurable signal for the degree of alignment achieved.

Due to the low efficiency of the HPGe detectors used (∼20%), losses during the transfer of the francium beam from the gold target to our foil, upper limits on the temperature of the cell (a restriction caused by the presence of the OTS coating), and background issues, only for one of the four main γ-ray lines (see Fig. 88) were we able to see a statistically significant anisotropy between rates at 0° and 90°. The measurements are self-calibrating, with the signal being a difference between the ratios with the laser on and with it off, corresponding to polarized and unpolarized radon. The results for the 337 keV line are shown in Fig. 89.

Second run In December, the apparatus was moved to a different location at Stony Brook that allowed for better beam tuning and more efficient transfer of francium to our foil and two new HPGe detectors (of 30 and 50% efficiency) were used. Preliminary cell characterization studies and the literature on the subject [Wu *et al.*, Phys. Rev. **A42**, 2774 (1990)] indicated that uncoated cells would lessen the quadrupole relaxation experienced by the spin-5/2 ^{209}Rn atoms, motivating the use of a new set of uncoated optical pumping cells in this run. Measurements were taken at temperatures

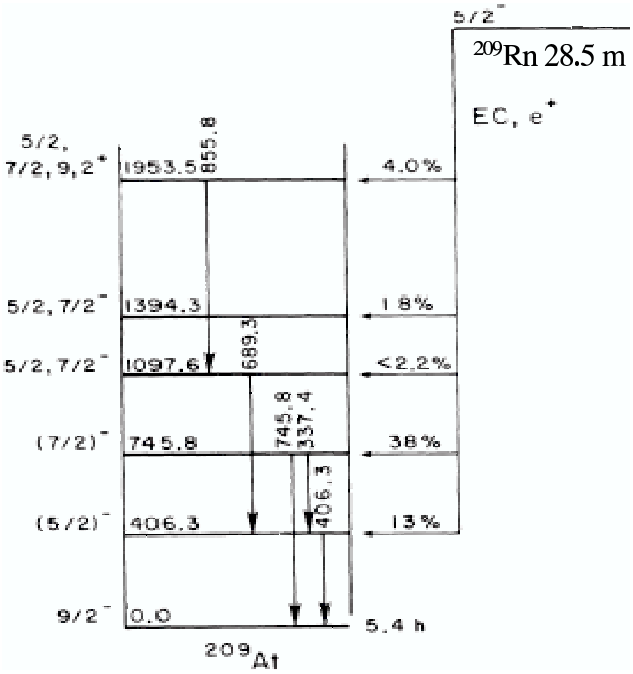

Fig. 88. The important lines in the ^{209}Rn decay scheme.

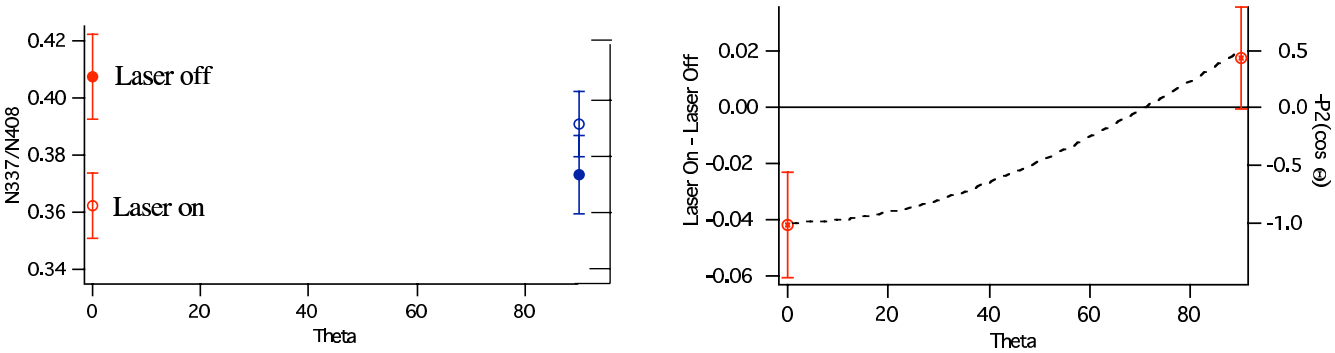

Fig. 89. The 337 keV γ-ray anisotropy from the first Stony Brook run, normalized to the isotropic 408 keV γ-ray. The right panel includes the expected $P_2(\cos\theta)$ dependence to help guide the eye.

Table XI. 0°/90° count ratios for the 337 keV line.

Cell temp. (°C)	Laser off	Laser on
150	2.256(83)	2.275(79)
170	1.906(91)	1.869(81)
180	2.019(68)	1.886(68)
190	2.045(60)	1.893(54)
200	2.297(73)	2.026(63)

Table XII. 0°/90° count ratios for the 745 keV line.

Cell temp. (°C)	Laser off	Laser on
150	4.164(205)	4.254(163)
170	3.894(182)	3.987(192)
180	3.988(135)	3.969(154)
190	4.015(111)	4.202(123)
200	4.001(126)	4.289(148)

ranging from 150°C to 200°C with the strongest signal coming from the highest temperature data (see Tables XI and XII for preliminary results). The geometry of the set-up limited the proximity to the cell of the 90° detector, offsetting some of the gains made in detector and radon transfer efficiency.

Optical pumping studies at University of Michigan

The new optical pumping cells used in the second Stony Brook run were made at Michigan and filled with rubidium, ∼100 torr natural xenon (26.4% ^{129}Xe, I=1/2 and 21.2% ^{131}Xe, I=3/2), and ∼1 atm N_2 in order to use them for studying the effect of quadrupole relaxation and, later, as a diagnostic tool for the Stony Brook set-up. Using adiabatic fast passage (AFP) NMR, we worked towards determining the relaxation rates of ^{131}Xe as compared to those of the ^{129}Xe in the same cell, thus acquiring information on the contribution of the quadrupole wall interaction to the achievable polarization of $I > 1/2$ noble gases. Figure 90 shows an example spectrum.

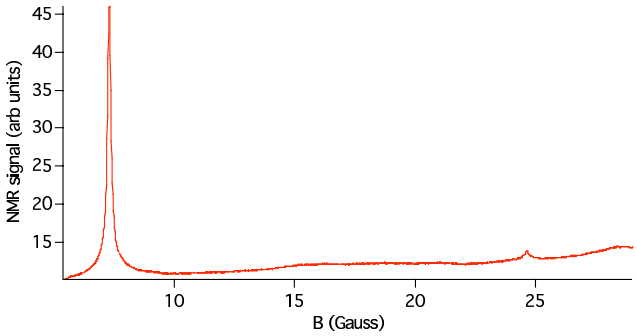

Fig. 90. An AFP NMR spectrum. The ^{129}Xe peak is to the left, and ^{131}Xe is to the right. The relative sizes are due to differences in the NMR parameters (magnetic moment, etc.), spin-exchange rates, and relaxation mechanisms.

^{120}Xe half-life measurement

The data collected in the 2003 TRIUMF run establishing the collection and transfer techniques [Nuss-Warren *et al., op. cit.*] were used to extract a measurement of the half-life of ^{120}Xe that was significantly different than the tabulated value of 40 ± 1 min., and a paper reporting our result is in preparation.

Experiment 930
Search for free decay of negative pions in water and light material
(T. Numao, TRIUMF; Y. Efremenko, Tennessee)

Flavour asymmetry in the incident neutrino beam is one of the key elements for successful neutrino oscillation experiments. In the case of beam-dump experiments using muon decays from stopped pions, negative pions are believed to be captured promptly after stopping in material, while positive pions freely decay. The total neutrino content after the pion decay $\pi^+ \to \mu^+\nu_\mu$ followed by the muon decay $\mu^+ \to e^+\nu_e\bar{\nu}_\mu$ ($\pi^+ \to \mu^+ \to e^+$ decay) does not include $\bar{\nu}_e$'s in the final state (the contribution from decay-in-flight is about 10^{-3} for a pion). This provides a good opportunity for $\bar{\nu}_e$ appearance experiments. However, if a π^- has non-zero lifetime in the stopping material, it may cause a significant contamination of $\bar{\nu}_e$'s. No limits for the fraction of the free-decay component exist in the stopping material except in liquid H_2, He and Ne. It is therefore important to confirm the absence of mechanisms that may cause free decays of π^-'s.

A direct method to search for free π^- decay is to detect electrons from the decay $\pi^- \to e^-\nu$. Because of its small branching ratio, 1.231×10^{-4}, it is very difficult to differentiate it from the background arising from prompt nuclear capture γ-rays that convert in the target to electron-positron pairs; the search for $\pi^- \to e^-\bar{\nu}$ was effective for a component with a relatively long lifetime. The presence of delayed electrons from the $\pi^- \to \mu^- \to e^-$ decay chain ($E_e = 0$–53 MeV) is also a signature of free pion decays; the background from decay-in-flight (DIF) of a pion to a muon, which stops in materials around the target and later decays to an electron, needs to be subtracted. One advantage of this method is that the sensitivity varies only by ∼15% for the lifetime between 0 ns and τ_π (26.033 ns). Another signature of free pion decay is the presence of delayed components in the time spectrum of pion capture products, such as protons. However, the capture experiment is insensitive to the free decay component as the lifetime approaches the pion lifetime.

The experiment was carried out at the TRIUMF M9 channel. Figure 91 shows the detector set-up. The incoming pion beam at $P_\pi = 70$ MeV/c was measured by two wire chambers (WC1 and WC2), identified by

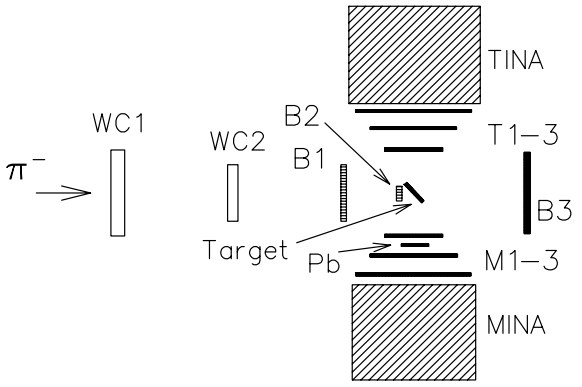

Fig. 91. Experimental set-up.

two plastic scintillators, B1 and B2, and stopped in a $60 \times 60 \times 8$ mm^3 water target at a rate of 1–10 kHz for the π^- beam and 30–100 kHz for π^+. We also used beryllium, aluminum and vinegar as target. The decay products were observed by two telescope arms at $\pm 90°$; each telescope consisted of three 3–6 mm thick plastic scintillators (T1–T3 or M1–M3), and a 46 cm diameter, 51 cm long NaI(Tl) crystal (TINA) or a 36 cm diameter, 36 cm long NaI(Tl) (MINA). For π^0 detection, a 5 mm thick 50×50 mm^2 lead sheet was placed as a converter between M1 and M2 in the MINA telescope.

In the analysis of $\pi^- \to \mu^- \to e^-$ decay events, electrons were selected based on the energy losses in the T1–T3 counters. Only delayed events (t_e = 48–81 ns) were selected for the analysis. The yield was normalized to that of the $\pi^+ \to \mu^+ \to e^+$ decays. The contribution of DIF events was simulated and subtracted from the data. 90% C.L. upper limits for the free-decay fraction in water were obtained to be 7.5×10^{-4} for a short lifetime and 7.9×10^{-4} for $\tau = \tau_\pi$.

Event selection criteria for the $\pi \to e\nu$ decay analysis were tighter than those used in the $\pi \to \mu \to e$ analysis because of its small branching ratio and sensitivity to background. Some events were seen in the time-energy box with time distribution consistent with the electron scattering background, though they were included in the free-decay candidates.

In the search for free π^- decay via detection of delayed protons from π^- capture, the time spectrum of protons essentially had a single component, a Gaussian peak at t_0. There were a few counts after t_0, which were treated as signal. A potential delayed component was extracted by fitting the time spectrum; the fit function was a Gaussian plus an exponential function including the resolution effect.

In the long lifetime region, the fit results were affected by the small sample bias. A simple time bin method was employed for this region; events in the time bin of t_p = 5–75 ns were considered to be possible candidates, and the sum in the time bin was normalized to the total number of events in the proton spectrum.

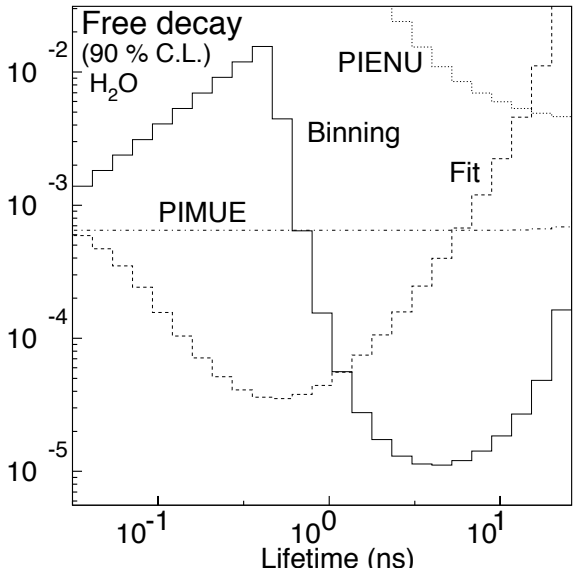

Fig. 92. Free decay fractions in H_2O. The dashed histogram is the result by fit, the solid histogram by binning, the dotted histogram by $\pi \to e\nu$ and the dash-dotted line by $\pi \to \mu \to e$.

All results from the $\pi \to \mu \to e$, $\pi \to e\nu$ and capture analyses are shown in Fig. 92. The limits obtained by the capture measurements became unity at $\tau = \tau_\pi$ (the next bin outside Fig. 92). Without knowing the lifetime of the delayed component, the conservative limits obtained at the pion lifetime for all materials are: 7.9×10^{-4} for H_2O by the $\pi \to \mu \to e$ analysis, 3.1×10^{-3} for beryllium, 7.6×10^{-3} for aluminum and 3.9×10^{-3} for vinegar by $\pi \to e\nu$.

The π^- capture ratio by hydrogen and oxygen atoms in water was measured using the reaction $\pi^-\mathrm{H} \to \pi^0 n$ for capture in hydrogen. Using the Panofsky ratio to compensate for the $\pi^-\mathrm{H} \to \gamma n$ channel, the capture ratio by the hydrogen atom in water was obtained to be $0.458 \pm 0.010(\mathrm{stat}) \pm 0.027(\mathrm{syst})\%$. An alternative method was to fit, to the expected energy spectra of hydrogen and oxygen capture, the singles γ-ray energy spectrum measured by MINA. The capture ratio in hydrogen was obtained to be $0.560 \pm 0.016 \pm 0.062\%$. The combined result of the two methods was $0.475 \pm 0.026\%$.

Experiment 948/986/1021
Proton and neutron radiation effects in silicon-on-insulator and bulk-silicon devices

(J.R. Schwank, Sandia National Lab)

Introduction

The primary goal of these experiments was to investigate proton radiation-induced effects on silicon-on-insulator and bulk-silicon devices for space applications. The proton energy range available at TRIUMF

(∼20 to 500 MeV) is well matched to the energy spectrum of protons in space. The experiments were divided into three main tasks: 1) investigation of the energy dependence for single-event latchup (SEL) and its impact on hardness assurance qualification, 2) investigation of total ionizing dose on the single-event upset hardness of advanced ICs, and 3) investigation of the sensitivity of SRAMs to neutrons; comparison of experiments to Monte Carlo simulations.

Work was also planned with the intent to investigate the charging effects in microelectrical mechanical systems (MEMS). MEMS offer numerous advantages for space environments. Works by us and others have shown that MEMS devices can degrade in charged particle environments (e.g., protons and electrons), but are relatively insensitive to total dose ionizing radiation effects (e.g., X-rays and γs). We planned to investigate the role of "charged" particle irradiations in 2005 to understand the mechanisms for the proton and electron induced degradation. Unfortunately, the variability in the pre-irradiation characteristics of the devices was too large to accurately assess the effects of charged particle irradiation.

Single-event effects

One of the most detrimental effects of the natural space environment on electronics is single-event effects (SEE). In memory circuits, information is stored at nodes in a circuit. If a high-energy heavy ion strikes a circuit node, it can create sufficient charge in a transistor to change the state of the node and cause false information to be stored. This type of failure is a non-destructive soft error and is known as a single-event upset (SEU). In addition to heavy ions, protons and neutrons can also cause single-event upset. An SEU can be corrected by reprogramming the circuit into its correct logic state or by restarting an algorithm in a central processing unit. The number of soft errors is normally specified in units of errors/bit-day. If the error rate is too large, it can result in performance degradation of a system and potentially mission failure.

A class of single-event effect that is not correctable by reprogramming is termed a hard error. Hard errors include single-event latchup (SEL), snapback (also called single transistor latch), burnout (SEB), and gate rupture (SEGR). If a hard error occurs, a circuit element can be physically damaged and the error cannot be corrected by reprogramming.

As IC technology advances, power supply voltage are reduced, circuit dimensions are decreased, less charge is stored on circuit nodes, and the energy required to change the state of a circuit node decreases. Hence, these devices are becoming more vulnerable to SEE. In fact, not only are commercial silicon circuits sensitive to radiation in the space environment, but they also are becoming more prone to upset due to cosmic-ray by-products (e.g., neutrons) and radioactive package contamination at the ground level and in aircraft. Soft errors due to terrestrial radiation are becoming a major reliability concern for commercial IC manufacturers.

This year at TRIUMF, we performed several experiments investigating proton and neutron induced SEE in silicon-on-insulator and bulk-silicon ICs. For each task, in addition to the experiments performed at TRIUMF, other experiments were performed to obtain a more comprehensive understanding of the effects of radiation on SEE.

Energy dependence for single-event latchup

Introduction Energetic particles in space can degrade integrated circuit (IC) performance and potentially cause IC failure in space systems through several single-event effect mechanisms. One of the most problematic single-event effects is single-event latchup (SEL). When a latchup occurs, the latchup state can be cleared only by removing power from the device. SEL can also lead to destructive IC failure. As a result, many space systems cannot tolerate even a single SEL. To ensure part functionality and possibly system survivability, it is critical that hardness assurance tests for SEL be capable of accurately determining IC susceptibility to single-event latchup.

Both protons and heavy ions can cause SEL in electronics in satellite systems. For some applications, electronics can be exposed to high fluxes of protons and the number of SEL events is dominated by proton strikes. To minimize test costs, devices are often screened for single-event hardness assurance using heavy ion tests. If the LET threshold for SEL determined by heavy-ion tests is sufficiently high, proton testing is often not performed. What LET threshold constitutes sufficiently high is not well defined. In the past, a frequently used guideline is the maximum LET of nuclear recoils that can be produced by energetic proton interactions with silicon (∼13 MeV cm^2/mg). As long as the LET threshold is above this value, proton testing may be postponed or cancelled. The validity of this assumption has not been fully investigated, especially for today's high-density ICs. To develop accurate hardness assurance SEL test guidelines, the correlation between heavy-ion and proton-induced SEL must be better understood.

It was recently shown that SEL testing at facilities with low maximum proton energies (<100 MeV) can significantly underestimate the probability for latchup and falsely lead to the conclusion that SEL-sensitive devices are latchup-free. This preliminary work examined only a limited number of devices and all testing was performed at room temperature. However, it is

well known that susceptibility to SEL can be greater at elevated temperatures. As a result, the effects of proton energy on SEL hardness need to be evaluated at elevated temperatures. To develop reliable hardness assurance tests for space environments, it is essential that we fully understand the mechanisms for the effects of proton energy on SEL hardness.

In this work, we examine issues relevant to proton SEL hardness assurance testing of ICs. SRAMs from several different suppliers are irradiated at room and elevated temperature at proton energies from 20 to 500 MeV over a wide range of fluence levels. To help identify the mechanisms for the degradation in SEL hardness with proton energy, the latchup cross section versus linear energy transfer (LET) was also characterized with heavy ions using a broadbeam heavy-ion source for some devices. The effective LETs of energetic nuclear recoils induced by high-energy proton collisions were calculated for a variety of materials common to present-day IC technologies using a modified version of the High-Energy Transport Code (HETC). These calculations are compared to the experimental results to elucidate the mechanisms for proton induced SEL in present-day ICs. Our data show a much larger variation in SEL cross section and proton energy threshold than previously observed. Nuclear scattering cross section calculations suggest that materials common to present-day SRAMs can make devices more prone to proton-induced SEL. These results have significant implications for proton hardness assurance testing for space environments.

Experimental details Proton irradiations were performed at the TRIUMF Proton Irradiation Facility. The proton energy was varied from 20 to 500 MeV. Energies from >70 to 105 MeV and <70 MeV were obtained by degrading 116 MeV and 70 MeV primary beams, respectively, using a variable thickness plastic plate. Protons with energies above 105 MeV were obtained by varying the primary beam energy of a second beam line capable of a maximum proton energy of 500 MeV. The proton fluence was measured using a calibrated ion chamber.

For latchup characterizations, SRAMs were irradiated in their preferred power-up logic state, i.e., they were not written with a specific pattern prior to exposure. The power supply current was continuously monitored during irradiation. When the power supply current increased to above a preset limit, a latchup was recorded, the power supply voltage was removed to clear the latchup state, the power supply voltage was reapplied, and the latchup test was continued. The preset limit was set to a current a few milliamps above the static current for the device. The latchup current was limited to 100 mA to minimize potentially destructive latchup effects. To clear latchup, the bias to the device was turned off for 0.5 s after a latchup was detected and then the bias was reapplied. For a given particle flux, this limits the maximum latchup rate that can be accurately measured. Because some SRAMs were exposed to high fluence levels and were repeatedly put into a latched state, the SEL cross sections of SRAMs were measured before and after repeated SEL characterizations. Within experimental uncertainty, the same SEL cross sections were measured before and after repeated characterization, suggesting that proton-induced displacement damage and total ionizing dose effects were negligible, and that there were no latent effects caused by repeated latchup testing.

Table XIII lists the devices used and shows the memory size of the SRAM, cell design if known (four or six transistors), technology feature size, and the tested bias voltage. All SEL characterizations were performed under worst-case biasing conditions, i.e., maximum bias voltage. Note that vendor C SRAMs operate using dual external supply voltages, e.g., 3.3 V and 2.0 V.

Proton-induced latchup – energy and temperature dependence Based on room temperature measurements of the SEL cross section versus proton energy, it has been shown that low-energy proton (<100 MeV) measurements can significantly underestimate the SEL cross section and may lead to the false conclusion that SEL-sensitive SRAMs are latchup-free. We first explore the effects of temperature on present-day ICs from two different technologies with soft to moderate proton-induced SEL hardness. Figures 93 and 94 are plots of the latchup cross section for SRAMs from vendors B and C, respectively, measured at 25°C (room temperature) and at 85°C. Vendor B SRAMs have a very high SEL saturation cross section with a low proton energy latchup threshold (soft), while vendor C SRAMs have a much lower SEL saturation cross section (moderately hard). For both SRAMs, temperature does not appear to have a large effect on the proton latchup threshold energy (the lowest energy where latchup was detected). The measured thresholds are approximately 20 and 35 MeV for vendor B and C SRAMs, respectively, at

Table XIII. Devices used in tests.

Vendor	Size (Mbits)	Cell design	Feature size (μm)	Bias voltage
A	4	6T	0.25	3.6
B	4	4T	0.18	5.5
C	1	6T	0.16/0.14	3.3/2.0
D	4	Unknown	Unknown	5.5
E	4	Unknown	Unknown	3.6
G	4	4T	0.18	3.6

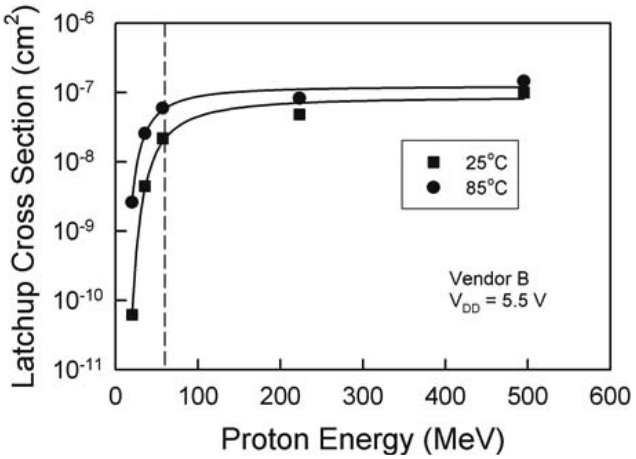

Fig. 93. Latchup cross section versus proton energy for SRAMs from vendor B measured at room temperature and at 85°C.

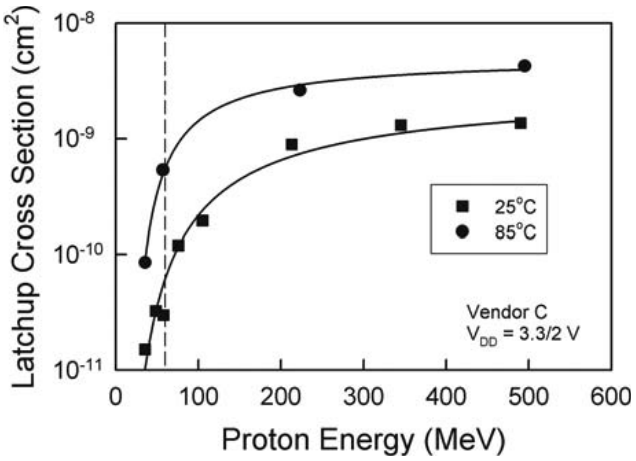

Fig. 94. Latchup cross section versus proton energy for SRAMs from vendor C measured at room temperature and at 85°C.

both 25°C and 85°C. Within experimental uncertainty, the saturation (highest energy) cross section measured at 25°C and 85°C are equal for vendor B SRAMs. At lower energies, the cross section varied more with measurement temperature. For measurements taken at 85°C, the SEL cross section is roughly the same for all energies above ∼60 MeV (noted by the dashed line in the figure). Hence, as long as the proton energy is above ∼60 MeV, proton energy and temperature have little effect on the measured probability for latchup for these SRAMs. For vendor C SRAMs, the SEL cross section is much higher at 85°C than at 25°C. However, at 25°C the cross section at an energy of 500 MeV is 40 times more than it is at 60 MeV, while at 85°C the cross section at an energy of 500 MeV is only about seven times more than it is at 60 MeV. Thus, for vendor C SRAMs proton energy still has some effect on SEL cross section when measured at elevated temperature, but this effect is much less than at room temperature.

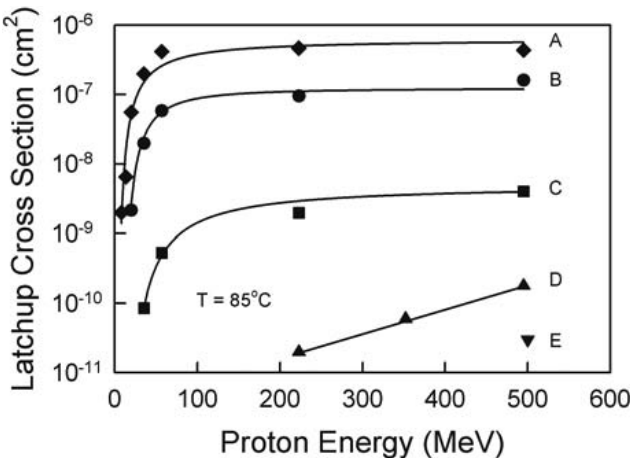

Fig. 95. Latchup cross section versus proton energy for four different technologies. SEL measurements were taken at a temperature of 85°C.

The above results show examples of soft and moderately SEL-hard technologies where the requirement for testing at very high proton energies is lessened when measured at elevated temperature. However, this is not always the case. Figure 95 is a plot of the SEL cross section for vendor A, D, and E SRAMs measured at 85°C. For comparison, the SEL cross sections for vendor B and C SRAMs are also plotted. Similar to vendor B SRAMs, vendor A SRAMs have a high SEL cross section and low threshold energy and there is almost no difference in the measured cross section for proton energies greater than ∼60 MeV. Vendor D and E SRAMs are much harder than vendor A, B, or C SRAMs. In fact, no latchups were detected at 25°C for vendor D and E SRAMs for any proton energy. At 85°C, the lowest energy at which latchups were detected for vendor D SRAMs was 223 MeV, while for vendor E SRAMs, latchups were only detected at 490 MeV, the highest energy examined. In addition to a significantly higher proton energy threshold for latchup for vendor D and E SRAMs, the latchup cross sections were very low. Unlike the results of Figs. 93 and 94 for vendor B and C SRAMs, proton energy has a substantial effect on the probability for detecting latchup at elevated temperature. These results clearly show the importance of testing using a high-energy proton source. Even testing at a facility with a maximum energy of 200 MeV would probably have falsely concluded that vendor D and E SRAMs were latchup-free. The above results show that the worst-case temperature for SEL testing of present-day SRAMs is still maximum temperature. They also show that for systems where latchups cannot be tolerated, latchup testing should be performed using protons with energies at least equal to the maximum proton energy of the system environment. Because of practical issues regarding the availability of

high-energy proton sources, it is imperative to investigate alternative hardness assurance test methodologies, as discussed below.

The maximum trapped proton energy in the Earth's radiation belts is around 400 MeV. Because of the very high proton-energy threshold measured for vendor E SRAMs, we would not expect trapped protons to cause latchup in these SRAMs. However, it is possible that the energy dependence for latchup in vendor E SRAMs is similar to the energy dependence of vendor D SRAMs, but with a lower cross section. If vendor E SRAMs were irradiated to higher fluence levels than in Fig. 95, it is conceivable that latchups could be detected at lower proton energies (e.g., those present in the Earth's radiation belts). Although the proton fluence levels required to observe latchup would be much higher than obtainable in most systems, if many of these SRAMs were used in a system, in aggregate, the total cross section would be much higher and could result in realistic latchup probabilities for some space environments. Conclusively excluding the possibility of latchup in such systems would require irradiating SRAMs to still higher fluence levels, probably necessitating the characterization of many SRAMs to avoid total dose damage of individual SRAMs. However, if we could gain a better understanding of the mechanisms causing the differences in cross section with energy for the different SRAMs, it might be possible to develop more reliable (and more practical) hardness assurance test guidelines for SEL.

To obtain insight into the mechanisms for the differences in proton-induced SEL thresholds and cross sections for the different SRAMs shown in Fig. 95, we measured the heavy-ion induced SEL cross sections for some of these SRAMs and performed nuclear scattering cross section calculations for proton interactions with materials common in present-day IC technologies.

Hardness assurance implications System requirements often necessitate the characterization of both heavy-ion and proton SEL hardness. To save money, devices are frequently screened for single-event latchup first using heavy ions prior to proton testing. If devices are sufficiently insensitive to heavy ions, proton testing may not have to be performed. One question that is often asked is what minimum heavy-ion SEL threshold LET is required to ensure devices will not latchup in proton environments? A general rule-of-thumb that has often been used is that if the SEL threshold LET is above $\sim$15 MeV cm^2/mg, then devices will not latchup in proton environments. This is based on the fact that the maximum LET for nuclear recoils generated by proton interactions with Si is $\sim$13 MeV cm^2/mg. If the measured heavy-ion SEL threshold is above this value, proton SEL testing could be delayed or cancelled. The results of this work suggest that this rule-of-thumb may not be appropriate for high-density ICs (e.g., SRAMs). The maximum LET for nuclear recoils generated by proton interactions with W is closer to 34 MeV cm^2/mg. In light of the fact that almost all high-density ICs incorporate W, a better rule-of-thumb for high-density ICs might be that if the SEL heavy-ion LET threshold is $\geq$40 MeV cm^2/mg the devices will not latchup in proton environments. For simpler devices which may not use high-Z materials, the old rule-of-thumb may still be valid.

Of course, our results also indicate that proton-induced latchups due to high-LET secondary particles are rare events (i.e., have low cross sections), and therefore proton SEL hardness assurance test decisions should be made bearing overall system reliability requirements in mind. Hardness assurance decisions should take into account issues such as the flux of high-energy protons in the system environment and the probability of SEL that can be tolerated. For instance, if SEL events are only detected at proton energies above that of the maximum proton energy of the environment, a maximum SEL rate can be determined at the maximum energy of the environment (assuming one latchup). If this SEL rate is below the acceptable latchup rate no further testing would be warranted and the device can be considered to have passed SEL test requirements. In some cases, the maximum proton energy of the environment is above the maximum proton energy of readily available proton radiation sources. For example, the maximum proton energy of a proton radiation source could be 200 MeV, while the maximum proton energy of the environment could be 400 MeV. Even in this case, testing at 200 MeV could result in satisfactory estimates of SEL hardness in the environment. If no SEL events are detected at a proton energy of 200 MeV, one can determine a maximum SEL rate for proton energies up to 200 MeV by assuming one latchup at the maximum test fluence. For proton energies from 200 to 400 MeV, one could assume one latchup for every 10^4 protons/cm^2 and calculate a maximum SEL rate. (Based on a reasonable upper reaction rate for protons with standard IC materials.) If the number of protons in the environment with energies above 200 MeV is very small, this can still result in a very low SEL rate. If the combined SEL rate at 200 MeV and at energies between 200 and 400 MeV is below the acceptable latchup rate no further testing would be warranted and the device can be considered to have passed SEL test requirements.

Our results strongly suggest that proton SEL hardness assurance testing should be performed at the maximum proton energy of the system environment and maximum use temperature. For trapped protons in the

Earth's radiation belts, the maximum proton energy is around 400 MeV. For other environments and other applications, the maximum proton energy could be even higher. For example, protons with much higher energies can be generated in high-energy colliders. This poses a serious hardness assurance problem because there are few proton facilities worldwide that can produce very high proton energies (i.e., 500 MeV). A second problem in hardness assurance testing is that the cross section of high-Z materials is small compared to that for Si. Because of the small cross section for even high-energy protons to create secondary particles with high LET it is possible that a part may not latchup at proton energies of 500 MeV during testing. Whether the upper bound on proton SEL rate that can be established is low enough for a given application will of course be system-dependent. Therefore, the best procedure to ensure devices are truly SEL-free may be to test them using broad beam heavy ion sources, where high-LET ions can be produced directly. For devices that show heavy ion SEL threshold LETs between 10 and 40 MeV cm^2/mg, further comprehensive testing in a high-energy proton environment may be necessary to determine the true proton-induced SEL sensitivity.

Summary We have found that the proton-energy threshold for SEL and the maximum SEL cross section can vary significantly between device technologies. In general, increasing the SEL characterization temperature increased the proton-induced SEL cross section. However, for some SRAMs, characterizing SEL hardness at elevated temperature decreased the difference in SEL cross section when measured at low and high proton energies. For other SRAMs, latchup was only detected at elevated temperature and at very high proton energies (>200 MeV). For one SRAM, latchups were only detected at a proton energy of 490 MeV. These results show that ideally proton-induced SEL hardness assurance testing should be performed at the maximum temperature and the maximum proton energy of the system environment. Combining measurements of the heavy-ion SEL threshold LET with proton nuclear scattering calculations, we determined that the cause of high proton energy SEL thresholds for some SRAMs was likely the generation of nuclear recoils with LETs up to 34 MeV cm^2/mg by high-energy proton interactions with W. Tungsten is common to many present-day high-density ICs. These results suggest that the high-Z materials used in present-day high-density ICs may make them more sensitive to proton-induced latchup than older technologies. Because of the potentially low cross section of W and other high-Z materials in high-density ICs (compared to Si), the SEL cross section for high-density ICs can be very low, making hardness assurance for proton-induced latchup in such devices difficult. Thus, the optimum procedure to ensure devices are truly SEL-free in proton environments may be to test them using heavy ions with LETs $\geq$40 MeV cm^2/mg.

Effects of total dose on single-event upset

Introduction The single-event upset hardness of integrated circuits (ICs) in space environments can deteriorate as devices are exposed to proton or electron total-dose ionizing radiation. Work performed on older technologies exploring the combined effects of total dose and single event effects showed that exposing devices to ionizing radiation can degrade the proton and heavy-ion single-event upset (SEU) hardness. The increase in SEU sensitivity with total dose for these technologies was attributed to large threshold voltage cell imbalances. For these older technologies with relatively thick gate oxides, ionizing radiation induces imbalances in the threshold voltages of the transistors within the memory cell. The magnitude of the radiation-induced threshold voltage shifts can be considerably different for ON and OFF biased transistors, leading to large imbalances in the threshold voltages. More recently it was shown that exposure to ionizing radiation can significantly increase the single-event upset cross section of present-day technologies. Because of the extremely small radiation-induced threshold voltage shifts of thin gate oxide present-day technologies, this result was unexpected. It was speculated in that the cause of the decrease in SEU hardness with total dose for these present-day technologies was radiation-induced increases in field oxide leakage currents in peripheral circuitry, which lowered the output voltage of internal circuitry used to control the bias levels to the internal memory circuits.

In this work, we explore the mechanisms and properties for the effects of total dose on SEU hardness. Radiation-induced field oxide leakage current depends on several parameters, including temperature and the bias conditions during irradiation and measurement. To explore these effects, SRAMs from six different vendors were irradiated with protons at energies from 20 to 500 MeV, ^{60}Co γ-rays, or low-energy X-rays to varying total dose levels. Following total dose irradiation, the proton-induced SEU cross section was measured at 25 and 80°C and with different bias configurations. In some cases, the heavy-ion induced cross section was also measured. In addition, selective areas of the devices were irradiated with low-energy X-rays and SEU characterized. These results shed new insight into the mechanisms for total dose effects on SEU hardness. Space does not permit a full presentation of the test results.

Hardness assurance implications Our results imply that worst-case test conditions for SEU hardness assurance testing are maximum system total dose, maximum system operating temperature, and minimum operating bias supply voltage. The first two of these worst-case test conditions result from the effects of total dose on SEU hardness. Testing every SRAM at the maximum system total dose level and maximum system operating temperature can greatly increase the cost of hardness assurance testing. Hence, it is desirable to develop effective screens to determine whether or not an SRAM's SEU hardness will be impacted by total dose. For every SRAM that we examined that showed a total dose effect on SEU hardness, the SEU cross section varied with V_{DD} prior to total dose irradiation. The variation in SEU hardness with V_{DD} is a strong indication that these SRAMs use bias level shift circuitry to control the internal biases to the memory arrays. These results suggest a possible screen to determine whether or not an SRAM will show a total dose effect on SEU hardness. For example, one could measure the SEU cross section at three different values of V_{DD} (e.g., for vendor A SRAMs 3.0, 3.3, and 3.6 V). These measurements could be performed with either protons or heavy ions. If there is no difference in SEU cross section versus V_{DD}, total dose probably will not affect SEU hardness and characterizing SEU hardness at maximum system total dose levels and operating temperature is not necessary. However, if the SEU cross section varies with V_{DD} then one should characterize SEU hardness at maximum system total dose and operating temperature. One word of caution: This voltage screen is valid for all devices examined in this work. Whether or not this voltage screen can be universally applied to all SRAMs and probably more importantly to other types of circuits is not known and further work is required to ascertain the general applicability of this voltage screen.

Summary The SEU hardness of SRAMs has been investigated at elevated temperatures and over a wide range of bias supply voltages. For the devices investigated in this work, results show that worst case conditions are high total dose, elevated temperatures, and minimum bias supply voltage. The bias configuration during total dose irradiation and measurement greatly impacts the effect of total dose on SEU hardness. These results have significant impact on hardness assurance testing for space environments.

Neutron-induced SEU in bulk SRAMs: Monte Carlo simulations including neutron-silicon and neutron-oxygen interactions

Introduction Neutron-induced soft errors are now identified as a major reliability issue for complex electronic systems. The interactions of neutrons with nuclei in the device create secondary ions, which may be highly ionizing and can easily induce single event upsets (SEU) in integrated circuits. This effect has been evidenced at avionic altitude and ground level a long time ago. Several research teams have used nuclear codes (GEANT4) or developed dedicated tools (BGR methods, SEMM, DASIE) to predict and to understand the mechanisms responsible for the soft error rate (SER). A collaborative effort between CEA-EADS-CEM2 has developed a new SER simulator called MC-DASIE.

Recent studies at 14 MeV or between 1 MeV and 150 MeV have shown that interaction modelling should consider both neutron-silicon (n-Si) and neutron-oxygen (n-O) reactions to accurately calculate secondary ions produced in Si substrate and in SiO2 passivation layers. This task discusses the impact of neutron-oxygen interactions on the calculation of SEU sensitivity for bulk SRAMs induced by neutrons at energies from 14 MeV to 500 MeV. For the first time, Monte Carlo simulations with both n-Si and n-O interactions are done with charge diffusion modelling and a dynamic SEU criterion. A new neutron-oxygen interaction database has been developed and the MC-DASIE code has been upgraded to integrate these new interactions. In the first part, some experimental mono-energetic SEU cross section measurements are presented. In a second part, the basic principles of the MC-DASIE simulator are described for both nuclear and electrical modelling. Finally, we compare the simulation results with experimental data for all considered energies. The contribution of n-Si and n-O interactions are extracted from simulations to quantify the impact of materials on SEU mechanisms. The resulting sensitive volume and the contribution of each type of secondary ion are detailed for each simulated energy.

Experiments In this study, we investigated the response of a commercial 0.25 μm bulk SRAM. An SEU cross section characterization as a function of neutron or proton energy has been done. 14 MeV neutron measurements were performed at CEA Valduc (France) using the SAMES facility. The 50, 100, 200, 350 and 500 MeV SEU cross section characterizations were done at the TRIUMF proton irradiation facility (PIF). All tests were done at nominal supply voltage. For each test, the total dose did not exceed a few krad (Si) and the failure rate was the same between the first and the last irradiation run, so we ensure that the cumulated dose on devices does not modify the SER. Assuming the effects of protons and neutrons are similar for energies above 50 MeV, we have used proton beams instead of neutrons as mentioned in JEDEC test procedures.

Monte Carlo DASIE The Monte Carlo DASIE (MC-DASIE) code, which was especially developed for SER evaluation, has been used and upgraded. A Monte Carlo method is used to study the statistics of the SEU induced by secondary ions produced by neutron-nucleus interactions. This method is based on the use of a dedicated nuclear interaction database and an electrical modelling for SEU criteria.

Summary This study has shown that realistic neutron-induced SEU cross sections can be calculated with a limited set of technological parameters. Adding the neutron-oxygen interaction in the nuclear modelling gives interesting results concerning the relative contribution of each type of secondary particles. At low energy (14 MeV), O, N and C recoils are taken into account only when the n-O interaction is considered. This leads to the understanding of the significant role played by the passivation layer. For energies above 200 MeV, various types of secondary ions (from Si to He) induce SEUs. In this case, n-O reactions give secondary ion types, which are also produced by n-Si. This leads to the limited influence of oxygen atoms in SEU mechanisms.

Experiment 955
β-decay of ^{32}Na at ISAC/TRIUMF

(C. Mattoon, F. Sarazin, Colorado School of Mines)

Studies on neutron-rich nuclei near the N = 20 shell closure bring up challenges for the nuclear shell model. In particular, experimental studies have shown a breaking of magicity of the N = 20 [Motobayashi *et al.*, Phys. Lett. **B346**, 9 (1995); Azaiez *et al.*, Eur. Phys. J. **A15**, 93 (2002)] and the N = 28 [Sarazin *et al.*, Phys. Rev. Lett. **84**, 5062 (2000); Sohler *et al.*, Phys. Rev. **C66**, 054302 (2002)] configurations for neutron-rich nuclei. Key nuclei in their relevant regions such as ^{32}Mg and ^{44}S display large quadrupole collectivity arising from their prolate deformation. Early on, it was suggested that the emerging experimental results could partly be explained by adding more contributing orbitals to the valence space considered [Storm *et al.*, J. Phys. **G9**, L165 (1983); Poves, Phys. Lett. **B184**, 311 (1987)]. Over the years (and with the steady increase of computing power), shell model calculations in particular have led to a better understanding of the magicity disappearance in certain regions of the nuclear chart (for a recent review see Caurier *et al.* [Rev. Mod. Phys. **77**, 427 (2005)] and references therein). In the case of the N = 20 shell closure, the so-called "island of inversion" around ^{32}Mg is due to low energy fp-intruder states competing with the standard sd-orbitals, giving rise to the deformed configurations. The expected original spherical configuration is, however, believed to remain present at low-excitation energy, as recently demonstrated by the observation of a second 0^+ state in ^{44}S, which lies only 1365 keV above the ground-state [Grévy *et al.*, Eur. Phys. J. **A25**, 111 (2005)]. A similar shape coexistence is expected in ^{32}Mg, although so far, no indication of a low lying second 0^+ state has been observed.

Despite many experimental studies, significant features of the ^{32}Mg level scheme are still missing. In fact, only the first excited state at 885 keV was firmly assigned as a 2^+ state [Detraz *et al.*, Phys. Rev. **C19**, 164 (1979)]. The other excited states have at best received only a tentative assignment. Of interest are the locations of the 4^+ and 0_2^+ states to shed some light on the origin of the observed deformation. Azaiez *et al.* propose that the 4^+ state, identified in an in-beam γ spectroscopy experiment, is located at 2315(15) keV in agreement with the 2321 keV state previously observed by Klotz *et al.* in the β-decay study of ^{32}Na [Klotz *et al.*, Phys. Rev. **C47**, 2502 (1993)]. Recently, a highly selective two-proton knockout reaction on ^{34}Si brought new evidence of the existence of such a state in the vicinity of 2.31 MeV [Bazin *et al.*, Phys. Rev. Lett. **91**, 012501 (2003)]. However, conflicting evidence exists. With a tentative assignment of $(3^-,4^-)$ for ^{32}Na, a 4^+ state in ^{32}Mg could not be directly populated by the β-decay of ^{32}Na. Klotz *et al.* did not see any evidence that the 2321 keV state was populated from higher excited states. In hopes of resolving these contested assignments, another experiment was performed at ISAC.

The β-decay of ^{32}Na was investigated at TRIUMF-ISAC in late 2003 using the 8π/SCEPTAR β-decay station (see TRIUMF Annual Report 2003, p.77). ^{32}Na atoms were produced by bombarding a 22.4 g/cm^2 tantalum target with a 40 μA 500 MeV proton beam. An estimated 2–3 ^{32}Na atoms per second were extracted by surface ionization and implanted at the centre of the arrays on an aluminized mylar tape. The tape served to remove long-lived daughters from the detection chamber, either continuously or at six-second intervals. β-detection from SCEPTAR cleaned up the spectrum by first removing unwanted γ-singles, and by providing veto of bremsstrahlung events via β-γ anti-coincidence (see TRIUMF Annual Report 2004, p.134-5).

The γ-ray intensities extracted in this work agree with those from Klotz *et al.* over a wide energy range. A notable exception is the 1973 keV transition in ^{32}Mg, where Klotz *et al.* extracted a stronger intensity using γ-γ coincidences, probably because of the presence in that experiment of the contaminant ^{128}In, which β-decays to ^{128}Sn with a 20% (absolute intensity) γ transition at 1973.86 keV. A number of weak, high-intensity γ-rays were observed that remain unidentified.

Attempts to use γ-γ coincidences to produce level

schemes are limited by the overall low count rates in the present experiment; nevertheless a few features were observed. First, the 694 transition originally assigned by Klotz *et al.* to ^{32}Mg was recently identified by Mach *et al.* as an $11/2^- \rightarrow 7/2^-$ transition in ^{31}Mg [Mach *et al.*, Eur. Phys. J. **A25**, 105 (2005)]. Coincidences observed in this work support the placement as made by Mach *et al.* (see Fig. 96 (top)). However, we find that a transition near 694 keV also appears to be in coincidence with the 885 keV and 1973 keV transitions in ^{32}Mg (see Fig. 96 (bottom)). As a result a new level is proposed in the level scheme of ^{32}Mg lying at ∼3553 keV, and the ∼695 placed as a transition from ∼3553 keV → 2858 keV in ^{32}Mg.

Another transition at 1665.6 keV is tentatively placed by this work using γ-γ coincidences as belonging to the level scheme of ^{32}Mg, from the accepted 2551 keV → 885 keV levels.

A paper describing this work is in preparation.

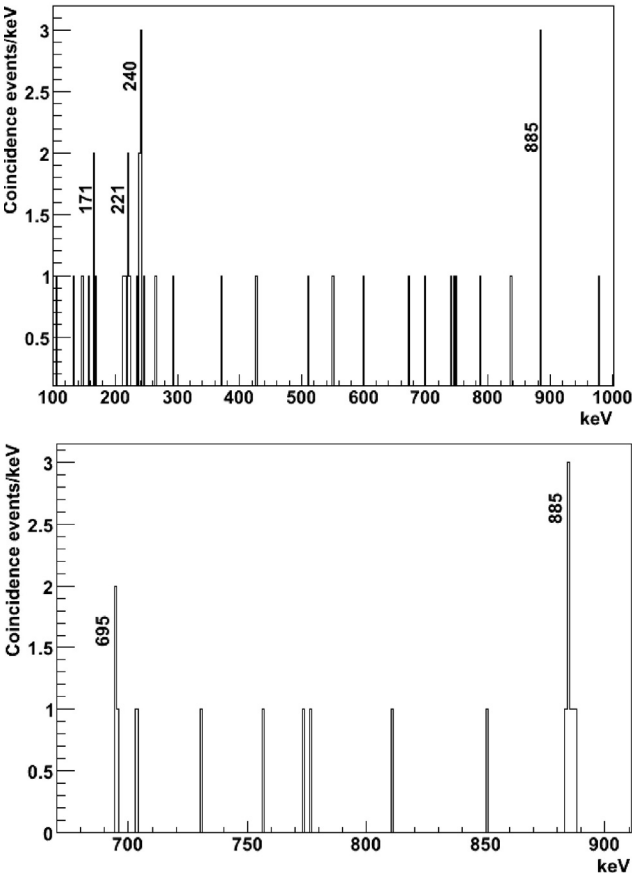

Fig. 96. Coincidence evidence suggesting a ∼695 keV γ belongs in ^{32}Mg. (top) Produced by a (691 keV – 697 keV) coincidence gate in the β-γ-γ spectrum. Both ^{31}Mg and ^{32}Mg (at 885 keV) are found in coincidence with transitions near 694 keV. (bottom) Produced by a (1971 keV – 1975 keV) coincidence gate in the γ-γ spectrum (no β coincidence requirement). 885 and ∼695 are found in coincidence with the 1973 keV γ.

Experiment 956
Search for tensor interactions in recoil nucleus singles in decay of polarized ^{80}Rb
(J.A. Behr, M.R. Pearson, TRIUMF; K.P. Jackson, TRIUMF/SFU)

Scientific motivation

The recoiling daughter nuclei from the β-decay of polarized nuclei have spin asymmetry $A_{\rm recoil} \approx 5/8\ (A_\beta + B_\nu)$ [Treiman, Phys. Rev. **110**, 448 (1958)]. This vanishes in the allowed approximation for pure Gamow-Teller decays, making it a very attractive experimental observable because knowledge of the nuclear polarization at 1 to 10% level is sufficient to be competitive. Our novel capability of measuring the recoil nuclei from laser-polarized cold atoms allows this observable to be measured now.

From data taken in December, 2004 we deduced $A_{\rm recoil} = -0.013 \pm 0.036$. We have taken a much larger data set with an upgraded experimental set-up in December, 2005.

Theory Right-handed vector currents do not contribute, so $A_{\rm recoil}$ is sensitive to lepton-quark tensor interactions. A renormalizable interaction that Lorentz transforms like a tensor can be generated by the exchange of spin-0 leptoquarks [Herczeg, Prog. in Part. and Nucl. Phys. **46/2**, 413 (2001)].

The PIBETA collaboration has reported a statistically significant deviation from the standard model [Frlež, Phys. Rev. Lett. **93**, 181804 (2004)] in $\pi \rightarrow \nu e \gamma$ decay that could be explained by a finite tensor interaction. Experiment 956 would become competitive with other nuclear β-decay measurements if it achieves 0.01 accuracy in the recoil asymmetry [Herczeg, Phys. Rev. **D49**, 247 (1994)], while ∼0.001 level is needed to reach similar sensitivity to the tensor interaction indicated by the π decay experiments. Since the recoil asymmetry vanishes, the degree and knowledge of polarization achieved in Expt. 715 is already sufficient for Expt. 956.

Higher-order corrections "Recoil-order" corrections beyond the allowed approximation produce a nonzero $A_{\rm recoil}$ within the standard model. The decay of $I^\pi = 1^+$ ^{80}Rb is primarily to two states, 74% to the ground 0^+ state and 22% to the first excited 2^+ state. The $1^+ \rightarrow 0^+$ transition has higher-order correction form factors b weak magnetism, and d induced tensor. We estimate $A_{\rm recoil}$ to be ∼–0.03 by using $b = 4.7\ Ac$, where A is the atomic number and c the Gamow-Teller matrix element. (This ignores a matrix element of orbital angular momentum contributing to b, and the d term entirely). The recoil-order terms have a different dependence on recoil momentum that may allow us to

extract them from the allowed and fundamental tensor terms.

The 1^+ to 2^+ transition includes several higher-order form factors that would need nuclear structure calculations. We have used an 80% high-purity germanium detector to measure $A_{\rm recoil}$ in coincidence with the 617 keV γ-ray that tags this state, so that we can subtract it off experimentally, leaving the simpler $1^+ \rightarrow 0^+$ transition asymmetry to interpret.

Experimental geometry

The geometry is shown in Fig. 97. The detector for ^{80}Kr recoils is the same system as for Expt. 715: a microchannel plate (MCP) with position sensitive readout, and a uniform electric field for collecting ions. We have added an additional MCP to detect low-energy atomic shakeoff electrons. All of the positive ions produced in β^+ decay will produce at least one electron. The solid angle of the Expt. 715 β^+ detector was 1%, so this technique increases the efficiency for recoil detection by ≈50 times.

The ^{80}Rb atoms are polarized by switching off the MOT light and optically pumping for 20 μs. The MOT 5 G/cm quadrupole field stays on. A small bias field of ≈2 G to help hold the polarization is applied by attenuating two of the retroreflected beams in the MOT horizontal plane, which moves the atoms to an equilibrium position at finite magnetic field. (The atoms are then moved back to centre with the 2 G uniform field.) This short duty cycle minimizes the motion of the cloud during the optical pumping time, which was a dominant systematic in Expt. 715 ^{37}K tests. By toggling the optical pumping light in frequency between the two polarizations, the cloud position was kept the same to better than 0.2 mm, and very similar polarizations achieved. The position is monitored by non-resonant photoionization with a pulsed laser.

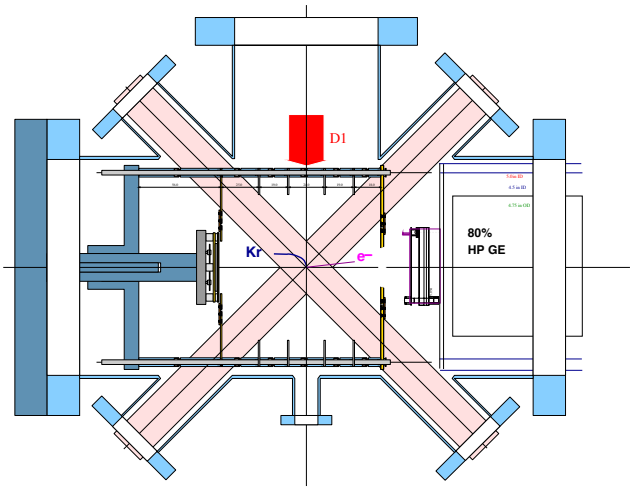

Fig. 97. TRINAT apparatus as modified for Expt. 956, showing new electron detector and HPGe detector. D1 light from a 50 mW diode laser optically pumps the ^{80}Rb.

The nuclear vector polarization achieved is between 60 and 70%. This was measured by the time dependence of the atomic excited state population during the optical pumping. It was independently measured by the β^+ asymmetry using the plastic/CaF_2(Eu) phoswich detectors, in coincidence with shakeoff electrons to minimize sensitivity to decays from untrapped atoms. The phoswiches are located at ±30° with respect to the polarization direction.

The ^{80}Rb ion beam from ISAC was ∼1 to 2×10^9/s from a zirconium target with a tantalum ionizer (to suppress Cu ionization for another experiment.) The number of atoms trapped was ≈1 to 2×10^6.

Electron detector details We demonstrated, using electrons from laser photoionization, that we have achieved ≈45% efficiency for electron detection. The field for the positive ion collection is made more uniform by biasing the grid in front of the electron detector to a potential close to that of the final electrodes in the field assembly.

We show a typical TOF spectrum in Fig. 98. The upper figure is predominantly ^{80}Kr ions. The lower figure was measured with the electron MCP biased to exclude atomic electrons from the trap. Most of the resulting 3% background can be attributed to β^+ detection. An additional background appears to be secondary electrons collected from β^+s striking material near the ion MCP.

Asymmetry We show raw data from the resulting recoil asymmetry for several charge states in Fig. 99. Different fractions of the angular distribution are collected from the different charge states, so this will provide an important systematic consistency check.

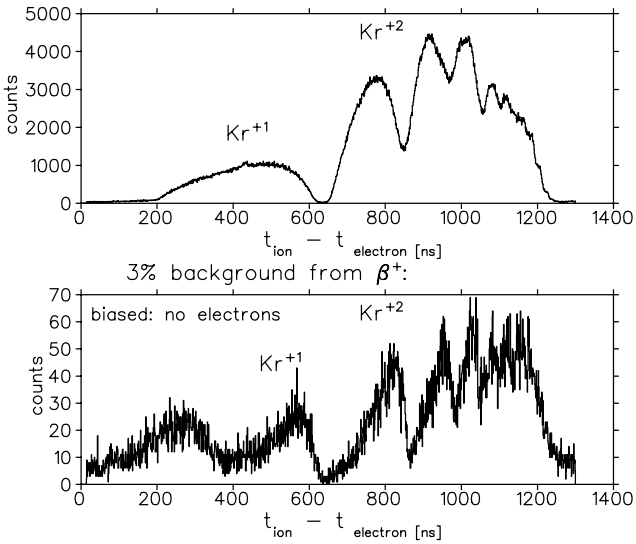

Fig. 98. Top: Time-of-flight spectra for recoil coincidences with shakeoff atomic electrons. Bottom: background with electrons excluded from detector, mostly β^+. See text.

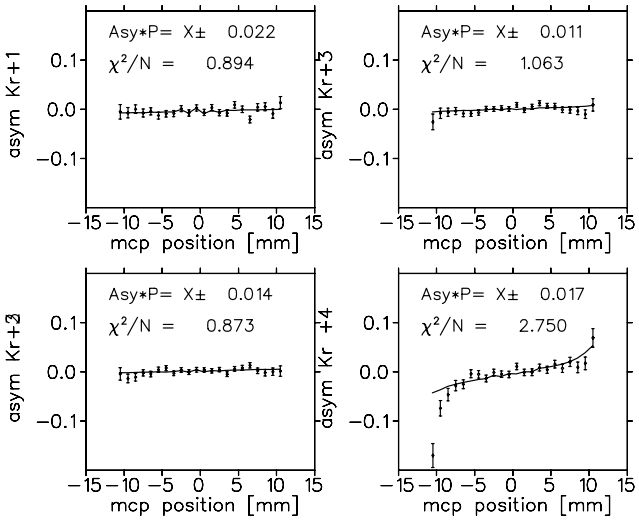

Fig. 99. Asymmetry for 1/3 of the data for the first 4 charge states, with very simple model fit to estimate statistical accuracy.

Summary and future For Expt. 956, we have collected data for a statistical error of ≈0.005 in the asymmetry. Analysis is proceeding. This experiment constitutes the main component of the M.Sc. for students R. Pitcairn and D. Roberge, UBC. Possible extensions of this experiment would include measuring the same quantity in ^{82}Rb as a nuclear structure consistency test, and measurements in ^{47}K decay.

The high-statistics electron detector technique looks very promising for a number of other TRINAT experiments, both for the recoil singles asymmetry measurements and to clean up the β asymmetry. Isospin mixing effects in ^{36}K decay could now be measured via the recoil asymmetry, which is directly sensitive to the Gamow-Teller/Fermi interference term induced. Competitive statistics for the ^{37}K recoil asymmetry, sensitive to right-handed currents, could now be obtained in about 1 week (see the Expt. 715 section of this Annual Report). The ^{74}Rb isotope shift now becomes a more practical measurement, and would yield the charge radius needed for isospin mixing corrections to its ft value. The upgraded ^{38m}K β-ν measurement will also include this technique (see the Expt. 1070 section of this Annual Report).

Experiment 964
TACTIC – TRIUMF annular chamber for tracking and identification of charged particles
(G. Ruprecht, TRIUMF)

TACTIC is a cylindrical time projection chamber for the detection of low-energy ejectiles from nuclear reactions. It allows the three-dimensional reconstruction of ion tracks by means of a two-dimensional anode array combined with a time-of-flight measurement of the drift electrons. Although it will be used as a facility for many experiments, its design parameters are mainly dictated to resolve the ^{4}He(^{8}Li,^{11}B)n reaction at astrophysical energies. For more details see last year's Annual Report, or visit the TACTIC Web site http://tactic.triumf.ca .

The cylindrical design is possible by utilizing gas electron multiplier (GEM) foils as a first stage of amplification. For information on GEMs see Sauli and Sharma [Ann. Rev. Nucl. Part. Sci. **49**, 341 (1999)] and Sharma and Pauli [Nucl. Instrum. Methods **A350**, 470 (1994)]. The planar test chamber we used last year has been improved to allow for sub-atmospheric pressures down to 100 mbar. With a 5486 keV α source and a 90% He/10% CO_2 gas mixture the gain of the GEM has been determined. At 100 mbar the signals are still on an acceptable level, though the range of operating voltage between noise and break-down is much smaller (see Fig. 100).

A sizeable effort has gone into creating a GEANT4 simulation for TACTIC in which all ion relevant processes can be simulated. The largest effort went into writing a Coulomb elastic scattering code to replace the GEANT4 built-in multiple scattering process (MSC). The MSC code assumes a light projectile moving in a dense medium where the nuclear scattering centres are heavy and fixed in position. Each step in the MSC process assumes a number of single scatterings and statistical methods are employed. Clearly this code will not work for the TACTIC environment where the projectile is a heavy ion with a mass comparable to the scattering centres which are nuclei in a tenuous gas. A single scattering process code was written based on a screened Thomas-Fermi potential model [Nucl. Instrum. Methods **130**, 265 (1975)] and, unlike the GEANT4 MSC process, can even produce recoils, so the full cascade of ions could be simulated. This code has the advantage that it can also be used to generate the correct large angle distribution of ^{8}Li+α scatter-

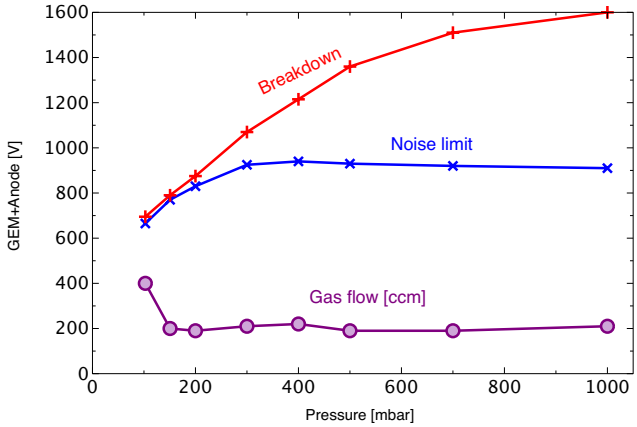

Fig. 100. GEM voltage operating range for different pressure ranges.

ing events where the ^{8}Li and α ions enter the drift region and become a background for the ^{4}He(^{8}Li,^{11}B)n events. The simulations show that most of the ^{4}He recoils do not reach the drift region and that the number of ^{8}Li ions will be tolerable. Figure 101 depicts the situation.

The drift field was modelled using FEMLAB. By numerical integration using the measurements of Peisert and Sauli [CERN 84-08, 1984, http://tactic.triumf.ca/cern] the total drift times for electrons released at the cathode at different z-positions were obtained. If nothing is done to fix the end cap fields, the cylindrical field becomes inhomogeneous and the drift times of the electrons become a strong function of the longitudinal position in the chamber. FEMLAB showed that voltage supporting rings at both end caps will correct this deficiency and make the drift times constant over most of the region (see Fig. 102). These results are discussed in a TACTIC resource document available on the Web [Kirchner, http://tactic.triumf.ca/publications].

A precise numerical calculation of the motion of the electrons in the drift medium is in progress at the University of York, using the Garfield/Magboltz package from CERN. The results for the drift times and diffusion of the electrons will be included in the GEANT simulation.

The VF48 flash ADC board, a VME based flash ADC board under development at the University of Montréal, has been designated as the main data quantizing device. Both pulse shape and timing of the anode signals will be digitized. Most of the development this year has gone into correcting a defective firmware problem. The designated MIDAS/ROOT-based data acquisition system, ROME [http://midas.triumf.ca], was found not to be fast enough to process the incoming data stream and inadequate for visual displays of ion tracks. A new ROME extension, ARGUS, is going to be tested. However, it will probably be necessary to write a special MIDAS/ROOT-based data aquisition system.

With the improved GEANT4 simulation and the detailed electric field calculation, the final design could be fixed. The technical drawings are now being drawn up at Daresbury and the prototype chamber will be constructed at the University of York. The chamber is expected to be ready for first beam tests at the end of 2006. Figure 103 shows a three-dimensional sketch of the final design combined with the ion trajectories as simulated with GEANT4. More details of the TACTIC chamber can be found in the European Journal of Physics on-line article (2006) [http://dx.doi.org/10.1140/epja/i2006-08-048-y].

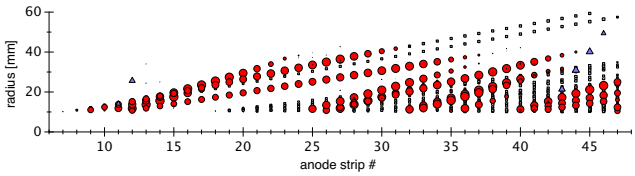

Fig. 101. Simulated ion tracks for the ^{8}Li+^{4}He reaction as seen by the 48 anode pads which can detect only electrons from the drift region (r = 10–60 mm). Circles = ^{11}B, squares = ^{8}Li, triangles = ^{4}He. The size of the symbols reflects the energy collected per anode strip.

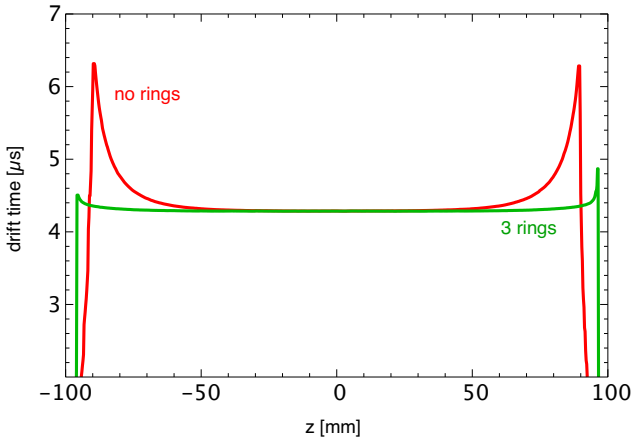

Fig. 102. Drift time of the electrons from the cathode (−500 V) to the anode (0 V) for a 90% Ar/10% CO_2 gas mixture at STP. Close to the end of the drift region (here at $z = \pm 100$ mm) the field is too inhomogeneous so that only 50% of the drift region could be used. Three voltage supporting rings increase this region to 90%.

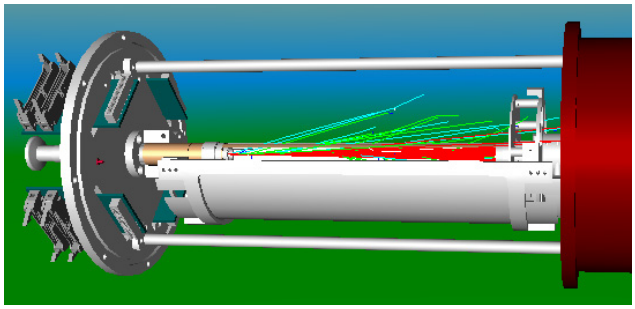

Fig. 103. Sketch of the entire TACTIC. The ^{8}Li beam comes from the left and it expands as a solid envelope to the right due to scattering with the target gas in the target region. A few of the ^{8}Li and ^{4}He tracks make it into the drift region, however, most of the tracks in the drift region are from ^{11}B ions.

Experiment 973
Study of coexisting collective phases far from stability: systematic decay spectroscopy of the $N = 90$ isotones

(W.D. Kulp, J.L. Wood, Georgia Tech.)

Introduction

The nuclei with 90 neutrons are receiving intense interest currently because they exhibit collective be-

haviour which suggests competition between very different shapes or phases [Nuclear Science Advisory Committee, *Opportunites in Nuclear Science. A Long Range Plan for the Next Decade* (2002)]. Using the 8π and PACES with the Moving Tape Collector, we have initiated a very detailed study of these exciting issues at TRIUMF. This has been built on earlier experience with the 8π when it was at LBNL: our program there established the 8π as a tool for unprecedented high-precision, high-sensitivity γ-ray spectroscopy in the elucidation of complex nuclear structure questions [Kulp *et al.*, Phys. Rev. Lett. **91**, 102501 (2003); *ibid.*, Phys. Rev. **C69**, 064309 (2004); *ibid.*, **C71**, 41303 (2005); *ibid.*, **C73**, 014308 (in press)].

Nuclear structure can be broadly divided into states that have positive parity and states that have negative parity – classified as quadrupole and octupole degrees of freedom, respectively in collective nuclei. Such classes of states are connected by electric dipole, $E1$ transitions which have very weak internal conversion. Nuclear structure can also be broadly divided into states with different shapes (deformation) or different phases. Such classes of states are generally connected by $E0$ transitions [Wood *et al.*, Nucl. Phys. **A651**, 323 (1999)] which cannot occur by γ-ray emission. Of particular interest in this study is the identification and placement of $E1$ and $E2$ (electric quadrupole) transitions for identification of band structures and the measurement of $E0$ transitions for interpretation of the nature of the bands.

Evolution of the pentagonal array for conversion-electron spectroscopy (PACES)

The pentagonal array for conversion-electron spectroscopy (PACES) developed at LSU by Ed Zganjar is an array of 5 Si(Li) detectors which makes available both conversion-electron and internal-pair spectroscopy. Inclusion of conversion-electron data provides not only multipolarity information, but also reveals the crucial $E0$ transitions indicative of shape coexistence. First used in the ^{156}Ho decay study, PACES included only three Si(Li) detectors and achieved a modest resolution of 4 keV FWHM at 975 keV.

In order to improve the detector resolution, two major design issues needed to be addressed: cooling and electronic noise. The cold-finger for PACES is 2 ft long (in order to get to the centre of the 8π array), and it is hollow (a 1 in. diameter hole down the axis) to allow the beam to pass through, thus cooling the Si crystals and FETs in the array is quite challenging. The cramped space of the 8π structure prevents mounting the full preamplifier assembly for each Si detector within the 6 in. maximum distance recommended by the manufacturer.

To address the cooling problem, a change was made such that LN2 went into the cryostat directly using a gravity feed dewar rather than through a flange which requires that heat be conducted through a copper rod connecting the LN2 dewar and the cold-finger inside the beam line. This modification brought the temperature down to the required values for the crystals (about 95 K to reduce the kT noise). With adjustments to the FET mounts, the FETs were set to an optimum 110 K.

To address the electronic noise issue, the preamps were modified at LSU to perform best with the unique set-up for the 8π structure. The long leads between the front-end of the pre-amps (the cold part with the FETs) and the remainder were 18 in., far longer than the manufacturer specifications, and the electronics needed to be adjusted to achieve better performance. With those modifications a nominal resolution of 2.0 keV at 1 MeV was achieved, and separation at the Bi $K_{\alpha 1}$ and $K_{\alpha 2}$ X-rays can be observed in the spectra shown in Fig. 104.

Decay of ^{156}Ho to ^{156}Dy

Nearly 750 GB of data on the decay of ^{156}Ho to ^{156}Dy were collected in an 11-day experiment in 2004. This first stage of Expt. 973 was also the first pairing of the 8π spectrometer with the PACES array. Data analysis is currently under way at Georgia Tech.

Decay of ^{158}Tm to ^{158}Er

Beam time for the study of the decay of ^{158}Tm to ^{158}Er was allocated in August. Figure 105 shows γ-ray and conversion-electron spectra for the beta decay of ^{158}Tm (3.98 min) to ^{158}Er from this run. The γ-ray lines are matched to the conversion electron lines (by an energy shift equal to the K-binding energy for $Z = 68$ (Er). Dramatic differences in line intensities for the two spectra are observed, due to the extraordinary sensitivity that the internal conversion process possesses with respect to spin changes and parity changes for nuclear transitions.

The power of combining PACES with the 8π is evident in Fig. 105, as one can immediately identify the $E0$ and $E1$ transitions in the spectra shown. The lines at 706, 794 and 815 keV which are strong in the γ-ray spectrum and weak or invisible in the electron spectrum are parity-changing $E1$ transitions. Lines at 597, 631, 730, 797, and 806 keV which are strong in the electron spectrum and weak or invisible in the γ-ray spectrum are transitions with electric monopole components, $E0$ (in some cases pure $E0$ transitions).

The spectra shown in Fig. 105 are evidence that the 8π+PACES spectrometer array can easily identify cornerstone features of unstable nuclei even when the spectra involved have great complexity. The added capability of observing coincidences between γ pairs, electron pairs, and γ–electron pairs enables detailed

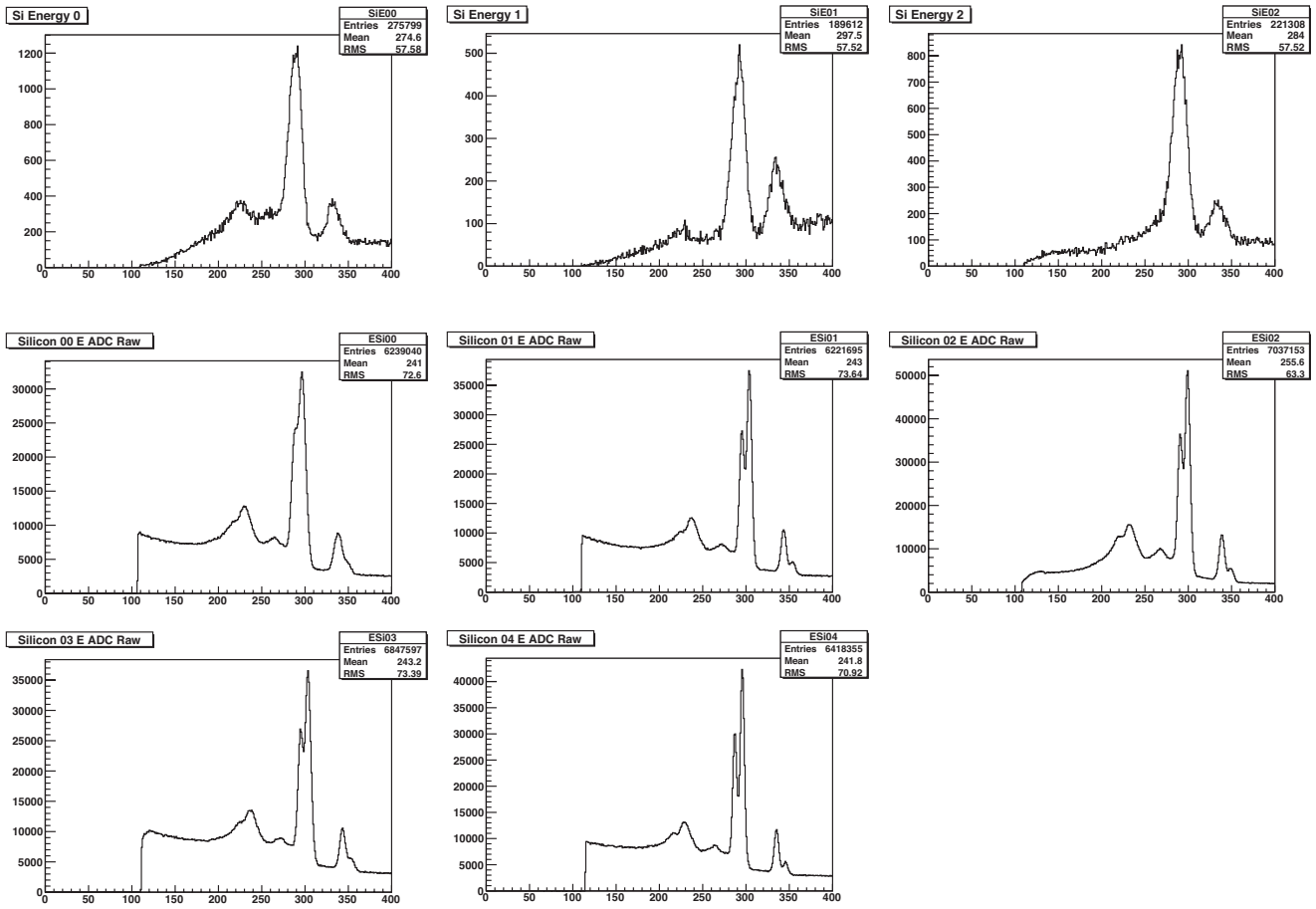

Fig. 104. Conversion-electron spectra from calibration of PACES with a ^{207}Bi source. The top three spectra show the Pb K_α X-rays during the 2004 run, and the following five spectra show the same lines from the 2005 run, after modification to PACES.

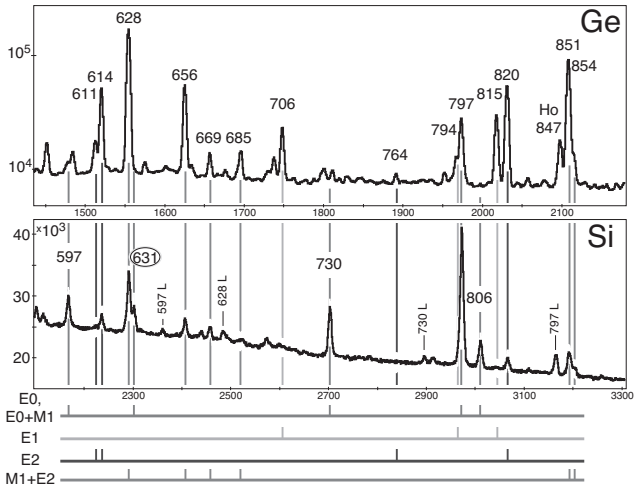

Fig. 105. A comparison of the γ-ray spectrum from the 8π with the conversion-electron spectrum measured using PACES can be used to determine the multipole character of nuclear transitions. See the text for a discussion of individual lines in the spectra.

band structure and very weak decay branches to be elucidated, thus leading to collective band structures and the presence of selection rules (weak or unobserved transitions) which are critical for the elucidation of collective nuclear characteristics.

With the refurbishment of the 8π γ-ray detector and its greatly extended spectroscopic capability, it now functions as the best high-sensitivity, high-precision, multi-spectroscopy facility in the world.

Experiment 973 is a collaboration of scientists from Georgia Tech., Colorado School of Mines, Louisiana State University, McMaster University, Oregon State University, Saint Mary's University, Simon Fraser University, TRIUMF, University of Guelph, University of Surrey, University of Toronto, University of Vienna, and Youngstown State University.

Experiment 989
Astrophysical studies using ^{26}Al ground-state and isomeric beams
(C. Ruiz, TRIUMF)

Over the course of 2005, the DRAGON collaboration has undertaken an extensive campaign to measure the ^{26g}Al$(p,\gamma)^{27}$Si reaction. With test runs and measurement attempts up until and including the summer of 2005, a final push was made in the fall of this year resulting in the first measurement of this reaction in inverse kinematics providing new information which will determine the influence of this reaction in nova nucleosynthesis.

Motivation

The Galactic ^{26g}Al distribution has been mapped by COMPTEL and partially investigated by INTEGRAL and RHESSI via its characteristic 1809 keV γ-ray. Particular details of this distribution suggest that most of the ^{26}Al seems to coincide with regions of large star formation rate, suggesting young high-mass progenitors such as core collapse supernova (CCSN), asymptotic giant branch (AGB) or Wolf-Rayet stars.

However, hydrodynamic nova models predict a very significant amount of synthesized ^{26}Al, in some cases up to 20% of the observed distribution.

In order to have confidence in the nova models and the amount of synthesized ^{26}Al, all the reaction rates in the so-called MgAl cycle must be known accurately in the energy region relevant to nova temperatures.

In this region, the ^{25}Al$(p,\gamma)^{26}$Si and ^{26g}Al$(p,\gamma)^{27}$Si reactions stand out as the most uncertain and have a very significant influence on the final amount of ^{26}Al synthesised in the nova. In particular, a low energy resonance previously thought to lie at $E_{C.M.} = 188$ keV is known to dominate the ^{26g}Al$(p,\gamma)^{27}$Si reaction rate at nova temperatures. The strength of this resonance was thought to be around 55 $\pm$ 9 μeV based on a previously unpublished measurement attempt in normal kinematics using an ^{26}Al implanted target. Nova modellers have expressed that this strength is critical enough that extensive investigation of its true value be carried out. DRAGON undertook to measure this strength directly with the goal of either confirming the previously measured value or accurately measuring its true value, if different.

Experimental method

A high-power silicon carbide target was bombarded with up to 70 μA of 500 MeV protons from the cyclotron producing radioactive ^{26g}Al which then diffused out of the target and into the ISAC surface ionization source. An enhancement to the surface ionization of up to a factor 8 was provided using the TRILIS laser ion source.

The DRAGON recoil separator consists of a windowless hydrogen recirculating gas target surrounded by an array of 30 BGO detectors, and two stages of electromagnetic mass separation. The total separator length from the centre of the gas cell to the final focus is 20.42 m, and during this experiment a double-sided silicon strip detector (DSSSD) was placed 65 cm downstream from this position.

A collimated silicon surface barrier detector placed at 30° from the centre of the gas cell was used to detect elastically scattered protons from incoming beam during the run as a means of normalization. These spectra were compared to Faraday cup readings, measurements of gas target beam transmission and measurements of the average beam charge state after gas to provide the number of incident ions on target to 5%.

The separator was set to accept 4+ silicon recoils from the reaction ^{26g}Al$(p,\gamma)^{27}$Si which were then detected using the DSSSD in coincidence with prompt γ-rays detected in the BGO array. The majority of unreacted beam ends up impinging on the left slit at the mass-focus after the first electric dipole. As a primary means of background rejection, the time-of-flight through the separator was measured to eliminate random coincidences caused by radioactive beam contaminants and room background.

The contaminants in the beam were primarily radioactive ^{26}Na ($t_{1/2}$=1.07 s) and ^{26m}Al ($t_{1/2}$=6.345 s) created in the SiC target, efficiently ionized and, sufficiently close in mass to ^{26g}Al to be not completely resolved using the mass separator. The level of these contaminants in the beam was monitored during the run; the ^{26}Na via its characteristic 1809 keV γ-ray from beta-decay to the first excited state of ^{26}Mg using a high-purity germanium detector; the ^{26m}Al via paired 511 keV γ-rays created from electron-positron annihilation caused by β^+ decays of this isomer at the mass slits. The ^{26}Na contaminant was the major source of background in the experiment due to the small fraction of beam which would be implanted in the entrance aperture to the gas cell causing a high rate in the BGO array and stimulating more random coincidences. With a combination of a mechanical iris device upstream of the gas cell designed to remove the source of beam decay away from the detectors and some fine tuning of the mass separator optics, we were able to reduce the level of ^{26}Na in the beam from 1:32,000 to 1:337,000, with a contribution to the BGO rate equal to that of room background. The level of ^{26m}Al contaminant remained at around 1:30,000 during the run.

During the run, a gas target pressure of 6 torr was maintained to within $\pm$1.6%. Initially a beam energy of 201 keV/nucleon was chosen to place the 188 keV resonance at the centre of the gas target and over 179

hours of data were taken at an average intensity of 2.5 $\times 10^9$ ions/sec at this energy, although peak intensities of over 5 $\times 10^9$ ions/sec were achieved. Some 49 hours of data were taken at an energy of 197 keV/nucleon, and an off-resonance background run was taken at 225 keV/nucleon for 30 hours.

Analysis and results

True ^{27}Si recoils were identified by their unique time of flight through the separator and their final energy at the silicon strip detector. Background caused by randomly coincident leaky beam was subtracted by a variety of methods. Figure 106 shows a sample plot of separator time of flight versus coincident heavy-ion energy for a selection of 201 keV/u runs, showing the clear ^{27}Si peak. The background, mostly caused by ^{26}Na, was partly reduced during this set of runs.

The stopping power of ^{26}Al in the H_2 gas was measured for each beam energy during the experiment using the calibrated DRAGON dipole magnet. Charge state distributions were measured for various gas pressures using a ^{28}Si beam of several nA, allowing the selected 4+ charge state efficiency for the separator to be determined. Separator efficiency was modelled using GEANT, and the efficiency of the BGO array was also modelled using GEANT and compared to actual source measurements. The sensitivity of the efficiency to the gamma-branching ratios was also investigated.

We find a resonance strength which is approximately 60% smaller than previously thought, with a similar measurement uncertainty as the previous unpublished study. In addition, we have measured a resonance energy several keV lower than previously thought via investigations of the z-coordinate distribution of the BGO detectors that were struck with the most energetic γ-ray in each reaction (see Fig. 107). Both these results will have a bearing on

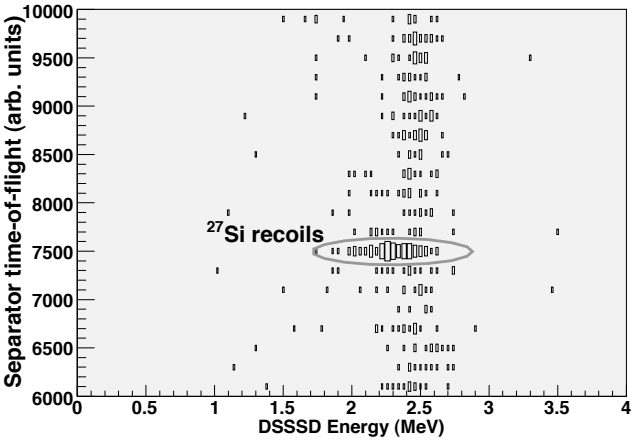

Fig. 106. Separator time of flight versus particle energy for γ-ray heavy-ion coincidences, showing true ^{27}Si recoils lying on a background of "leaky" beam.

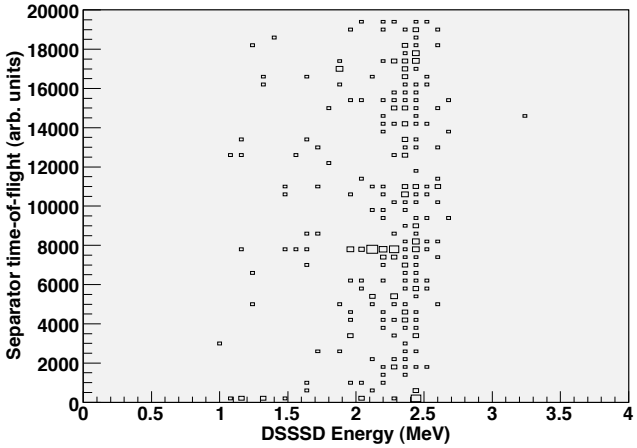

Fig. 107. z-coordinate of highest energy coincident γ-ray for 197 keV/u run in which resonance was centred in the gas target (y-axis shows counts per bin).

the temperature-dependent reaction rate in nova environments. Hydrodynamic simulations of nova explosions will be used to determine the influence of these results on the synthesized ^{26}Al in these scenarios, leading to a better understanding of the contribution novae make to Galactic ^{26}Al and further constraining nova models. The results of this experiment will be submitted to Physical Review Letters for publication.

Experiment 991
Nuclear charge radius of ^{11}Li
(W. Nörterhäuser, GSI/Mainz, for the ToPLiS collaboration)

The ^{11}Li nucleus exhibits a halo structure – a diluted neutron matter surrounding a ^{9}Li-like core. Despite many attempts from the experimental and theoretical side to resolve the puzzle of its nuclear structure during the last two decades, details of the interaction between the halo and the core are still not well understood. Particularly, the question whether the ^{9}Li core is decoupled from the halo in the sense that it is not modified from the free ^{9}Li nucleus is still open. A modification of the core can be probed by measuring the change in the nuclear charge radius between ^{9}Li and ^{11}Li. Such a difference can only be determined with a measurement of the isotope shift in an atomic transition. The isotope shift has the advantage that it is very sensitive and provides nuclear-model independent values for the nuclear charge radii. A shift in frequency (the isotope shift, $\delta\nu^{A,A'}$) of a spectral resonance is produced by the change in the nuclear mass (mass shift, $\delta\nu^{A,A'}_{\rm MS}$) and the nuclear charge distribution (field shift, $\delta\nu^{A,A'}_{\rm FS}$). For lithium the mass shift is ten thousand times larger than the field shift. Thus both, high resolution isotope shift measurements and accurate atomic calculations for the mass shift are required

to extract nuclear charge radius information with a relative precision of a few per cent.

On the experimental side, an on-line laser and mass spectroscopic technique was developed at the GSI facility, Germany, to measure the isotope shift in the $2s\,^2S_{1/2} \rightarrow 3s\,^2S_{1/2}$ Doppler-free two-photon electronic transition in lithium. The technique is efficient enough to overcome the short half-life and low abundance of the radioactive lithium isotopes. First measurements were performed on $^{6-9}$Li at GSI in 2003. In 2004, the experimental apparatus, shown schematically in Fig. 108, was moved to the ISAC facility, which delivered about 30 000 $^{11}Li^+$/s to the experiment. The lithium ions with 30 keV kinetic energy were stopped in a hot thin carbon foil, neutralized and released as an atomic cloud into the low-field source region of a quadrupole mass spectrometer (QMS). There, they crossed through the focus of two overlapped laser beams which were enhanced ∼100 times with an optical cavity. The atoms were reionized via doubly resonant four photon ionization: $2s \xrightarrow{2\times 735\,\mathrm{nm}} 3s \xrightarrow[30\,\mathrm{ns}]{\mathrm{decay}} 2p \xrightarrow{610\,\mathrm{nm}} 3d \xrightarrow{610/735\,\mathrm{nm}} Li^+$. The created photo ions were mass analyzed with the QMS and detected with a continuous dynode electron multiplier detector.

The titanium:sapphire laser was stabilized relative to a diode laser locked to a hyperfine-line of I_2.

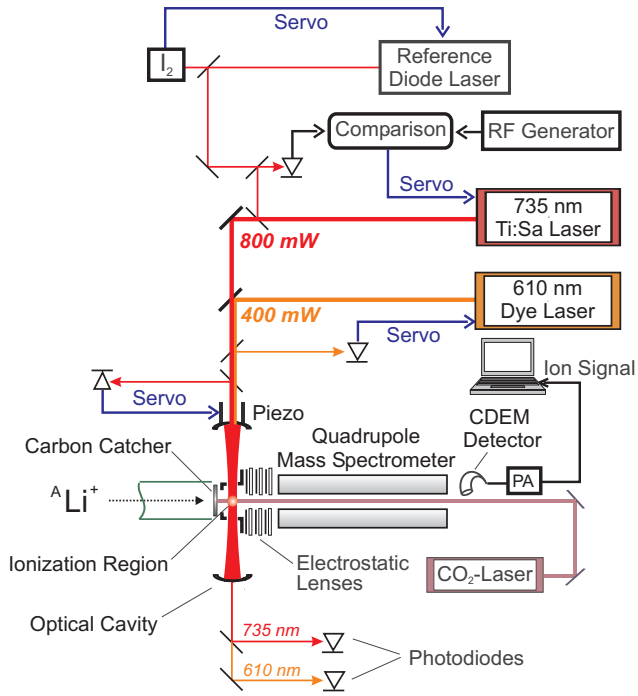

Fig. 108. Simplified experimental set-up to measure the $2s \rightarrow 3s$ Doppler-free two photon transition as explained in the text.

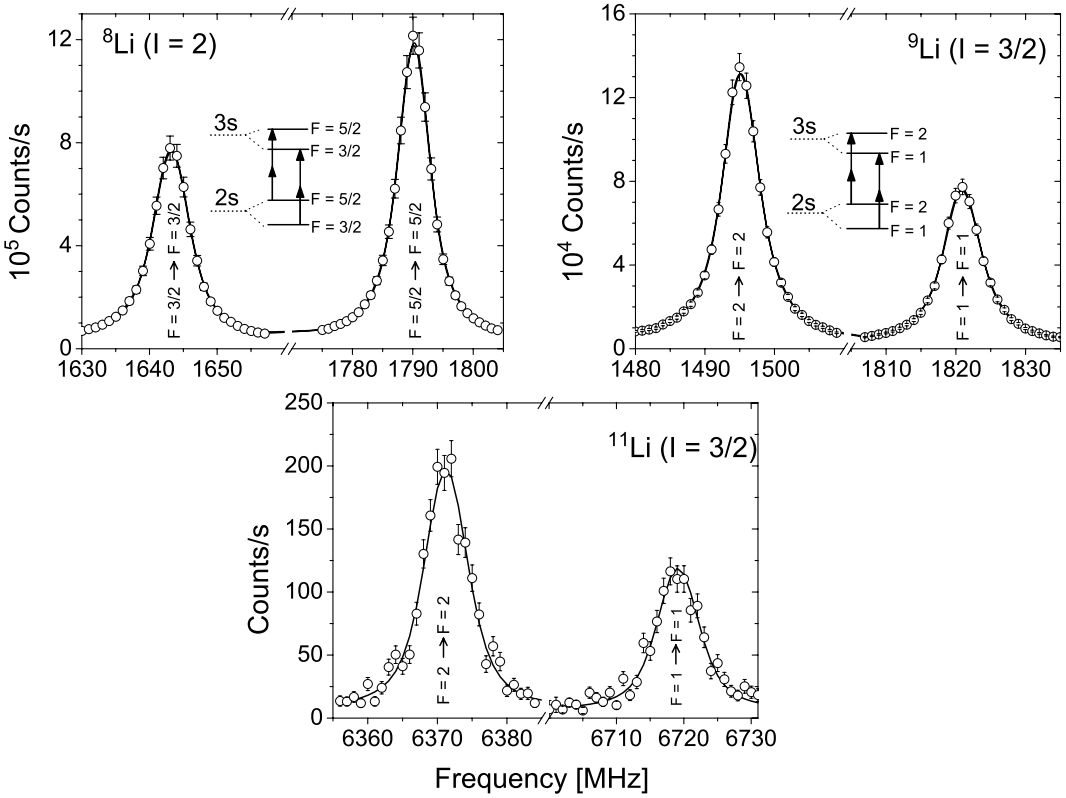

Fig. 109. Examples of spectra of the $2s \rightarrow 3s$ transition recorded for $^{8-11}$Li at ISAC in September and October, 2004.

The nuclear spin of the isotopes gives rise to a hyperfine structure and the resonance pattern is governed by the selection rule $\Delta F = 0$ for an $s \rightarrow s$ two-photon transition. For ^{11}Li, twenty-four such spectra were obtained over six days of beam time. These measurements were interspersed with measurements on ^{6}Li, which served as experimental reference.

Isotope shifts of the centre of gravity of the observed hyperfine transitions relative to ^{7}Li were calculated and results for ^{6,8,9}Li are in good agreement with those previously observed at GSI. A value of $\delta\nu^{11,7}_{\mathrm{IS,exp}} = 25,101.226(125)$ MHz was measured for ^{11}Li.

On the theoretical side, the quantum mechanical three electron problem for low Z was solved to high accuracy in the non-relativistic limit and the effects of relativity and quantum electrodynamics were included by perturbation theory. The various contributions to the mass shift were calculated from the resulting electron wave functions.

Nuclear charge radii of the lithium isotopes could be extracted from the combination of isotope shift measurements and mass shift calculations using the following expression

$$r_{\mathrm{c}}^2(^{\mathrm{A}}\mathrm{Li}) = r_{\mathrm{c}}^2(^{7}\mathrm{Li}) + \frac{\delta\nu^{\mathrm{A,7}}_{\mathrm{IS,exp}} - \delta\nu^{\mathrm{A,7}}_{\mathrm{MS}}}{-1.5661\ \mathrm{MHz/fm}^2}\ ,$$

where the root mean square nuclear charge radius of ^{7}Li measured by electron scattering, $r_{\mathrm{c}}^2(^{7}\mathrm{Li}) = 2.390(30)$ fm, was taken as reference. The results obtained are shown in Fig. 110. The charge radius of ^{11}Li is found to be 2.467(37) fm – which is clearly larger than ^{9}Li – while from ^{6}Li to ^{9}Li the charge radii were monotonically decreasing from 2.517(30) fm to 2.217(35) fm.

In Fig. 110 different theoretical predictions for the nuclear charge radii of all lithium isotopes are included. From those models which were able to predict the ^{11}Li charge radius, the stochastic variational multi-cluster model shows the best agreement with the experimental result. This model considers light nuclei as composed of smaller clusters namely the α particle, the triton nucleus, and the nucleons p and n. This clustering allows us to focus on those degrees of freedom thought to be the most relevant to the physical behaviour of a given nucleus. Calculations for ^{11}Li were performed including neutron correlations as well as polarization of the ^{9}Li core by the halo neutrons. If core-excitation is not included, the model predicts a much smaller charge radius, only slightly larger than that of ^{9}Li. Thus, in the frame of this model, one can conclude that core-perturbations contribute significantly and must be included in order to reproduce the increase in charge radius from ^{9}Li to ^{11}Li.

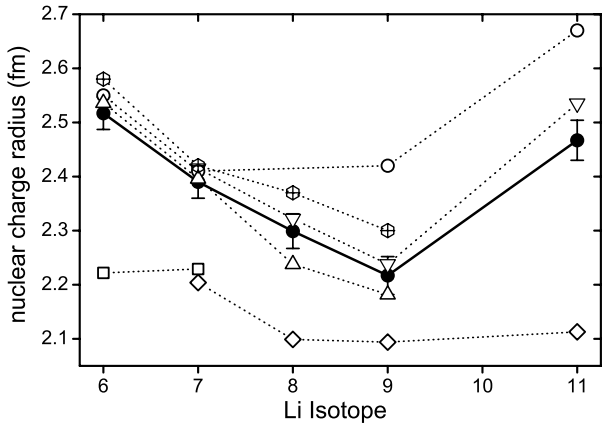

Fig. 110. Experimental charge radii of lithium isotopes (•) compared with theoretical predictions: △: Green's function Monte Carlo calculations, ▽: stochastic variational multi-cluster model, ⊕: Fermionic molecular dynamics, ○: dynamic correlation model, □ and ◇: *ab-initio* no-core shell model.

Experiment 992
Lifetime of the 4.033 MeV state in ^{19}Ne
(R. Kanungo, TRIUMF)

X-ray bursts are the astrophysical site for the *rp* process. In these stellar phenomena the temperature and density are sufficient to initiate a breakout from the hot CNO cycle, which involves elements with A < 20, into the *rp* process, creating heavier nuclei up to A ~ 100.

It is still an open question as to which is the most important reaction for this breakout. Currently the $^{15}\mathrm{O}(\alpha,\gamma)^{19}\mathrm{Ne}$ reaction is considered to be the most likely path for the initial breakout. This reaction mostly proceeds through resonances in ^{19}Ne which are located just above the ^{15}O+α threshold. It is important to know the rate of this capture reaction in order to ascertain its importance in explosive astrophysical processes. A direct measurement of this reaction rate is not trivial and requires a very high intensity low-energy ^{15}O radioactive beam.

On the other hand it is possible to estimate the resonant reaction rate from a knowledge of the α and γ decays including the branching ratio $\mathrm{B}_\alpha = \Gamma_\alpha/(\Gamma_\alpha+\Gamma_\gamma)$. If Γ_γ or Γ is also known then the resonance strength and the contribution of each resonance can be calculated. The first excited state above the ^{15}O+α threshold in ^{19}Ne is at 4.03 MeV. The α-decay branching ratio of this state has been studied by several reactions, leading to an upper limit $\mathrm{B}_\alpha = 4.3 \times 10^{-4}$ at the 90% confidence level [Davids *et al.*, Phys. Rev. **C67**, 065808 (2003)]. Prior to 2005, a large uncertainty existed regarding the lifetime of this state and hence its Γ.

We therefore performed an experiment at the ISAC facility to measure the lifetime of this level using the

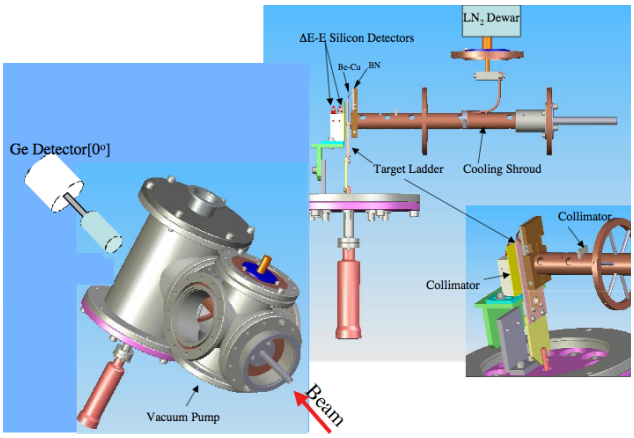

Fig. 111. A schematic view of the experimental set-up.

Doppler shift attenuation method. A schematic set-up of the experiment is shown in Fig. 111. The level of interest around 4.03 MeV in ^{19}Ne was populated in the one-neutron transfer reaction ^{3}He(^{20}Ne, ^{4}He)^{19}Ne using a ^{20}Ne beam accelerated to 34.4 MeV. The average beam intensity was ∼12 p nA. The reaction target was prepared by ^{3}He implantation at 30 keV in a Au foil (12.5 μm thick). A total of 6×10^{17} atoms was implanted at a depth of 0.1 μm. The recoiling ^{19}Ne nuclei were stopped in the Au foil while the α particles were transmitted through the foil and were detected using a silicon $\Delta E - E$ telescope. The γ-rays from de-excitation of the levels in ^{19}Ne were detected in an 80% HPGe detector placed 89 mm downstream of the target at 0°. To obtain an idea of the un-shifted peak energy a second HPGe detector was placed at 90°.

The scattering chamber was designed with a cold trap to ensure a clean target surface. This was achieved using a narrow differential pumping aperture followed by a copper cylinder enclosing the path of the beam to the target. The copper cylinder was cooled using liquid nitrogen. To avoid any condensation of impurities on the surface of the target, the copper cylinder was not in direct contact with the target ladder. An indirect contact of the cold copper cylinder to the copper target ladder was made using BeCu fingers mounted on a boron nitride plate. This arrangement maintained a temperature difference between the copper cylinder and the target ladder.

A clear peak was observed for the level of interest in ^{19}Ne in both the Ge detectors. Gamma transitions from other levels of ^{19}Ne were also observed. The lifetime of the level of interest is being determined from a lineshape analysis of the γ-ray detected in coincidence with the α particle in the silicon telescope. A preliminary analysis of the data suggests at the 2σ confidence level $\tau = 9.5^{+7.5}_{-6.0}$ fs for ^{19}Ne*(4.03 MeV). This is in agreement with the recent results reported by Tan *et al.* [Phys. Rev. **C72**, 041302 (2005)].

Experiment 1022
The resonant radiative capture ^{12}C(^{16}O,γ)^{28}Si reaction

(S. Courtin, F. Haas, IReS, Strasbourg)

Scientific motivations

Radiative capture is a process in which the incident projectile is absorbed by the target nucleus and the subsequent compound system is cooled by γ emission only. Such reactions have typically low cross sections because the electromagnetic force is weak compared to the nuclear force and the decay via particle emission is often 3 to 6 orders of magnitude more probable than the radiative decay. Light heavy-ion induced radiative capture measurements have been performed only for a few systems, of which ^{12}C+^{12}C and ^{12}C+^{16}O reactions have been the most studied. As for the ^{12}C(^{12}C,γ)^{24}Mg reaction, it was investigated in the 1980's using a large NaI detector and only high energy γ-rays ($E_\gamma \geq 18$ MeV) could be observed in the spectra due to the piling up of low energy transitions from fusion evaporation channels. A resonant excitation function was measured for this system for bombarding energies between 19 and 25 MeV. This reaction has known a renewed interest recently with the Jenkins *et al.* campaign of experiments at Berkeley (Gammasphere), Argonne (Fragment Mass Analyser) and TRIUMF (DRAGON) [Jenkins *et al.*, Phys. Rev. **C71**, 041301 (R) (2005)]. An unexpectedly high resonant capture cross section has been measured and the resonance decay has been shown to proceed dominantly through doorway states whose deformed structure overlaps with the ^{24}Mg entrance channel.

Concerning the ^{12}C(^{16}O,γ)^{28}Si reaction, strong resonant structures have been measured in the excitation function especially for bombarding energies between $E_{\rm CM} = 8$ and 10 MeV corresponding to ^{28}Si excitation energies between 25 and 27 MeV [Collins *et al.*, Phys. Rev. Lett. **49**, 1553 (1982)]. As in the ^{12}C+^{12}C study, the γ spectra obtained are dominated by an important background at low energy. This could be highly reduced with the use of a high performance 0° spectrometer. In the present experiment we have thus reinvestigated the ^{12}C(^{16}O,γ)^{28}Si reaction taking advantage of the highly selective DRAGON 0° spectrometer and the efficient associated BGO γ-array to study in detail the decay of two of the resonant structures at $E_{\rm CM} = 8.5$ MeV and $E_{\rm CM} = 9.0$ MeV. Measurements on and off these resonances have been performed to establish the relative importance of the decay branches to the g.s. ^{28}Si oblate band, to its prolate excited band and to eventual doorway states having a ^{16}O+^{12}C cluster configuration which are predicted to lie at E_X(^{28}Si) ∼15 MeV.

Experimental details

A 40 μg/cm^2 ^{12}C solid target was bombarded with a TRIUMF-ISAC ^{16}O beam at 3 energies: 20.01 MeV, 20.71 MeV and 21.18 MeV, respectively on the $E_{\rm CM}$ = 8.5 MeV resonance, off resonance and on the $E_{\rm CM}$ = 9.0 MeV resonance. The intensity of the ^{16}O beam was limited to ∼10 p nA to keep the acquisition dead time less than 20%. This is mainly due to the counting rate in the BGO array arising from low energy γ-rays from the fusion evaporation channels. The ^{28}Si recoiling nuclei were detected at the DRAGON focal plane using a double sided silicon strip detector and the coincident γ-rays were recorded in a 30 crystal BGO array covering 90% of 4π around the target chamber. Figure 112a shows a heavy-ion singles spectrum from the DSSSD obtained at E_L = 20.01 MeV (on the first resonance). This spectrum shows a peak at 8 MeV corresponding to the ^{28}Si recoils and a small peak at ∼5.5 MeV from a detector chamber α radioactivity. Figure 112b corresponds to the γ spectrum in coincidence with the ^{28}Si peak of spectrum a). This spectrum extends to 25 MeV, which is the excitation reached in ^{28}Si at the first resonance energy. It shows strong transitions among the low-lying ^{28}Si excited states: 1.79 MeV ($2^+ \rightarrow 0^+$) and 2.84 MeV ($4^+ \rightarrow 2^+$). The peaks observed around 4.5 MeV and 6.9 MeV probably correspond to the decays of the ^{28}Si 3^+ (6.28 MeV), 0^+ (6.69 MeV) and 3^- (6.88 MeV) states. Moreover, this spectrum displays a clear and broad structure between $E \sim$ 11.9 MeV and $E \sim$ 15.8 MeV, centred at $E_\gamma \sim$ 13.4 MeV, showing that the decay of the $E_{\rm CM}$ = 8.5 MeV resonance also proceeds via intermediate ^{28}Si states.

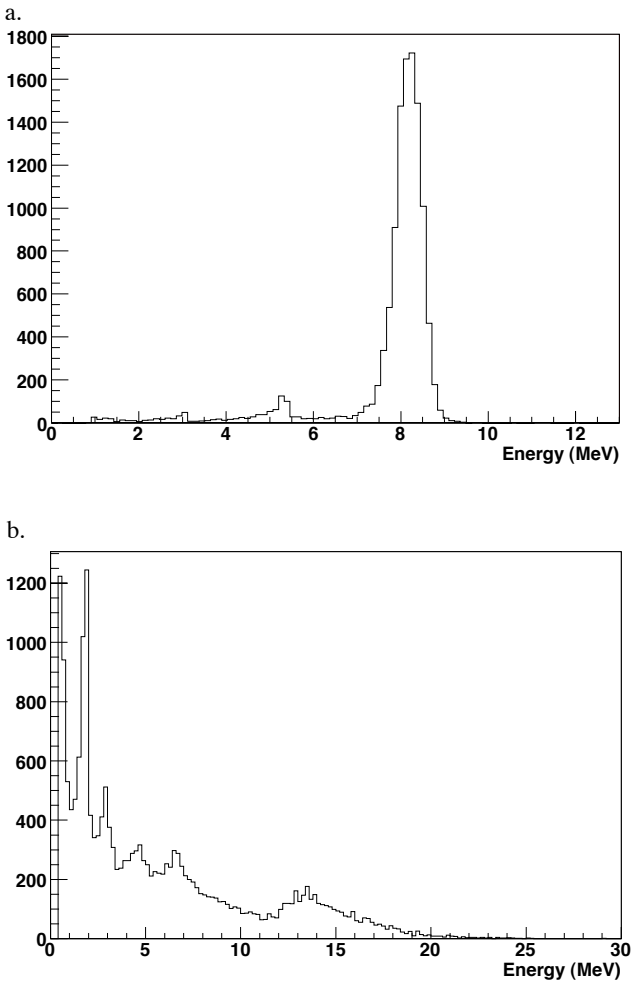

Fig. 112. a) Heavy-ion singles spectrum. b) BGO γ spectrum in coincidence with the 8 MeV ^{28}Si peak from spectrum a).

A detailed analysis of the experiment and in particular the study of the data at the two other energies (E_L = 20.71 and 21.18 MeV) is in progress.

Experiment 1024
^{40}Ca(α,γ)^{44}Ti for astrophysics
(C. Vockenhuber, TRIUMF)

The detection of ^{44}Ti ($t_{1/2}$ = 60.0 yr) through the 1.157 MeV γ-ray line by COMPTEL in supernova remnant Cas A has generated a great interest in ^{44}Ti. The light curves of relatively recent and nearby supernovae from the ^{44}Ti decay provide an observational test for nucleosynthesis models. Today, the measurement of ^{44}Ti from known and as yet unknown supernovae as well has high priority in the current γ-ray astronomy mission of INTEGRAL.

^{44}Ti is produced primarily in the α-rich freeze-out from nuclear statistical equilibrium, which takes place in the last stage of a supernova when at low densities α-particles are available for capture reactions on heavier nuclei. Since the reaction ^{40}Ca$(\alpha,\gamma)^{44}$Ti is the main process for the nucleosynthesis of ^{44}Ti this reaction has a strong influence on the final ^{44}Ti yield.

This reaction was studied partly in the 1970's by prompt γ-ray spectrometry in the energy range of E_α = 2.75–6 MeV, which corresponds to stellar temperatures of T_9 = 1.7–3.7, respectively ($T_9 = T/10^9$ K). A recent off-line measurement using accelerator mass spectrometry (AMS) for counting of ^{44}Ti atoms from a preceding ^{40}Ca irradiation of a He gas target showed a significantly larger production rate at wider temperature region $T_9 \sim$ 0.8–3 compared to the expected yield from prompt γ-ray spectrometry.

In order to get a better understanding of ^{44}Ti nucleosynthesis we are pursuing a detailed study of the reaction ^{40}Ca$(\alpha,\gamma)^{44}$Ti in inverse kinematics at astrophysically relevant energies with the recoil mass spectrometer DRAGON.

Ion source and beam contamination

The experiment requires a ^{40}Ca beam in the energy range of 0.5–1.2 MeV/u. ^{40}Ca beam is produced in the

off-line ion source OLIS. Because of the restrictions of the ISAC RFQ ($A/q < 30$), a charge state of 2+ or higher must be extracted by the ion source. Beam contamination is another concern since ^{40}Ar is a stable isobar to ^{40}Ca.

Our first approach was using the surface-hybrid ion source, loaded with pure calcium. Ca has a first ionization potential of 6.1 eV and can be easily ionized by surface ionization. Ar is not ionized at significant levels in a surface ion source because of its high first ionization potentials (15.8 eV). The second ionization potential of all elements is above 10 eV and thus multiple charge states are usually not observed with surface ion sources. However, the special design of the OLIS hybrid-surface ion source allows electron impact ionization as a second ionization step. This results in a significant production of 2+ charge states of ^{40}Ca. Furthermore, the significant electron current of about 100 μA screens and carries the 2+ ions through the retarding potential at the extraction electrode. This technique provides a clean $^{40}Ca^{2+}$ beam up to a few nA with negligible contamination of ^{40}Ar and other components (Fig. 113a).

In order to achieve higher beam currents, a microwave ion source was used. Clean He gas was used for the plasma which sputters Ca atoms from a large pure Ca metal target installed at the back of the ion source chamber. Up to several 100 nA could be produced with little contamination of ^{40}Ar (Fig. 113b). The large sputtering target allows an operation of several weeks without interruptions.

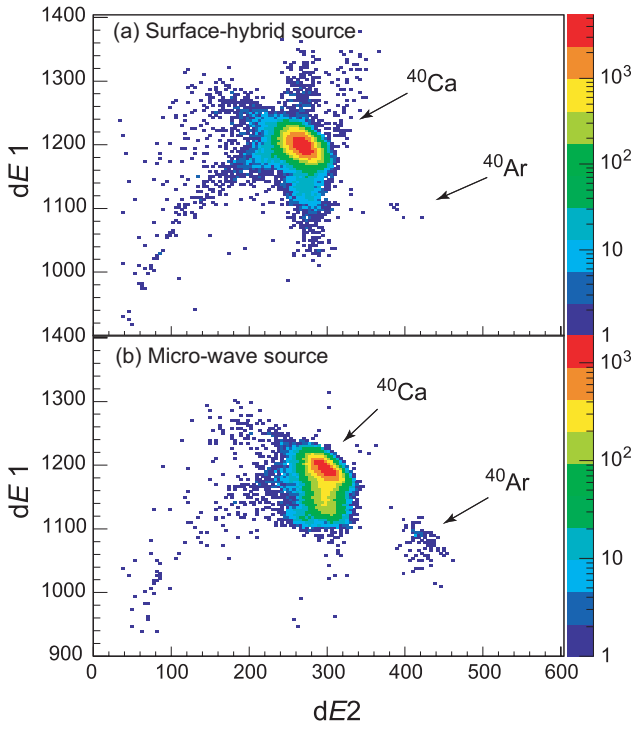

Fig. 113. Beam contamination from the ion sources. A ^{40}Ar/^{40}Ca ratio of 8×10^{-5} for the surface-hybrid source (a) and 5×10^{-3} for the microwave source (b) was measured using attenuated beam in the DRAGON ionization chamber ($dE1$ and $dE2$ are the two energy-loss signals from the segmented anode of the ion chamber).

Charge state distribution

This experiment also requires a special device to boost the charge states of the recoils to match the bending requirements of the recoil spectrometer. This device consists of a retractable foil, which we call the DRAGON charge state booster (CSB) and which is described in the DRAGON section of this Annual Report.

To determine the charge state distribution of ^{40}Ca we measured the current in a Faraday cup after the first bending magnet MD1, where charge states 11+ or higher can be bent. The final CSB set-up shifted the charge state distribution as expected without and with gas in the gas target (Fig. 114).

The CSB has several advantages: First, we can cover at least 2/3 of the charge state distribution of ^{44}Ti recoils. Second, we can avoid the unfavourable charge states 10+ and 11+, where the beam suppression of the recoil separator is reduced due to identical A/q values of beam and recoil. Third, for a given energy the recoils leave the CSB with the same charge state fraction no matter where the reaction occurs. Otherwise, with only the gas acting as a stripper, the charge state fraction depends strongly on the position where the reaction takes place because the equilibrium distribution is not reached at our pressures.

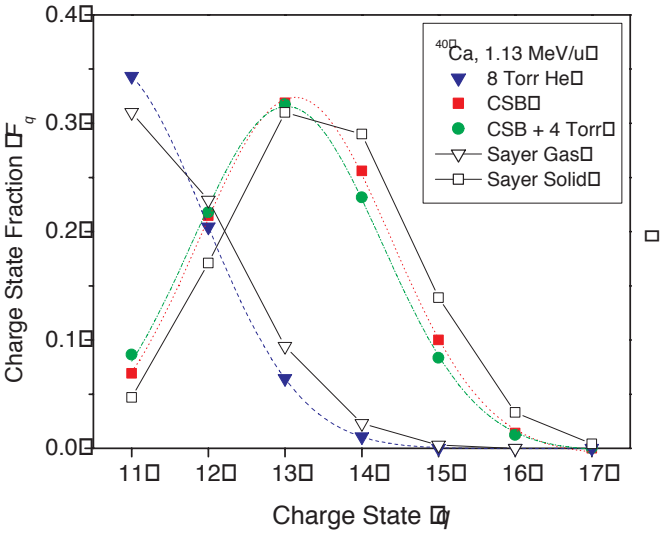

Fig. 114. Measured charge state distributions of ^{40}Ca at 1.13 MeV/u with and without He gas and charge state booster (CSB). A Gaussian was fitted to the measured data points. For comparison the expected values from the Sayer formula for gas and solid medium are also shown as open symbols.

^{44}Ti identification with an ionization chamber

Recoils are finally detected in the DRAGON ion chamber. It consists of an isobutane gas volume of 25 cm length separated from the upstream beam line with a thin entrance window (130 μg/cm^2 Mylar or grid supported 55 μg/cm^2 poly-propylene) of 50 mm diameter. In its volume ions lose energy according to their stopping power dE/dx, which depends on energy, mass and nuclear charge of the ions. The anode is segmented into two 10 cm sections and a 5 cm section at the end of the chamber ($dE1$ for the first segment and $dE2$ for the second segment). The total energy is measured as the sum of all segments with a resolution of 1.2% FWHM.

Figure 115 shows 2-dimensional spectra ($dE1$ vs. $dE2$) of singles and coincidences with the BGO detector of a typical run at the strong resonances. ^{44}Ti signals are clearly separated from the broad background of leaky ^{40}Ca. The ion chamber also provides identification of beam contamination (Fig. 114). Although ^{40}Ca and ^{40}Ar have the same energy, they are clearly separated in the $dE1$ vs. $dE2$ plot due to the difference in nuclear charge of 2.

^{44}Ti yield

In order to check the measurement capabilities of this reaction at DRAGON we started with the strong and well established resonances at $E_x \sim 9.2$ MeV. Resonance strengths and γ-ray decays of this isospin-mixed triplet were measured in detail by prompt γ-ray spectrometry. ^{44}Ti recoils were measured at several ion energies and target pressures to resolve the narrow structure. Due to the high yield, charge states 12+ to 16+ of ^{44}Ti could be measured. This allowed us to measure the charge state distribution of ^{44}Ti recoils and derive the absolute yield. Our preliminary value for the sum resonance strength of $\sum\omega\gamma = 7.7 \pm 0.7$ eV is in agreement with the prompt γ-ray data.

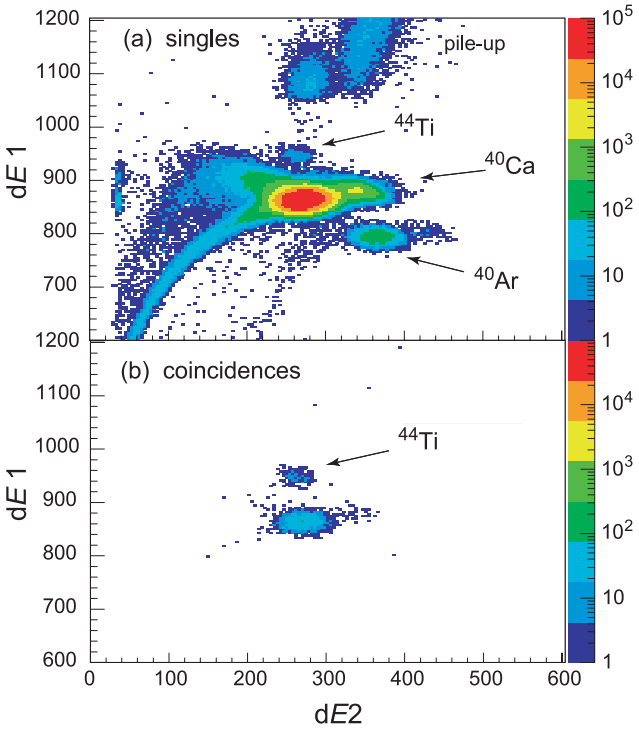

Fig. 115. 2-dimensional spectra ($dE1$ vs. $dE2$) of singles (a) and coincidences with the BGO detector (b) of a typical run at the strong resonances. The main peak in singles is leaky ^{40}Ca, which is reduced in the coincidence spectrum by more than 3 orders of magnitude.

The first part of the astrophysically interesting region from $E_x = 9.2$ MeV down to $E_x \sim 6.5$ MeV was covered in a longer run in November using around 50 different beam energies from 1.13 MeV/u down to 0.85 MeV/u. The analysis of the data is in progress.

Experiment 1027
Measurement of the ^{22}Na(p,γ) reaction rate
(J. Caggiano, TRIUMF)

Orbiting γ-ray observatories like the now decommissioned CGRO from the Comptel mission, and the recently launched INTEGRAL satellite have been used to detect unique γ-ray signatures from explosive events such as novae, supernovae, and γ-ray bursts. These data are unique because they are tied to one particular isotope, in contrast to other observations which can not distinguish between individual isotopes of a given element. By understanding the production of a particular radioisotope, the explosive process that created it can be further understood. This process requires accurate nuclear physics data so that astrophysical models may be refined and modified to explain the observed γ-ray fluxes detected at these telescopes.

It remains a mystery why, for example, no ^{22}Na characteristic γ-rays ($E_\gamma = 1.275$ MeV) have been observed in connection with specific, known explosions. Recently, a new level in the nucleus ^{23}Mg was identified at $E_x = 7.769$ MeV ($E_r = 189$ keV) and falls within the Gamow window for novae [Jenkins *et al.*, Phys. Rev. Lett. **92**, 031101 (2004)]. The existence of this level may help to explain the absence of the characteristic γ-rays in observational data. The spin and parity of the level, while not definitively identified in the experiment, were tentatively assigned to be $9/2^-$, corresponding to $L = 1$ proton capture in novae. Given estimates about the strength of this resonance ($\omega\gamma \leq 4$ meV), it could be the dominant contributor to the burning of ^{22}Na. Hence, the resonance strength needs to be measured.

We have initiated a project to measure the strength of this resonance (as well as the others within 1 MeV of the proton threshold) by taking advantage of the high intensity ^{22}Na beam available at TRIUMF's ISAC

to produce an implanted target of ^{22}Na. The project has many specific stages as follows: implanting stable ^{23}Na into a variety of carefully chosen candidate substrate materials, characterizing the implanted targets using a strong proton resonance, producing the ^{22}Na targets/sources, and finally carrying out the (p,γ) measurement.

In February, several metal foils were loaded with (stable) ^{23}Na at doses ranging from 0.2 to 2.0 mCi-equivalent ^{22}Na. The implantations were done at energies of 30, 40, and 50 keV, corresponding to energies available at ISAC. Implantation was executed in the low energy part of the ISAC experimental hall at the 8π target position. In order to produce uniformly-distributed layers of ^{23}Na, beam rastering was used with a 5 mm diameter circular collimator placed just upstream of the target. By adjusting the parameters of the rastering program, a uniform distribution with sharp edges was obtained.

In April, the three dimensional profile of some of these implanted targets was characterized. The profiles were measured using a strong resonance in the ^{23}Na(p,γ) reaction at 309 keV. The depth profile was measured by changing the beam energy by small $\sim$2 keV/u steps. A beam of singly-charged, molecular H_3 was delivered from ISAC to the DRAGON target position and BGO rates of known γ-rays were used to determine the resonance profile. Beam currents of up to 1 particle-microampere were delivered to the target. The beam was collimated using a 1 mm diameter circular collimator. A two-dimensional translational motion stage was built to move the target in the directions perpendicular to the beam and thereby measure the lateral profile.

In June, a new target lid for the ISAC collection station was fabricated and installed for the purposes of collecting the ^{22}Na at TRIUMF. A coil of LN_2-cooled copper tubing was installed just upstream of the target to suppress carbon buildup on the substrates during collection (and also to prevent migration of scattered ^{22}Na upstream). A 5 mm diameter circular collimator was installed $\sim$5 mm upstream of the substrate (target) ladder to limit the beam spot size on the targets. Following installation, one small ($\approx$10 μCi) target was fabricated in July.

In October/November, a beam of 25 p nA of ^{22}Na was used to make two target-quality sources: 300 μCi and 185 μCi. These targets will be used for testing detection apparatus and for the actual measurement, while the weakest target will be used for testing purposes only.

The targets are to be transported to the Nuclear Physics Laboratory at the Univ. of Washington for executing the ^{22}Na(p,γ) reaction rate measurement.

Experiment 1030
Charged-particle channels in the β-decay of ^{11}Li
(R. Raabe, Katholieke Univ. Leuven)

The ground state of the ^{11}Li nucleus is the best example of the two-neutron halo state. Its structure has been mostly studied with nuclear reaction methods, giving results which are somehow model-dependent. The β-decay process, on the other hand, has the advantage of being well understood: valuable information can be extracted from the nature and branching ratios of the various decay channels. We decided to study the β-decay of ^{11}Li, with particular attention to the channels proceeding through high-lying resonances in ^{11}Be, which are characterized by the emission of charged particles. One channel, $^{11}\mathrm{Li}\xrightarrow{\beta}{}^{9}\mathrm{Li}+d$, can also occur by direct decay into the ^{9}Li$+d$ continuum; its branching ratio gives the overlap between the mother and daughter state wave functions. Our aim was to identify this channel by separating it from the ^{8}Li$+t$ channel, then measure their branching ratios and the spectra of the emitted particles.

The measurement took place at TRIUMF in April. We used a novel technique by implanting the ^{11}Li nuclei directly into a finely segmented silicon detector and observing the decay events. The detector has more than 2300 pixels, 300×300 μm^2 each, and it is 78 μm thick. The high segmentation allows β particles to escape from the pixel where they are emitted, depositing very little energy; on the other hand, the heavier charged particles are almost always stopped within one pixel. This strongly reduces the importance of the β-particles background. This, and low-noise electronics equipment, allowed us to measure particles to a very low energy (less than 200 keV). Further advantages with respect to previous techniques are the very large efficiency (in principle 100%, with the limitation of the acquisition dead time), a very reliable normalization for the measured branching ratios, and access to the "decay history" of each implanted nucleus (often, daughters are also radioactive and their decay can be correlated).

To achieve the desired implantation depth into silicon, radioactive nuclei have to be accelerated to an energy of some MeV. For this purpose, a ^{11}Li beam was for the first time accelerated at ISAC, to the TUDA beam line where our set-up was placed. Beams of ^{8}Li and ^{9}Li were also used to measure in detail the energy spectrum of the particles emitted in each case. For all beams, the energy was the maximum delivered by ISAC (1.5 MeV/nucleon), which allowed implanting the nuclei halfway into the detector. Further details on the beam characteristics are given in Table XIV. Notice that we never used the full beam intensity that ISAC could provide: with ^{11}Li we wanted

Table XIV. Characteristics of the beams used in this measurement. To protect the detection set-up we did not use the maximum intensity that ISAC could provide.

Beam	On/off (s)	Irradiation time (hours)	Total charge (impl. nuclei)
^{8}Li	2.5–2.5	13.9	10.1×10^6
^{9}Li	0.5–0.5	12.6	17.8×10^6
^{11}Li	20.0–20.0	28.2	9.0×10^6
^{11}Li	continuous	133.1	68.3×10^6

to allow sufficient time between successive implantations in the same pixel for all daughters to decay; with ^{9}Li and ^{8}Li we needed to limit the possible damage on the detector. In some cases, in addition, implantation periods (beam-on) were alternated with decay periods (beam-off) in order to have a signature of the half-life. This was achieved by using the beam "kicker" at the entrance of the beam into the ISAC hall. A uniform implantation profile on the whole detector surface (16×16 mm^2) was obtained by de-focusing the beams using the quadrupoles on the TUDA beam line.

^{8}Li The ^{8}Li nucleus has a half-life $T_{1/2} = 838$ ms. It decays into ^{8}Be ($Q_\beta = 13.6$ MeV) with a 100% branching to the $J^\pi = 2^+$ first excited state; this is a large resonance ($E^* = 3$ MeV, $\Gamma = 1.5$ MeV) that immediately decays into two α particles. In our detector we measure the full energy of both αs. The spectrum is shown in Fig. 116 for all the beam-off (pure decay) events. Its importance lies in the information that we can deduce from it about the shape and exact position of the 2^+ state in ^{8}Be, which is still debated in literature. The shape of the resonance is used to determine the actual neutrino spectrum from the decay of ^{8}B, a crucial quantity in experiments measuring the neutrino flux coming from the sun. This is the first time that the 2α spectrum from ^{8}Li is measured with our "calorimetric" method, and Fig. 116 shows how results differ from a previous measurement where only one α particle was detected. In our measurement, only negligible corrections are expected from the β-particle energy pile-up; the evaluation will eventually include a detailed simulation of the measurement.

^{9}Li The half-life of ^{9}Li is $T_{1/2} = 178.3$ ms. It decays into ^{9}Be with a 50% branching to the ground state (stable, $Q_\beta = 13.6$ MeV), and the remaining 50% to resonances immediately decaying into two α particles and a neutron. Due to the complex decay pattern, and the fact that the neutron is not detected, the energy deposited by the two α particles is not easily predictable. Since this is an important parameter in our analysis for the identification of the channels in the ^{11}Li decay, we decided to measure it directly by implanting ^{9}Li nuclei in our detector. The energy spectrum of decay

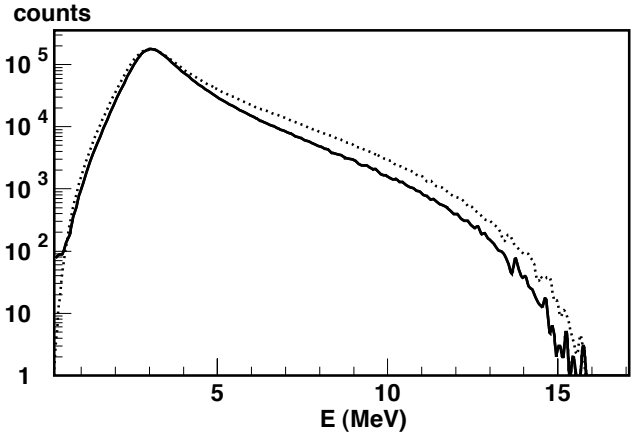

Fig. 116. Energy spectrum of events from the decay of ^{8}Li. Solid line: this measurement (3.3×10^6 events); dotted line: from Phys. Rev. Lett. **26**, 1127 (1971).

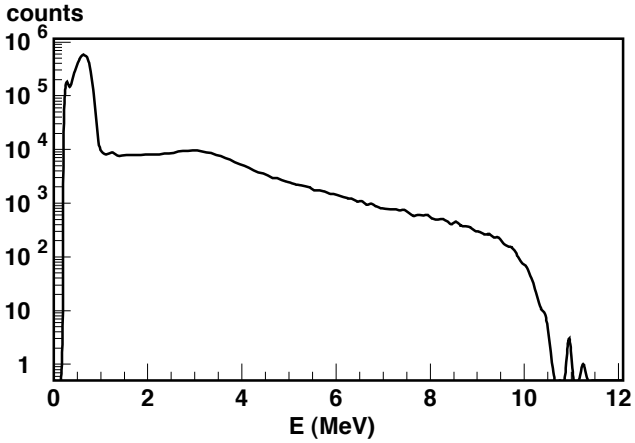

Fig. 117. Energy spectrum of events from the decay of ^{9}Li (2.7×10^6 events).

events is shown in Fig. 117. The total branching ratio into excited states, obtained comparing the number of decays with the total number of implanted nuclei, is 48.2% (preliminary), in agreement with the literature value (49%). The peak at $E \sim 0.65$ MeV is due to α particles, while the β-background is hardly visible (a cut-off at 200 keV is applied).

^{11}Li The half-life of ^{11}Li is $T_{1/2} = (8.5 \pm 0.2)$ ms. The β-decay proceeds to states in ^{11}Be ($Q_\beta = 20.68$ MeV). Several particle-emission channels are open and have been observed in the past. Some of the daughter nuclei are in turn unstable and can emit charged particles, like ^{8}Li, ^{9}Li and ^{11}Be. In order to disentangle the contribution from the latter nucleus ($T_{1/2}(^{11}\text{Be}) = 13.8$ s) we performed runs with an implantation-decay cycle of 20–20 s. The energy spectrum of events detected during the beam-off period of these runs is shown in Fig. 118. The peaks at $E = 1.19$ MeV and $E = 0.71$ MeV are due to the $^{11}\text{Be} \xrightarrow{\beta} {}^{7}\text{Li}+\alpha$ channels, where the ^{7}Li can be produced in its ground state or in its $E^* = 477.6$ keV excited state. The ratio between the number of decays

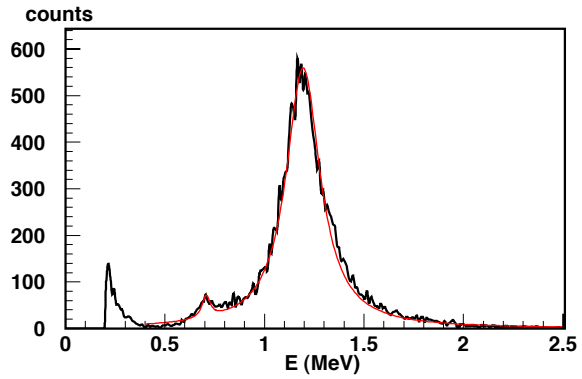

Fig. 118. Energy spectrum of events recorded during the beam-off period following the implantation of ^{11}Li (19200 events). The time cycle (20 s on – 20 s off) was chosen so as to enhance the events from decay of ^{11}Be. The line is a double-Lorentzian fit of the peaks corresponding to the decay of ^{11}Be into ^{7}Li(g.s.)+α and ^{7}Li*(478 keV)+α.

detected in these two channels does not agree with the branching ratios reported in literature. The evaluation is still in progress.

For the actual measurement of the ^{11}Li, we implanted the nuclei *continuously* in the detector, keeping the rate sufficiently low so as to follow, for each implanted nucleus, its decay and that of its daughters. Identification of the various channels is based on the identification of the daughter decays via a) the energy spectra of the emitted particles and b) the half-life of the daughter channels. For some channels, the daughter is either stable or decays via pure β-emission, and is therefore not detected. However, for the channels of most interest to us (^{9}Li+d and ^{8}Li+t) this method is valid: the daughter nuclei emit charged particles and their spectrum is very different, as proved by the direct measurements shown in Figs. 116 and 117.

Events from the decay of ^{11}Li follow an implantation within a short time. By applying this selection, the energy spectrum in Fig. 119 is obtained (the inset shows the time behaviour of all events following an implantation). The peaks in the spectrum are explained by decays into n-unbound states in ^{11}Be: after a neutron is shaken off, the remaining ^{10}Be is in narrow resonances states that break up into ^{6}He+^{4}He. From the analysis of the peaks it will be possible to extract information on the states and the branching ratios.

The energy spectrum of daughter-decay events is shown in Fig. 120. The channels emitting charged particles are strongly selected. The peak at low energy is attributed to the decay of ^{9}Li from the deuteron-emission channel of the ^{11}Li β-decay. Further analysis is necessary to reduce the contribution from background channels. Additional evidence will also be provided by the time behaviour of the different groups of events visible in Fig. 120. For this purpose, analysis on the full statistics is in progress.

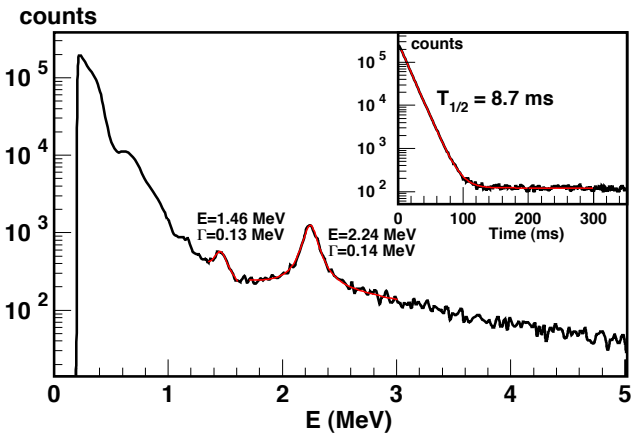

Fig. 119. Energy spectrum of decay events from ^{11}Li, obtained selecting events following implantations within 40 ms. The inset shows the time behaviour of all decay events: the ^{11}Li decay gives the short half-life component. Events in this figure are only 10% of the full statistics.

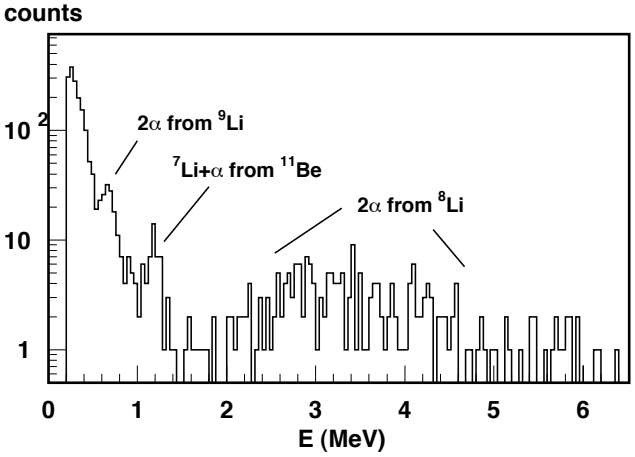

Fig. 120. Energy spectrum of daughter-decay events after the decay of ^{11}Li. The channels emitting charged particles are strongly selected (events in this figure are only 10% of the full statistics).

Experiment 1031
Charged particle exit channels from the ^{12}C+^{12}C fusion reaction at astrophysical energies

(A.M. Laird, York; M. Aliotta, Edinburgh)

Motivation

The ^{12}C + ^{12}C fusion reaction is important in explosive carbon burning in type 1a supernovae as well as in hydrostatic burning during standard stellar evolution. At the temperatures relevant in both scenarios, (0.8–1.2 $\times$ 10^{9} K), the reactions ^{12}C(^{12}C,p)^{23}Na and ^{12}C(^{12}C,α)^{20}Ne dominate, resulting in the main products of carbon burning being ^{20}Ne and ^{24}Mg (from ^{23}Na(p,γ) and ^{20}Ne(α,γ)).

Consequently, not only is the ^{12}C + ^{12}C fusion rate important for describing stellar evolution subsequent to helium burning, but it also dominates the ignition

of thermonuclear runaway leading to type 1a supernovae. Therefore, measurements which yield information on the astrophysical S-factor at temperatures between 0.8–1.2 $\times$ 10^9 K, corresponding to a centre of mass energy range of 1 to 3 MeV, are highly important.

Experiment

In July, TUDA performed an initial experimental run to test the method by measuring an energy region covered by existing data.

A 3^+ ^{12}C beam was provided by OLIS with a maximum intensity of around 70 e.nA. The beam energy was varied between 670 keV/u ($E_{\rm cm}$ = 4.02 MeV) and 610 keV/u ($E_{\rm cm}$ = 3.66 MeV) in 20 keV/u steps. Before and after each energy change, the beam energy was measured using DRAGON to determine the beam energy with high accuracy and to ensure that the beam energy had not drifted during the course of a run. This is extremely important due to the sensitivity of the cross section to the centre of mass energy. Enriched carbon targets of thickness 20 μg/cm^2 were used. Figure 121 shows a schematic of the experimental set-up which comprised two LEDA-type silicon strip detectors (1000 μm and 300 μm thickness) and two S2-type detectors (500 μm). The forward detector arrays were protected from elastic scattering by aluminum foil with the exception of the monitor detector. One LEDA detector was offset upstream to cover the angular region around 45°. This detector had five 1 mm holes in the shield, at each of five angles, to provide elastic scattering data around 45° for normalization purposes.

During the run, it was discovered that the intensity of the beam produced such a high flux of electrons from the target that, despite the aluminum shielding, charge built up on the detector arrays resulting in an increase in leakage current of more than an order of magnitude. Further investigation into this problem showed that positively biasing the shields overcame this problem and this information will be incorporated into the designs of future runs.

Figure 122 presents an on-line spectrum from one strip of the forward LEDA detector corresponding to a laboratory angle of 19°. Several peaks can be seen arising from reaction protons and alphas. The peak observed at approximately 3 MeV is due to elastically scattered deuterons from water contamination of the

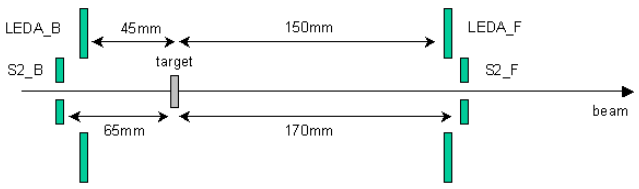

Fig. 121. Schematic of experimental set-up.

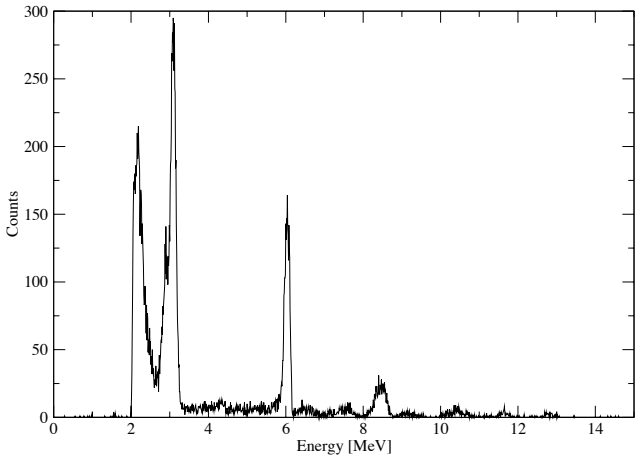

Fig. 122. On-line energy spectrum.

target foil. The sharp cutoff at about 2 MeV is a result of a hardware threshold imposed to remove elastic protons. Analysis of the data is ongoing and further experimental runs are planned for 2006.

Experiment 1070
Upgrade of ^{38m}K β-ν correlation
(J.A. Behr, M.R. Pearson, TRIUMF; K.P. Jackson, TRIUMF/SFU)

The TRIUMF neutral atom trap collaboration has pioneered the direct measurement of β^+-ν angular distributions by measuring the momentum of the few 100 eV energy recoiling nucleus in coincidence with the positron.

We have published the best measurement of a pure Fermi β-ν correlation parameter a = 0.9981 $\pm$ 0.0030 $\pm$ 0.0037 [Gorelov, Phys. Rev. Lett. **94**, 142501 (2005)] in agreement with the standard model prediction a = 1. These are the best limits on general scalar interactions coupling to the first generation of particles. In December the TRIUMF EEC approved our proposal to improve the overall accuracy of this β-ν correlation experiment by a factor of 3. We also would extend it to lower β energy to improve sensitivity to the scalar-vector Fierz interference term and hence gain linear sensitivity to certain types of scalars, reaching accuracy directly competitive with the Q-value dependence of $0^+ \rightarrow 0^+$ ft values.

ISAC has demonstrated ^{38m}K yields 5 times greater than those for the published experiment, and we have also improved our collection efficiency by 3 times by adding another ring laser. Most of our systematic errors are given by statistically limited fits of different aspects of the data *in situ*. We have the best experiment and have good ideas on what to fix and upgrade to make it considerably better.

Theory corrections are small

A very attractive aspect of the scalar search described here is that it is free of nuclear structure-dependent corrections to another order of magnitude sensitivity. The ^{38m}K decay is one of the well-characterized superallowed $0^+ \rightarrow 0^+$ decays (see Fig. 123). The branch to the excited state is known to decay cleanly to the ground state, with experimental limits on excited-state branches of $<2 \times 10^{-5}$ [Hagberg, Phys. Rev. Lett. **73**, 396 (1994)]. The recoil-order corrections to the allowed approximation are small, $<3\times10^{-4}$, and are calculable without nuclear matrix elements [Holstein, Rev. Mod. Phys. **46**, 789 (1974)]. Radiative corrections, mostly due to the distortion of the momenta by bremsstrahlung production of real photons, are at 0.2% level but can be calculated to accuracy an order of magnitude better, and we include this in our Monte Carlo with assistance from F. Glück [Comp. Phys. Comm. **101**, (1997) 223; *ibid.*, Nucl. Phys. **A628**, 493 (1998)]. Corrections

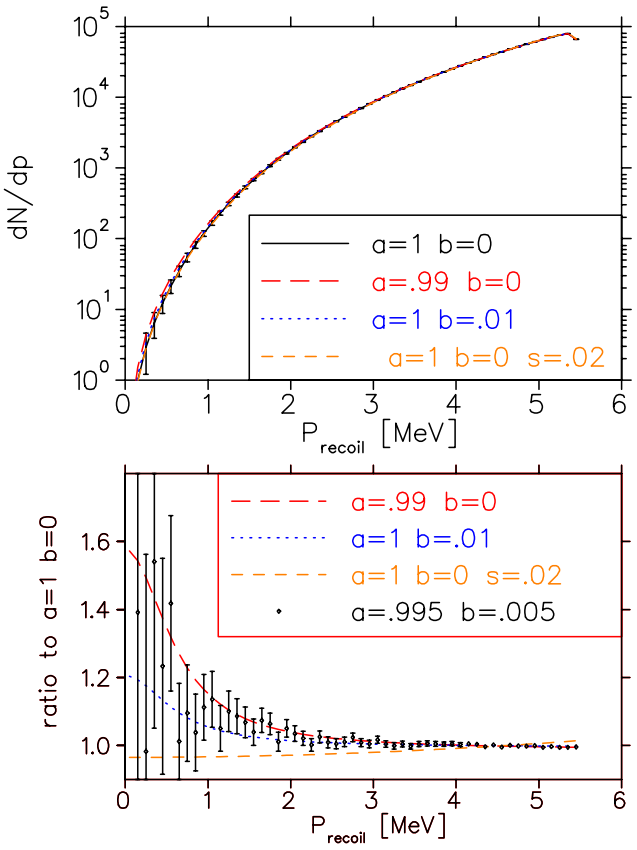

Fig. 123. Analytical simulation of the recoil momentum spectrum, which we would measure with atomic e^--recoil coincidences. The bottom figure shows the dependence on a and b. Although a and b are well-correlated, either one can be separated from the data simultaneously while allowing the shakeoff e^- dependence on recoil momentum to float. To reach statistical error 0.001 in b, with sensitivity to a window left open by $\pi \rightarrow e\nu$ decay, would require 10 shifts.

with some model dependence, such as the order q^2 term in the expansion of the vector form factor [Kleppinger, Nucl. Phys. **A293**, 46 (1977)], begin to enter at $< 2 \times 10^{-4}$.

Theory

The dependence on four-fermi coupling constants is given in Jackson, Nucl. Phys. **4**, 206 (1957). There is sensitivity to imaginary (time-reversal-violating) terms that is very interesting, but it is nevertheless instructive to show the simple expression assuming the constants are real, and setting $C'_V = C_V = 1$ (no vector current coupling to right-handed ν):

$$\begin{aligned} a &\approx 1 - (|C_S|^2 + |C'_S|^2) \\ b &\approx -\sqrt{1-(\alpha Z)^2}\, Re(C_S + C'_S)\,. \end{aligned}$$

The Hamiltonian can be rearranged as [Herczeg, Prog. Part. Nucl. Phys. **46/2**]:

$$\begin{aligned} H_S &= [(C_S + C'_S)\bar{e}(1-\gamma_5)\nu_e^{(L)} \\ &\quad + (C_S - C'_S)\bar{e}(1+\gamma_5)\nu_e^{(R)}]\bar{u}d, \end{aligned}$$

making it clearer that the coupling combination $C_S + C'_S$, which is constrained by b, couples to standard model left-handed ν's. The combination $C_S - C'_S$ describes scalars coupling to right-handed ν's and must be constrained by a.

Our present experiment, Expt. 715, places limits on scalar bosons with mass/coupling ratios ∼3 times the mass of the W. That makes it complementary to the limits on the Fierz interference term b, and to strong indirect limits on many types of scalar couplings from higher-order corrections to $\pi \rightarrow e\nu$ decay in an effective field theory analysis [Campbell, Nucl. Phys. **B709**, 419 (2005)].

Although the coupling of the scalars in many standard model extensions scale with the fermion masses, "...this is partially maintained in the MSSM and simple two Higgs doublet models, but usually not in more complicated Higgs models" [Langacker, Czech. J. Phys. **55**, A1 (2005)]. The best general limits on first generation scalar interactions still come from nuclear β decay [Herczeg, *op. cit.*].

Fierz term b In addition to improving the measurement of a, we will extend the measurements to lower E_β to gain sensitivity to the Fierz interference term b, with a goal of achieving competitive accuracy to the Q-value dependence of the world average of $0^+ \rightarrow 0^+$ ft values, $b_F = 0.0024(28)$ [Savard, Phys. Rev. Lett. **95**, 102501 (2005)]. Previous direct experiments have attempted this by measuring the detailed β energy spectrum. Our technique would measure the angular distribution as a function of β energy, which has much

less dependence on detector E_β response. The present Savard *et al.* result, incorporating new advances in mass measurements, moved the Fierz centroid by 1 σ while roughly preserving the error. Our present statistical error on the Fierz term is about 4 times larger, and our upgraded experiment would approach their sensitivity.

We analyzed data taken in October, 2000 in two ways:

• Method I) fitting the experimental time-of-flight spectra of the recoils as a function of β energy. At fixed E_β, the TOF of the recoil is monotonic with the ν angle of emission. Separating into E_β bins avoids overlapping all of these effective ν angle spectra and diluting sensitivity.

• Method II) Reconstructing the β-ν angle from the position and energy information in both detectors. This method gives a consistent result. This method has great power to simultaneously extract certain systematic physics errors.

Possible systematic effects from physics

Recoil energy-dependent e^- shakeoff A potential systematic physics error for our method is that the final charge state of the recoiling atom should have a small but nonzero dependence on its velocity. This effect will distort the recoil energy spectrum by (1+s E_{recoil}/E_{max}) in a simple argument based only on the sudden approximation [Carlson, Phys. Rev. **129**, 2220 (1963)] independent of the details of the atomic physics calculation. With this parametrization, the shakeoff effect can be fit simultaneously with the a and b parameters. We have done this using both methods I and II, finding an effect consistent with zero and with upper limit [Gorelov, *op. cit.*; Behr, Eur. Phys. J. A (2005) "online first" DOI: 10.1140/epjad/i2005-06-097-9] consistent with a rough estimate from Berkeley [Scielzo, Phys. Rev. **A68**, 0222716 (2003)]. The correction is small and statistics-limited in its determination. The best ^{6}He β-ν experiment [Johnson, Phys. Rev. **132**, 1149 (1963)] succeeded in extracting this effect while only measuring the recoil momentum spectra as a function of charge state. We also expect to be able to do this in atomic e^--recoil coincidence measurements.

Dependence on atomic density Berkeley has seen evidence for a systematic change in a with density of ^{21}Na atoms in the MOT [Scielzo, Phys. Rev. Lett. **93**, 102501 (2004)]. Their suggested plausible mechanism involves the formation of molecular dimers from photoassociation. The rate of molecule formation r_{mol} would scale linearly with density. We run at $\sim$1/500 the density. The probability for an atom to form a dimer before decaying will be proportional to r_{mol}/r_{decay}, and the ratio of decay rates is an additional 1/20. So for the simplest scalings, we expect to be down by 10^{-4} in this effect. Nevertheless, the e^--recoil coincidence would provide a high-statistics method for us to test this for the upgraded experiment.

Proposed upgrade

Most of the systematic errors are determined by statistics-limited data evaluation. One example: the charge state of the recoil can depend on its momentum by shaking off different numbers of e^-s. We constrain this effect by simultaneously fitting it and a to our angular distribution reconstruction of Ar^{+1}. The projected statistics would allow us to fit other charge states +2 and +3 as well, achieving powerful redundancy of the model and making the systematic error smaller. Several other errors can be projected to improve with statistics.

An upgraded experiment would also include:

1. A larger MCP to reduce an error from the apparatus acceptance of 65% of the Ar^{+1} recoils (see Gorelov [*op. cit.*] for details of our published systematic errors). This error folds indirectly into the electric field and trap position errors.
2. A permanent mask installed on the MCP to monitor any position distortions from resistive anode nonlinearities. This is important for analysis method II, which we expect to be critical at lower E_β.
3. Better low-energy β singles calibration using interwoven ^{37}K trap measurements. At present our ability to determine the Fierz term is compromised by a relatively poor understanding of our singles E_β spectrum (from which we get our energy calibration) below 2 MeV. There is a 2.17 MeV γ-ray from the ground state of ^{38}K, and it appears there is a very small contribution of 2.7 MeV endpoint βs from ^{38}K g.s. that diffuses into the detection chamber. These together produce a 10% distortion of the singles E_β spectrum. We have shown in the past that ^{37}K does not suffer from this effect.
4. Measurement of the recoil momentum spectrum free of the β energy detection problems via a coincidence between atomic shakeoff e^-s and recoils to determine their TOF. We are in the process of experimentally testing this technique and expect it to have substantially reduced systematic errors, but stronger correlations between a and b.

e^--recoil coincidence method We show the sensitivity of the recoil momentum spectrum to these effects in Fig. 123. We also show the sensitivity to the recoil momentum dependence of the shakeoff electron probability and the ability to fit those simultaneously. See

the Expt. 956 report for more details on the electron detector.

This technique has been demonstrated by our competitors in Berkeley [Scielzo, Nucl. Phys. **A746**, 677c (2004)]. The resulting recoil TOF spectra will not be systematically dependent on the β energy. Depending on the efficiency we achieve in e^- detection, our coincidence rate will be 10 to 50 times greater. We have investigated systematic errors in a ^{80}Rb experiment in December (see the Expt. 956 report). We expect considerable discrimination of e^- signal from a small β^+ background by MCP pulse-height. If this method becomes viable for use in ^{38m}K decay, we could achieve statistical errors of ≈0.001 on the Fierz term in 10 shifts, halving the world error and making us sensitive to a window in parameter space left open for slepton exchange [Herczeg, Phys. Rev. **D52**, 3949 (1995)].

LANSCE Experiment NPDGamma
Measurement of the parity-violating gamma asymmetry A_γ in the capture of polarized cold neutrons by para-hydrogen, $\vec{n} + p \rightarrow d + \gamma$.

(S.A. Page, W.D. Ramsay, Manitoba)

Since the last Annual Report, the $\vec{n} + p \rightarrow d + \gamma$ collaboration has made several improvements based on results of the recent commissioning run and has taken a considerable amount of data without the liquid hydrogen target. During late 2004 and early 2005, we made A_γ measurements on a variety of nuclear targets and continued off-line testing of the liquid hydrogen target in preparation for data taking in 2006.

The solid-target running was particularly successful, with the $\vec{n} + p \rightarrow d + \gamma$ equipment performing at levels close to or exceeding our specifications. We have already published several papers, both in refereed journals and conference proceedings, and the data will form the basis of two theses.

In October, 2004, the experiment was the subject of a DOE technical review. In the written report, received in March, 2005, the committee re-affirmed the scientific merit of the experiment and was pleased with the technical progress. Some suggestions for improvement were made in the areas of administration and scheduling. In response to these recommendations, we have appointed a Run Plan Coordinator, a Shift Coordinator and an Experiment Coordinator. We have also updated the installation schedule. The liquid hydrogen target is now the critical item and has been assigned the highest priority, higher than any physics measurements using the beam.

The hydrogen vent line to the FP-12 cave in ER2 was completed in August and we expect that the liquid hydrogen target will be installed in the cave and commissioned in early 2006. Data-taking to a statistical precision of 10^{-7} (in A_γ) should occur at LANSCE during 2006. We then plan to move the experiment to the Spallation Neutron Source (SNS) in 2007, with data-taking to 10^{-8} statistical precision starting in 2008.

Background

The experiment is designed to measure the very slight, parity-violating, up-down asymmetry, A_γ, in the capture of vertically polarized cold neutrons on liquid parahydrogen. A measurement of A_γ provides a very clean measure of the weak pion nucleon coupling, f_π^1. In fact, to a very good approximation, $A_\gamma = -0.11 f_\pi^1$. The value of f_π^1 is somewhat controversial. The circular polarization of 1081 keV γ-rays from ^{18}F gives zero, implying $f_\pi^1 = (0 \pm 1) \times 10^{-7}$ [Haxton *et al.*, Phys. Rev. Lett. **86**, 5247 (2001)]. The ^{133}Cs anapole moment, on the other hand, gives a non-zero value, indicating $f_\pi^1 = (7 \pm 3) \times 10^{-7}$ [Flambaum and Murray, Phys. Rev. **C56**, 1641 (1997)]. Because it is based on a simple two-nucleon system without the complex many-body dynamics of the ^{18}F and ^{133}Cs experiments, NPDGamma has a good chance of laying the controversy to rest. The original goal of the experiment, as indicated in Fig. 124, was to measure f_π^1 to $\pm$ 0.5 $\times$ 10^{-7}, which is approximately 1/10 of the mid-range theoretical estimates, and corresponds to a precision of $\pm$ 0.5 $\times$ 10^{-8} in A_γ. We planned to do this at LANSCE, but the beam intensity and moderator brightness are each approximately half what was expected, and interference from a neighbouring flight path has reduced the possible running time per year by one-half. As a result, the collaboration now plans to run at LANSCE in 2006, demonstrate that all

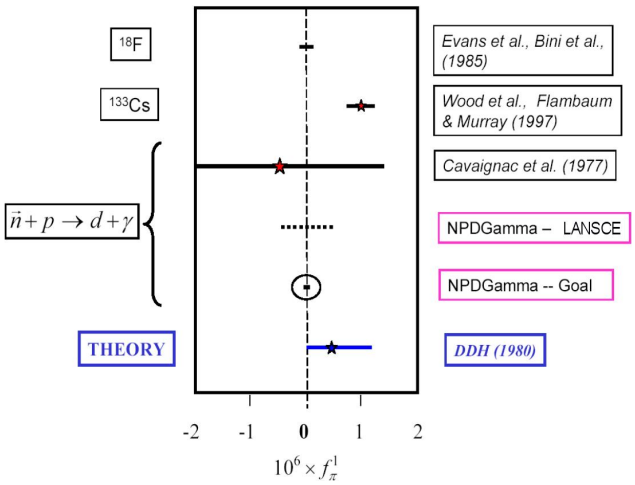

Fig. 124. Experimental and theoretical limits on the weak pion-nucleon coupling f_π^1. The expected precision of the upcoming 2006 run of the NPDGamma experiment at LANSCE is shown, as is the statistics-limited final result planned for the experiment at the Spallation Neutron Source (SNS). The experiment is expected to move to the SNS in 2007 and run in 2008.

the equipment works as expected and that systematic errors are under control, then move the experiment to the Spallation Neutron Source (SNS) at Oak Ridge. Once the apparatus is commissioned at the SNS, it should be possible to measure A_γ to a statistical precision of $\pm 1 \times 10^{-8}$ in 4000 hours at the design power of 1.4 MW.

The major pieces of equipment are shown in Fig. 125. A 20 Hz pulsed beam of cold neutrons is transported to the experiment through an $m = 3$ (critical angle for total reflection a factor of three greater than Ni) supermirror neutron guide. The neutrons are polarized by the ^{3}He spin filter in a uniform 10 G guide field, which is constant over the entire experiment. Vertically polarized neutrons are captured in the liquid hydrogen target with the emission of 2.2 MeV γ-rays. The target runs at 17 K with an equilibrium composition of 99.8% para-hydrogen to prevent spin flip scattering and the consequent neutron depolarization which would occur with ortho-hydrogen. To reduce systematic error, the rf spin flipper reverses the neutron spins at the 20 Hz neutron frame rate. Capture gammas are detected in an array of 48 CsI(Tl) crystals. The three beam monitors, which were provided by the Manitoba group, are used to determine the neutron polarization and to monitor the para/ortho hydrogen ratio in the target.

Liquid hydrogen target

The target will contain 16 l of liquid para-hydrogen which will absorb about 60% of the neutron beam. During the summer, we conducted off-line tests of the target. Figure 126 shows the target installed in a test shed at the Lujan Center. In accordance with safety regulations, the target must not be installed in the FP-12 cave until the hydrogen vent lines are in place and the target has passed all the appropriate safety reviews. The vent lines to the cave were completed in August and we expect that the target will be operational in FP-12 in early 2006.

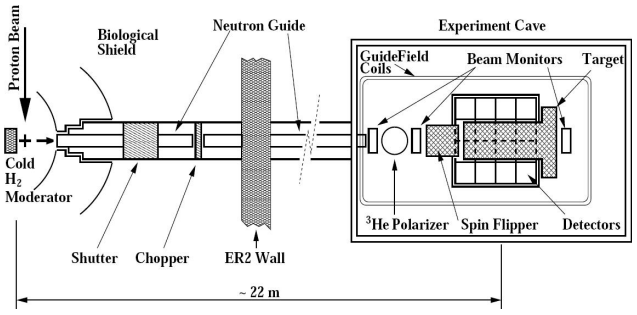

Fig. 125. Bird's eye view of the apparatus used to measure A_γ in $\vec{n} + p \to d + \gamma$ on FP-12 at LANSCE.

Fig. 126. Liquid hydrogen target undergoing off-line tests in the test shed. The target is expected to be installed in the FP-12 cave early in 2006.

Nuclear target measurements

A very productive part of the 2005 run period was the measurement of γ-ray asymmetries for a variety of nuclear targets. Preliminary results from the 2005 run are listed in Table XV. We chose target materials which either have large capture cross sections or which form part of the liquid hydrogen target and hence contribute a background during the actual run. Measurements on target materials are important, as the results of such measurements make it possible for us to estimate the contamination of our $n + p \to d + \gamma$ signal by capture on materials other than hydrogen. The chlorine runs are important because a well-known, large asymmetry exists that provides a useful test of our equipment. The chlorine runs prove that a non-zero asymmetry can be measured, and also confirm the $\cos\theta$ dependence of A_γ as shown in Fig. 127.

Table XV. Preliminary results for parity violating asymmetries from the 2005 run. The errors are statistical only.

Target	A_γ
In	$(-6.8 \pm 3.0) \times 10^{-7}$
Mn	$(5.3 \pm 7.8) \times 10^{-7}$
Sc	$(-7.0 \pm 2.8) \times 10^{-7}$
Co	$(6.1 \pm 3.1) \times 10^{-7}$
Ti	$(7.1 \pm 4.0) \times 10^{-7}$
Al	$(-0.02 \pm 3) \times 10^{-7}$
Cl	$(-21 \pm 1.6) \times 10^{-7}$
V	$(-2.42 \pm 4.5) \times 10^{-7}$

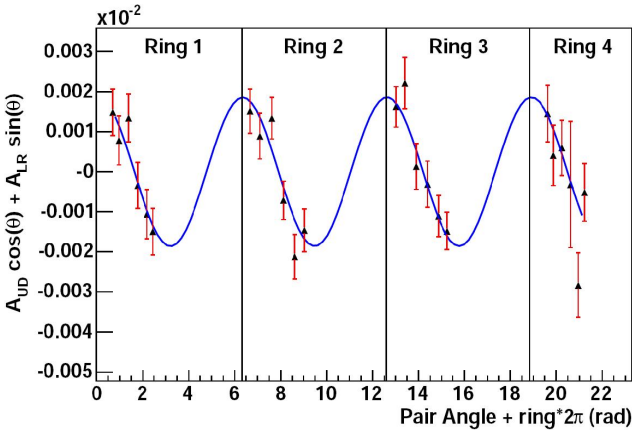

Fig. 127. Chlorine asymmetry as a function of angle for the four rings. The asymmetry for a detector pair that is not directly up-down or left-right is a linear sum of the UD and LR asymmetries. Here, the pure cosine nature of the fit shows that only the parity-violating UD asymmetry is nonzero. The large and well known A_γ from chlorine provides a test of our equipment.

False effects from rf spin flipper

Since the spin flipper contains signals synchronized with the spin flip, it is vital that none of these signals couple in any way to the detector signals, where the crosstalk could show up as a false signal of parity violation. During the 2005 run we checked for such false effects. The electronic noise is very small, so, with the neutron beam off, a very precise false asymmetry measurement can be made in a short time. One possible source of false asymmetry is a signal that leaks through and adds to the detector signal. Such an additive false signal can be detected by running with the spin flipper operating, but with no detector signal. It is also possible that some mechanism, for example magnetic field leakage from the spin flipper, could cause a helicity correlated gain change in the detector such that a false signal would only show up with a signal at the detector. Such a multiplicative effect can be detected by running the spin flipper while a low noise detector signal is generated by LEDs. Running 2 hours with both the beam and the LEDs off showed a false signal of $(-4 \pm 3) \times 10^{-9}$. Running 11 hours with beam off, LEDs on, gave $(-1 \pm 4) \times 10^{-9}$. Both are consistent with zero at the $\sim 10^{-9}$ level and will be of no consequence even for the $\pm 1 \times 10^{-8}$ measurement at the SNS.

Interference from FP-11

An unexpected problem has been interference from an 11 T superconducting magnet on the adjacent flight path, FP-11. Figure 128 shows the guide field measured in our cave in May while the FP-11 magnet was turned off for a nitrogen and helium fill and then turned back on again. In this particular case the magnet was only running at 5.5 T yet the disturbance to our FP-12 guide field was roughly ten times what we can tolerate. The solution has been an administrative one in which NPDγ (FP-12) and FP-11 will not be scheduled for beam at the same time. Unfortunately, this cuts our running time per calendar year in half.

Spin filter efficiency

To check the efficiency of the rf spin flipper (RFSF), a ^{3}He analyzing cell was placed just upstream of the final beam monitor (M3) as shown in Fig. 129. Collimation was also installed to allow us to check how the efficiency varied across the neutron beam. Ideally, the analyzer passes one spin state and blocks the other.

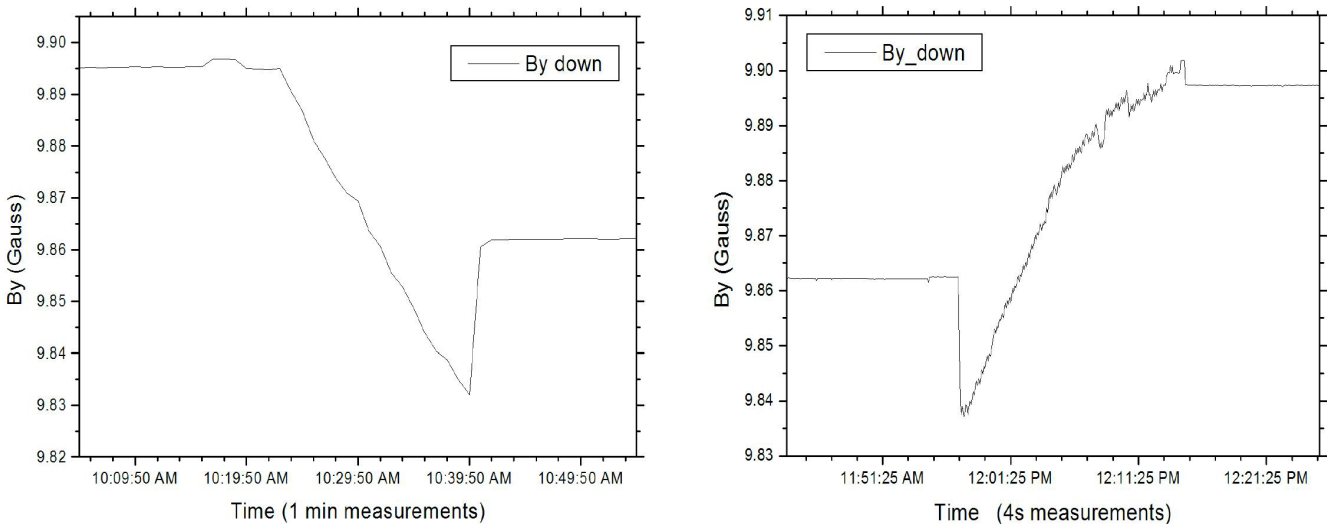

Fig. 128. Vertical holding field measured in the NPDγ FP-12 cave during May while the superconducting coil in the neighbouring FP-11 flight path was turned off for cryogen re-filling. The left panel is during ramp down and the right panel is during ramp up. Even though the coil was only running at one-half of its nominal 11 T field, the disturbance to the field in the FP-12 cave is roughly ten times what can be tolerated by NPDγ.

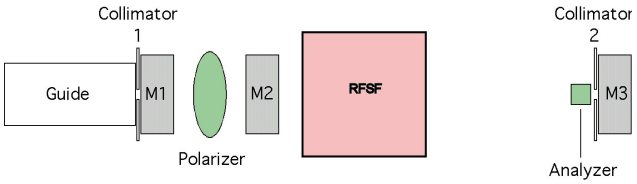

Fig. 129. Measuring the rf spin flipper efficiency. The analyzer passes one spin state and blocks the other. The polarizer and analyzer were calibrated using the Manitoba neutron monitors, M1, M2, and M3.

The combined polarizer-analyzer efficiency was calibrated by measuring the change in M3 signal when the spin direction was reversed with 100% efficiency at the ^{3}He polarizer using adiabatic fast passage (AFP). The rf spin flip efficiency is $\Delta M3_{\rm RFSF}/\Delta M3_{\rm AFP}$. During the spring run, the spin flip efficiency averaged over the beam cross section was 98%. Figure 130 shows the signal from M3 during one eight-state ($+--+-++-$) RFSF spin sequence.

Collaborators: J.D. Bowman (spokesman), T. Ito, A. Klein, S.I. Penttila, W.S. Wilburn, V.W. Yuan, Los Alamos National Lab; R.D. Carlini, Thomas Jefferson National Accelerator Facility; T.E. Chupp, University of Michigan; S. Covrig, M. Dabaghyan, F.W. Hersman, University of New Hampshire; S.J. Freedman, B. Lauss, University of California, Berkeley; T.R. Gentile, National Institute of Standards and Technology; M. Gericke, R.C. Gillis, S.A. Page, University of Manitoba; G.L. Greene, R. Mahurin, University of Tennessee; T. Ino, Y. Masuda, S. Muto,

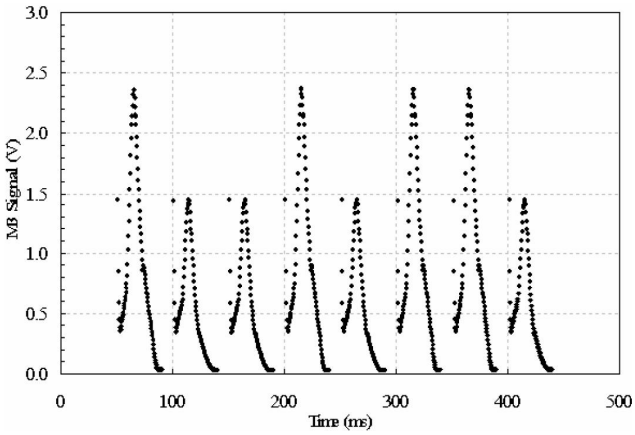

Fig. 130. Signal at M3 for eight neutron pulses corresponding to the spin sequence ($\uparrow\downarrow\downarrow\uparrow\downarrow\uparrow\uparrow\downarrow$) at the rf spin flipper. The rf spin flip efficiency is $\Delta M3_{\rm RFSF}/\Delta M3_{\rm AFP}$, where $\Delta M3_{\rm AFP}$ is the M3 change for 100% spin flip efficiency as determined by reversing the spin at the ^{3}He cell using adiabatic fast passage.

KEK National Laboratory; G.L. Jones, Hamilton College; M.B. Leuschner, B. Losowski, J. Mei, H. Nann, W.M. Snow, Indiana University; G.S. Mitchell, University of California, Davis; W.D. Ramsay, University of Manitoba/TRIUMF; S. Santra, Bhabha Atomic Research Center; P.-N. Seo, North Carolina State University; E.I. Sharapov, Joint Institute for Nuclear Research, Dubna; M. Sharma, University of Michigan; T.B. Smith, University of Dayton.